Exclusive Higgs Production and Decay to $WW^{(*)}$ at the LHC and Semiconductor Tracker Studies for the ATLAS Detector

Irina Nasteva

2006

Particle Physics Group

School of Physics and Astronomy

A thesis submitted to the University of Manchester for the degree of Doctor of Philosophy in the Faculty of Engineering and Physical Sciences

Contents

Total word count: 24285

List of Tables

List of Figures

Abstract

ATLAS is a general purpose experiment which will start operation at the LHC proton-proton collider in 2007. This thesis presents work carried out towards the preparation of the experiment in two aspects: detector development for the semiconductor tracker (SCT), and a Monte Carlo simulation of a Higgs search.

Finite element analysis was carried out to investigate the thermal properties of the SCT cooling blocks. Several possible designs were studied, and the results agreed with previous measurements of prototype blocks. The analysis confirmed that the SCT modules can be safely operated with a cooling block which is thermally split with a 1-mm layer of polyether ether ketone plastic.

The common mode noise performance of SCT modules with binary readout was tested by analysing coherent fluctuations in the occupancies of groups of channels. The measured levels of common mode noise at the system test were less than 200 electrons equivalent noise charge, which is within the limits imposed by ATLAS.

A simulation analysis was performed of exclusive Higgs production and decay to $WW^{(*)}$. The signal was generated using the ExHuME Monte Carlo, which implements the Durham model of exclusive diffraction. Events were selected by applying the ATLAS leptonic trigger criteria and requiring both protons to be tagged by the forward proton detectors at 215 m or 420 m downstream from the interaction point. It was found that the Higgs signal can be detected for masses in the range $140 < M_H < 200$ GeV. Between 3 and 6 events are expected in 30 fb^{-1} of data, the equivalent of three years of LHC running at initial luminosity.

Declaration

No portion of the work referred to in this thesis has been submitted in support of an application for another degree or qualification of this or any other university or other institution of learning.

Irina Nasteva
School of Physics and Astronomy
University of Manchester
Oxford Road
Manchester
M13 9PL
June 2006

Copyright

The Author

The author was educated at the American College of Sofia, Bulgaria, between 1992 and 1997, before obtaining a first class MSc (Hons) degree in Physics at the University of Sofia in 2002. The work presented here was undertaken at the University of Manchester.

Acknowledgements

I owe thanks to many people involved in this thesis, and in my life during the past four years. I am most grateful to my supervisor Brian Cox for choosing such an interesting project, and for the useful discussions. Thanks are due to Andy Pilkington and Andrés Osorio who helped me many times, not only with the code but also with any physics-related (or football-related) issues. Thanks also to Jeff Forshaw and Valery Khoze for explaining the theory.

On the hardware side of the thesis, thanks to Ian Duerdoth for supervising me in my first year. Many thanks to Steve Snow, Jo Pater, Paul Bell, Joe Foster and Ray Thompson for their useful advice. Their help with the experimental setup, programming, and running tests was much appreciated.

I would like to thank Fred Loebinger, Stefan Söldner-Rembold and Paul Miyagawa for proof-reading my thesis. Special thanks to Fred who made it possible for me to be here, and who was always helpful when I needed guidance. Thanks to Sabah for all his support. Many thanks to the HEP group for creating an extraordinarily friendly environment and for the entertaining coffee breaks.

Thanks to all the nice people I met in Manchester (in no particular order!): Sarah, Mitch, Marta, Alessandra, Shiv, Paul, Pete, James, Carl, Sarah, Simon, Will, Chris and everyone else. Also thanks to those who put up with living with me: John, Mark, Andy, Luis, Steve and Ian. Thanks to Nick for being patient and supportive. Finally, thanks to my parents, мама и тати, for everything.

Chapter 1

Introduction

One of the biggest questions facing particle physics today is that of the origin of mass. The Standard Model of particle physics, which unifies the theories of the electromagnetic, weak and strong interactions, is based on symmetries describing massless particles. In the model, the electroweak symmetry is broken via the Higgs mechanism in order for particles to acquire mass. As a consequence, the Higgs mechanism predicts a new doublet of complex scalar fields which leads to the existence of a new massive scalar particle, the Higgs boson. However, the Standard Model does not give a value for the Higgs mass, which is a free parameter. Detecting the Higgs boson and measuring its properties will be fundamental to our understanding of particle physics.

There have been extensive searches for the Higgs boson in particle experiments, yet it remains undiscovered to this day, and only constraints on its mass have been set. Detecting the Higgs is one of the main aims of the ATLAS experiment under construction at CERN. ATLAS is a general purpose particle detector optimised for new physics searches and precision measurements. It will start operation in 2007 at the Large Hadron Collider (LHC), which will collide protons

on protons with a centre-of-mass energy of 14 TeV. With such high energies, it will be able to scan a wide range of particle masses, to obtain accurate measurements of particle properties and to search for various new physics scenarios. If the Standard Model Higgs boson exists, it will definitely be detected at ATLAS, and its properties will be studied.

The work described in this thesis investigates two topics: detector development for the ATLAS semiconductor tracker, and a Higgs search simulation study at ATLAS. The thesis is organised as follows. Chapter 2 introduces the experimental apparatus: the LHC accelerator and the ATLAS detector. Then the properties of silicon detectors and the characteristics of the ATLAS semiconductor tracker (SCT) are described in Chapter 3. The next two chapters present the work done in two studies for the ATLAS SCT subdetector. Chapter 4 details an investigation into the thermal design of the SCT cooling block, and Chapter 5 describes a study of common mode noise for the SCT.

A brief overview of the Standard Model of particle physics is given in Chapter 6. This is followed by the theory of exclusive Higgs production, which is specific to the current study, in Chapter 7. Chapter 8 presents the simulation analysis of exclusive diffractive Higgs production and decay to $WW^{(*)}$ at the ATLAS experiment. It details the signal and background characteristics and the event selection approach, and discusses the results of this analysis. Chapter 9 then summarises and gives a conclusion.

Chapter 2

The ATLAS Experiment at the LHC

2.1 The Large Hadron Collider

The Large Hadron Collider (LHC) is the next proton-proton collider being built at the European Organisation for Nuclear Research (CERN) near Geneva, Switzerland. The accelerator will bring protons or heavy ions into head-on collisions at higher energies than all currently existing colliders, allowing physicists to study further the structure of matter and the laws of its interactions.

The LHC [1] is designed to collide protons on protons with a centre-of-mass energy $\sqrt{s}$ of 14 TeV, and lead ions on lead ions with $\sqrt{s}$ of up to 1150 TeV. It consists of two synchrotron rings installed in the 27 km tunnel used previously by the LEP accelerator. Because both beams consist of equally charged particles, they circulate in separate rings immersed in opposite magnetic dipole fields. The beams share a common ring of magnets, in which each magnet has two sets of coils to create the opposing fields. Superconducting magnet technology is used

to create a high dipole field of up to 8.33 T.

The number of events per second created in LHC collisions can be calculated from

$$N_{\text{event}} = \mathcal{L} \times \sigma_{\text{event}} \, , \tag{2.1}$$

where σ_{event} is the event cross-section and $\mathcal{L}$ is the instantaneous luminosity. The design luminosity of the collider will reach $\mathcal{L} = 10^{34}$ cm^{-2}s^{-1} to provide the experiments with high interaction rates. In the first three years of operation the LHC will run at a lower initial luminosity of $\mathcal{L} = 3 \times 10^{33}$ cm^{-2}s^{-1}. The two colliding beams are organised into 2808 bunches of 1.15×10^{11} protons, which will cross every 25 ns. The total cross-section for proton-proton interactions will then be around 100 mb, producing 10^9 interactions per second at the maximum luminosity. The high event rates allow the study of very rare processes, but at the same time the resulting radiation environment poses severe constraints on detector designs.

The effective centre-of-mass energy available in the collisions of proton constituents will reach the TeV range, potentially creating new massive particles. One of the main purposes of the LHC is to search for the Higgs boson, predicted by the Standard Model, or for an alternative mechanism for electroweak symmetry breaking. The accelerator will also look for signatures of new physics beyond the Standard Model, such as supersymmetric particles or leptoquarks. Its high luminosity will enable experiments to make precision measurements of particle properties, cross-sections and decay rates, as well as to examine rare processes so far unobserved. The LHC will provide a crucial test of our current physical theories, thus enhancing our understanding of the fundamental laws of nature.

The layout of the LHC ring, showing the positions of the four experiments which will operate on the collider, is given in Fig. 2.1. Two of the experiments,

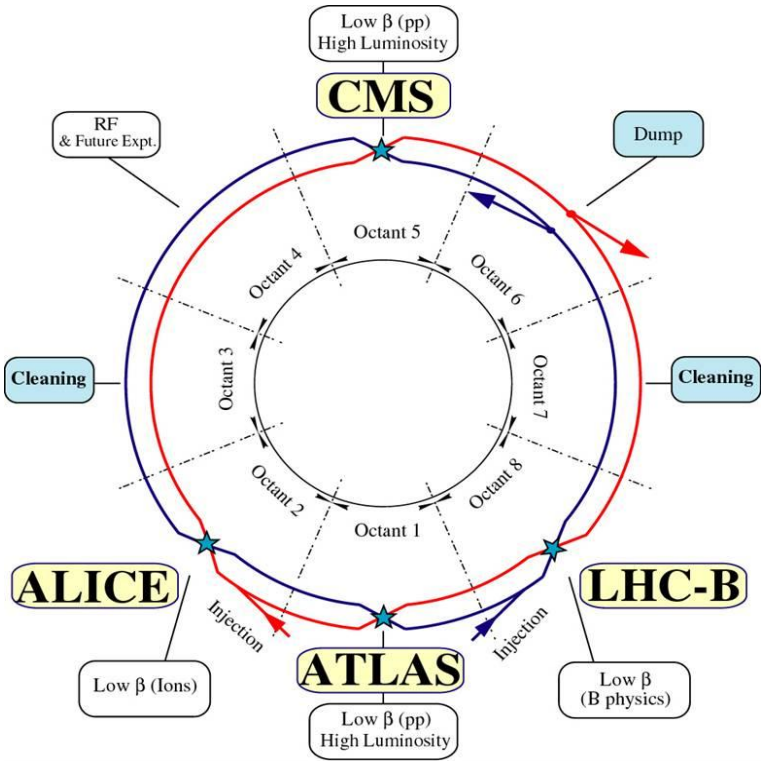

Figure 2.1: Schematic layout of the LHC beams and the four experiments [1].

ATLAS and CMS, are general purpose experiments. The other two experiments are specialised: ALICE will study quark-gluon plasma produced in heavy ion collisions, and LHCb will focus on CP violation in B meson decays.

2.2 The ATLAS Detector

ATLAS (A Toroidal LHC ApparatuS) is a general purpose experiment designed to exploit the full discovery potential of the LHC [2]. The origin of mass at the electroweak scale is a major focus of interest for ATLAS, which is therefore sensitive to the largest possible Higgs mass range. The experiment will also look for supersymmetric particles and for compositeness of the fundamental fermions, and will study CP violation in B-decays as well as top quark properties. In addition

to the proton-proton programme, ATLAS will also study heavy-ion collisions at the LHC.

The ATLAS detector is designed to carry out these physics studies at the high LHC luminosities. The general physics programme of the experiment requires detector sensitivity to a variety of final-state signatures. Therefore the main detector performance goals can be summarised as [2]:

- very good electromagnetic calorimetry for electron and photon identification and energy measurements, complemented by high resolution hermetic calorimetry for jets and missing transverse energy $\not{E}_T$;
- efficient tracking for lepton momentum measurements, for b-tagging, and for enhanced electron and photon identification, as well as τ and heavy-flavour vertexing;
- stand-alone, high precision muon momentum measurements.

ATLAS uses a coordinate system with origin at the interaction point, z coordinate along the beam direction and xy plane perpendicular to the beam axis. Polar coordinates are defined as the distance from the origin R, the polar angle θ from the beam axis and the azimuthal angle ϕ around the beam axis. The transverse momentum p_T and transverse energy E_T of particles are given in the xy plane in terms of their momentum p and energy E as

$$p_T = p \sin\theta \,, \qquad E_T = E \sin\theta \,. \tag{2.2}$$

Pseudorapidity, η, is also formulated using the polar angle θ,

$$\eta = -\ln \tan \frac{\theta}{2} \,. \tag{2.3}$$

In the central detector region $|\eta|$ is close to zero, while it grows to infinity in the beam directions.

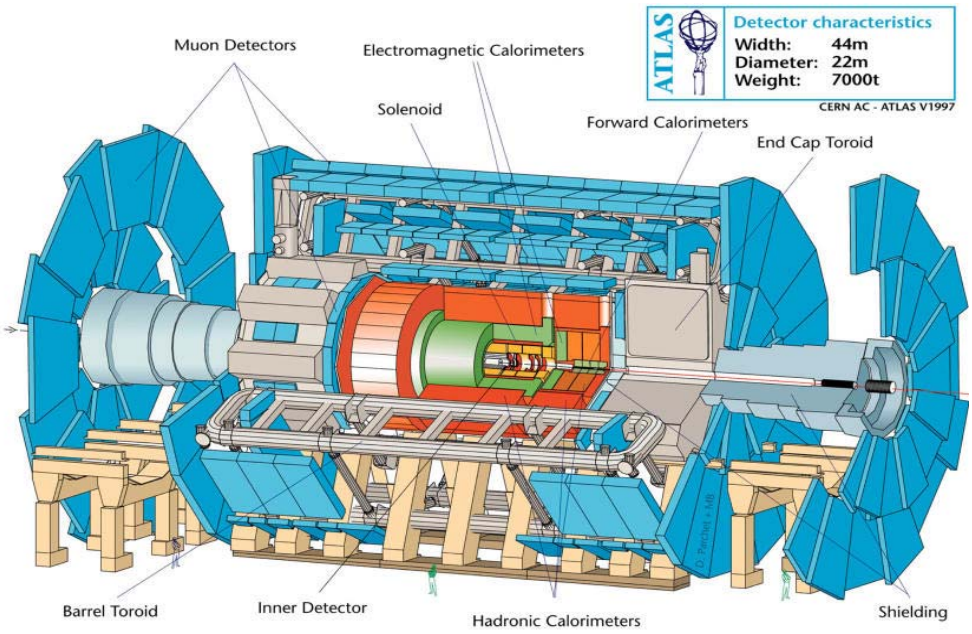

Figure 2.2: Three-dimensional view of the ATLAS detector and its subdetector systems [3].

The detector design considerations include coverage over a large pseudo-rapidity range. In addition, efficient triggering and measurements of particles are required at low transverse momentum thresholds. To achieve these goals, ATLAS is designed as a 4π coverage multi-purpose detector, consisting of three basic subdetector systems: muon spectrometer, calorimeters, and inner detector.

The global detector layout (Fig. 2.2) is largely determined by the configurations of the magnetic fields. A superconducting solenoid magnet surrounds the inner tracking detectors, outside of which are the highly granular electromagnetic and hadronic calorimeters. The outermost part of the detector is formed by large superconducting air-core toroid magnets, consisting of independent coils arranged with an eight-fold symmetry. They contain the muon spectrometer, which comprises three stations of high-precision tracking chambers complemented with fast trigger chambers.

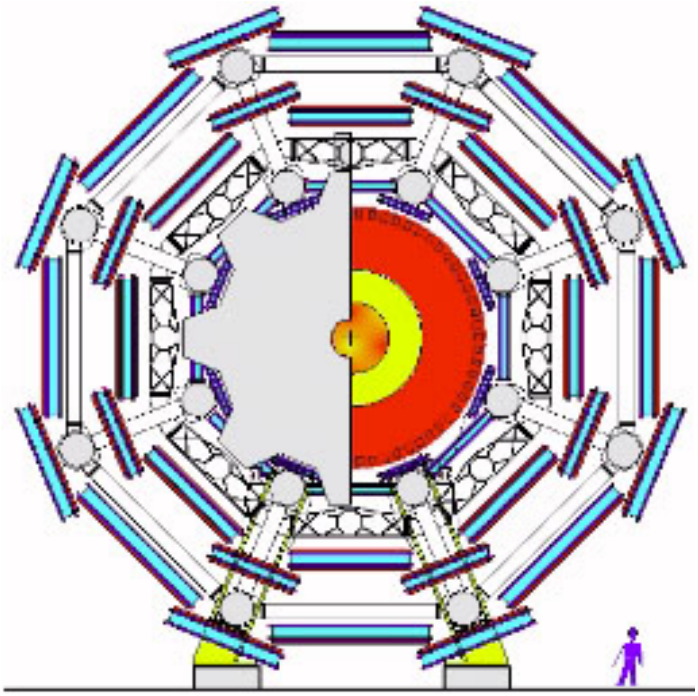

Figure 2.3: Transverse view of the ATLAS muon spectrometer. The muon chambers (shown in blue) form layers surrounding the tracking detectors (in yellow) and the calorimeter (in red).

With approximate dimensions of 44 m length and 22 m height, and a weight of 7000 tons [2], ATLAS will be the biggest particle physics detector ever constructed.

2.2.1 Muon System

The muon spectrometer is situated outside all other subdetector systems (Fig. 2.3). Its functions include muon identification and sign and momentum measurements of muons using the curvature of their trajectories bent by the magnetic field, as well as triggering [2]. The air-core toroid magnet system, with a long barrel and two end-cap magnets, generates a large magnetic field with strong bending power. The non-uniform field is in most cases perpendicular to the muon trajectories,

allowing excellent muon momentum resolution.

Three layers (stations) of high-precision tracking chambers form the muon system in the barrel region: at the inner and outer ends of the magnetic volume, and in the mid-plane to measure the sagitta. In the forward region the chambers are placed vertically. In addition to the high-precision chambers, there are independent fast trigger detectors.

A muon station chamber consists of two detector multilayers, each of which contains three or four individual planes of closely packed detectors. These are Monitored Drift Tubes (MDT), used over a large part of the η acceptance, and Cathode Strip Chambers (CSC), positioned in the high η forward region. MDT chambers consist of multilayers of drift tubes with a diameter of 30 mm, and they achieve a spatial resolution of ~ 60 μm. The CSCs are fast multiwire proportional chambers, whose cathode strips are finely segmented to perform precise position measurements of typical resolution 50 μm.

The choice of dedicated trigger detectors is based on the requirement for excellent time resolution. Two trigger chamber technologies are used: Resistive Plate Chambers (RPC) in the barrel and Thin Gap Chambers (TGC) in the forward regions. RPCs are gaseous parallel plate detectors, whose external pick-up electrodes are segmented into strips to give position information. TGCs are wire chambers with capacitive readout on pads or strips. Both detectors achieve a reasonable position precision with a time resolution of a few nanoseconds. In addition to triggering, they complement MDT chambers with bunch crossing assignment as well as position information. The combination of different detector technologies contributes to high muon momentum resolution and efficient triggering.

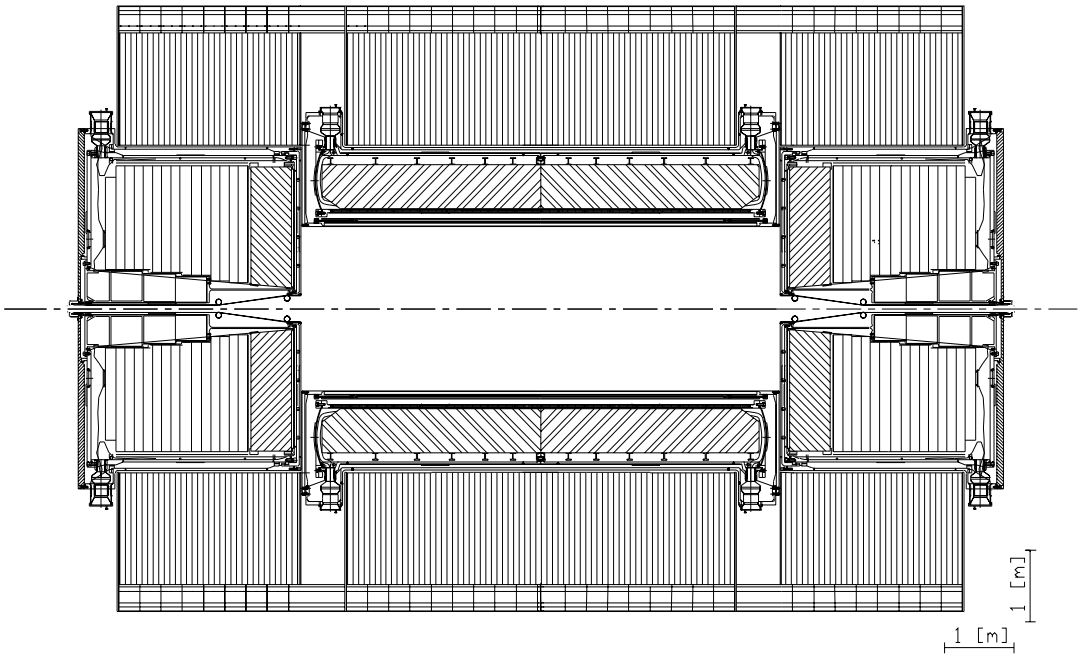

Figure 2.4: A cross-sectional view of the ATLAS calorimeter system, showing the electromagnetic calorimeters in the inner region and the hadronic calorimeters in the outer regions.

2.2.2 Calorimetry

The calorimeter system is contained in a cylindrical region around the beam pipe, between an inner radius of 1.15 m and an outer radius of 4.25 m. Its position is in the middle detector layer between the inner tracking cavity and the muon system. A two-dimensional view of the calorimeter system is shown in Fig. 2.4. It consists of a liquid argon (LAr) electromagnetic calorimeter and a hadronic tile calorimeter [2]. Calorimetry is needed to measure the energy and direction of photons, electrons, isolated hadrons and jets, as well as missing transverse energy.

The barrel electromagnetic calorimeter includes a LAr calorimeter and a presampler detector. The highly granular LAr electromagnetic sampling calorimetry

covers the pseudorapidity range of $|\eta| < 3.2$ and has excellent energy and position resolutions. The LAr endcaps consist of an electromagnetic calorimeter, a hadronic calorimeter with flat absorber plates, and a forward calorimeter with a tube electrode structure. The liquid argon sampling calorimetry uses lead absorber for the barrel part, and copper and tungsten alloy absorbers for the forward electromagnetic and hadronic modules.

The hadronic scintillator tile calorimeter is divided into a barrel and two extended barrel parts and surrounds the LAr calorimeter over its full length. Its technology is based on sampling with plastic scintillator tiles embedded in iron absorber.

The whole calorimeter system ensures precise energy measurements, as well as a very good jet and missing energy performance of the ATLAS detector.

2.2.3 Inner Detector

The ATLAS inner detector (ID) is the innermost detector system, which tracks charged particles from the LHC beam pipe to the electromagnetic calorimeter system. The layout of the detector and its subsystems is shown in Fig. 2.5. The ID consists of silicon pixel detectors closest to the interaction point, followed by silicon strip detectors and a straw tube transition radiation tracker (TRT). It combines high-resolution detectors close to the beam line with continuous tracking elements at outer radii [2, 4]. It is contained within a cylinder of length 6.80 m and radius 1.15 m, with a solenoidal magnetic field of 2 T.

The task of the inner detector is to reconstruct tracks and vertices (primary as well as secondary from the decays of short-lived particles) with high efficiency and precision, contributing to particle recognition, momentum measurements and

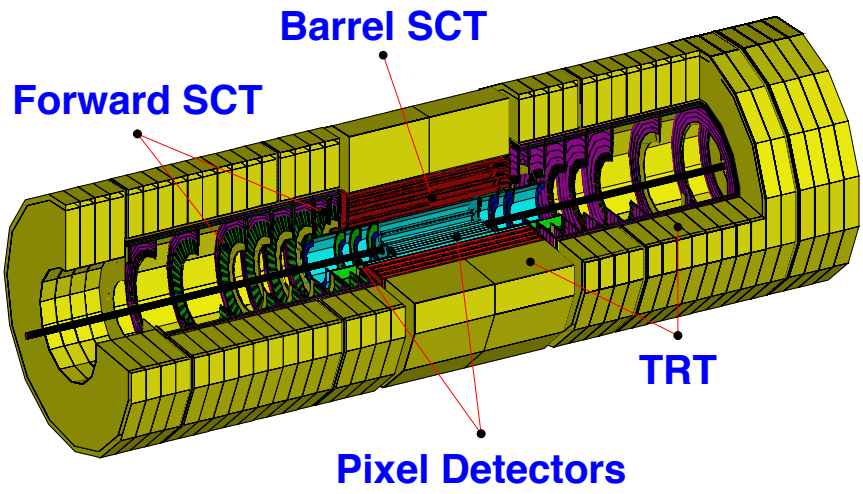

Figure 2.5: Three-dimensional view of the ATLAS inner detector [4].

triggering [4]. These requirements must be met in conditions of high track density and at a high beam crossing rate, imposing the use of fine-granularity and radiation-hard detectors. The tracker performance is assured even at the highest LHC luminosities, covering the pseudorapidity range of $|\eta| < 2.5$.

A cross-sectional view of the inner detector is shown in Fig. 2.6, and the basic design parameters and resolutions for space-point measurements are given in Table 2.1. The multilayer detector design maximises tracking precision by making a large number of measurements along the length of a track.

Highest granularity around the interaction point is achieved using semiconductor pixel detectors. Three layers of silicon pixel detectors in the barrel region, and four disks in each of the end-caps guarantee high-precision track measurements. The system contains about 2500 modules, each of which consists of detector substrates and readout integrated circuits mounted onto them. The pixel sensors are segmented in $R\phi$ and z coordinates. The innermost pixel layer, used for vertexing at a radius of 4 cm from the beam line, will have a limited lifetime due to radiation damage, and will have to be replaced after a few years of LHC

System	Position	Area (m^2)	Resolution σ (μm)	Coverage in $\lvert\eta\rvert$
Pixels	1 removable barrel layer	0.2	$R\phi = 12, z = 66$	$0 - 2.5$
	2 barrel layers	1.4	$R\phi = 12, z = 66$	$0 - 1.7$
	4 end-cap disks on each side	0.7	$R\phi = 12, R = 77$	$1.7 - 2.5$
SCT	4 barrel layers	34.4	$R\phi = 16, z = 580$	$0 - 1.4$
	9 end-cap wheels on each side	26.7	$R\phi = 16, R = 580$	$1.4 - 2.5$
TRT	Axial barrel straws		170 (per straw)	$0 - 0.7$
	Radial end-cap straws 36 straws per track		170 (per straw)	$0.7 - 2.5$

Table 2.1: Parameters of the inner detector [4].

operation. The pixel detector provides three of the high-precision track measurements, and determines the impact parameter resolution and the ID ability to reconstruct short-lived particles.

The semiconductor tracker (SCT) has silicon strip detectors which will be used at radii between 30 cm and 60 cm from the beam axis. The silicon strips in a module are aligned at a small stereo angle (40 mrad) to measure both $R\phi$ and z coordinates. The SCT modules are arranged in four barrel layers and nine forward disks to cover the whole pseudorapidity range. SCT is designed to provide at least four precision measurements per track, giving information on momentum, impact parameter and vertices.

The transition radiation tracker (TRT) is the outermost tracking subdetector, providing continuous tracking at outer radii. It consists of small diameter straw tubes parallel to the beam direction in the barrel part and arranged radially into wheels in the forward region. Charged particles ionise the gas in a straw and the produced electrons are detected by the sense wire in the centre. Each straw provides a drift-time measurement and discriminates between tracking hits and

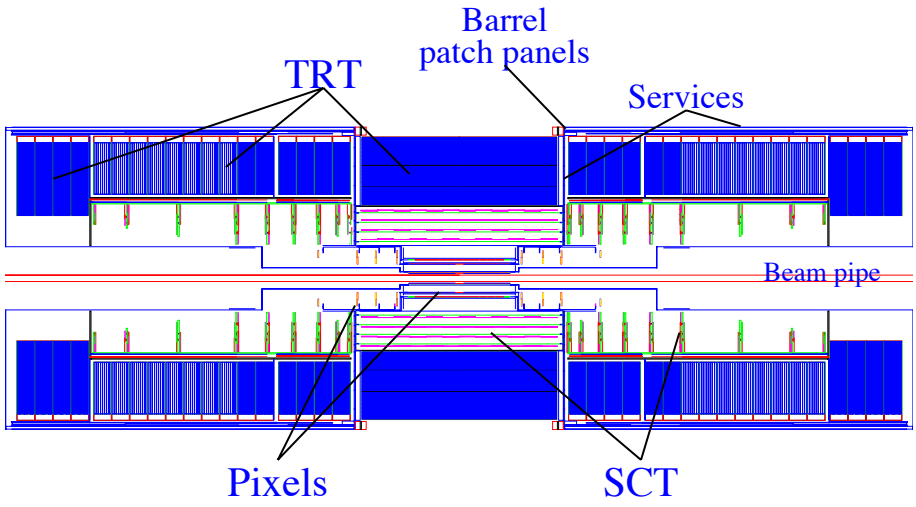

Figure 2.6: Cross-sectional view of the inner detector [3].

transition-radiation hits. The lower precision of the TRT compared to that of the silicon detectors is compensated by the large number of measurements—36 per track. The TRT also enhances the ATLAS electron identification capabilities by detecting transition-radiation photons in the straw tubes filled with xenon, and is used in the level-2 track trigger.

2.2.4 Trigger, Data Acquisition and Computing

The ATLAS trigger system serves the purpose of selecting information about interesting events out of all interactions. It will reduce the event rate from the LHC bunch crossing rate of 40 MHz to about 100 Hz for recording onto permanent storage. The trigger is organised in three levels, called level 1 (L1), level 2 (L2) and Event Filter [3].

The L1 trigger [5] is a synchronous system of dedicated processors, acting on reduced-granularity data from a subset of the detectors. It accepts data at the full bunch crossing rate of 40 MHz (every 25 ns) and takes about 2.5 μs to

reach a decision. During the level 1 processing, all subdetector data are held in pipeline memories. L1 uses information from the calorimeter and muon trigger chambers, and its decision is based on the presence of high transverse momentum muons, electrons, photons and jets.

After the level 1 trigger has reduced the rate to 100 kHz, the data are further processed by the level 2 trigger system, which uses full-precision information from all subdetectors. The L2 trigger examines only the regions of interest identified by L1. It performs more complicated algorithms to find tracks and measure their transverse momentum, with varying decision times of up to 10 ms.

In the high level trigger system, the full data of each event accepted by L2 are transferred via the event builder to a farm of processors for complete analysis. The Event Filter performs event reconstruction and makes the final selection of events to be recorded for offline analysis. The size of a single event is about 1 MB, and the maximum event rate for permanent recording is about 100 Hz.

Data acquisition (DAQ) and computing are major aspects of the whole ATLAS experiment. The fields of online and offline computing are interconnected and so require a global software design approach. Elaborate simulation and reconstruction software tools are being developed by implementing traditional as well as innovative software engineering techniques.

2.3 Forward Proton Taggers for ATLAS

For the purpose of studying exclusive processes, in which a central system is produced without the collision protons disintegrating, forward proton detectors need to be installed far from the central ATLAS detector. This is because in exclusive production the protons remain intact and lose a small fraction of their

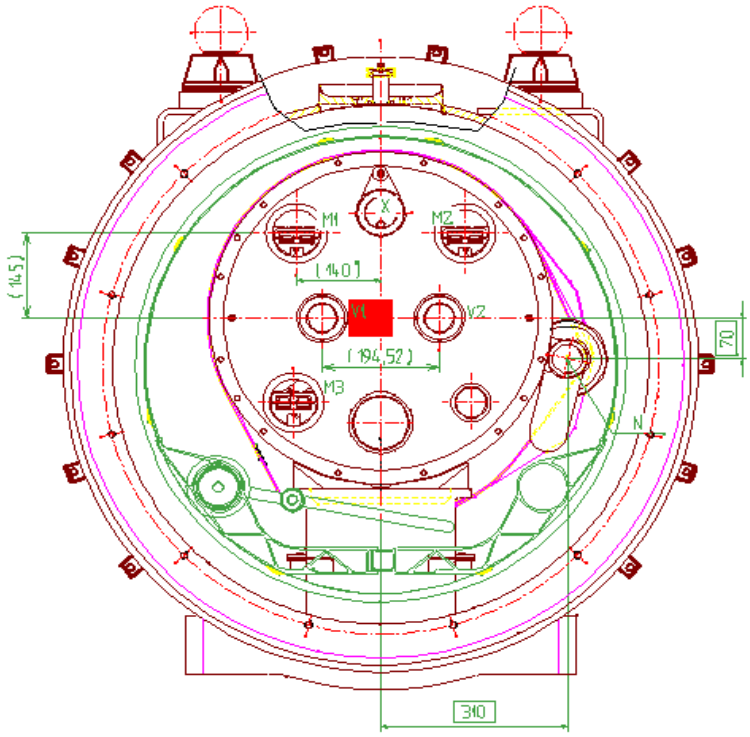

Figure 2.7: A cross-section of the LHC ring at a distance 420 m away from the ATLAS interaction point [6]. The red rectangle shows the position of the forward proton taggers between the two beam pipes.

momentum. As they continue moving down the beam pipe, dipole magnets bend their trajectories more than those of nominal beam protons, due to their loss of momentum. Suitably placed tracking detectors very near the beam pipe and away from the interaction point can then act as a spectrometer to measure the leading protons.

The feasibility of installing forward proton taggers at positions 420 m away from the interaction point is investigated by the FP420 project [6, 7]. The choice of position at 420 m is dictated by optimising the taggers' acceptance within the limited available space for detector installation around the densely packed accelerator components. At 420 m leading protons emerge a few millimetres to a

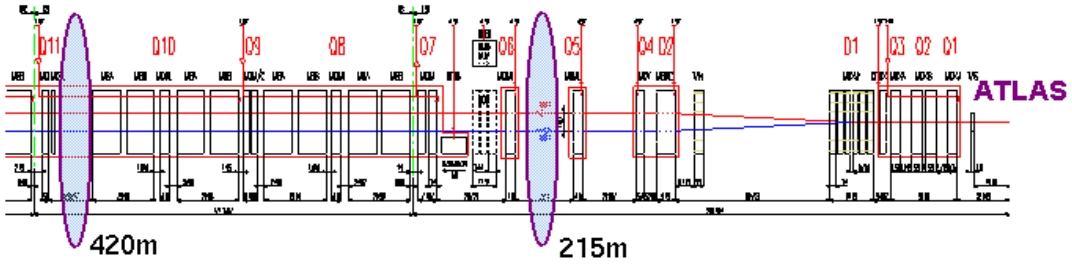

Figure 2.8: Schematic layout of the LHC lattice on the left side of ATLAS [1]. The positions of forward proton detectors at 215 m and 420 m are highlighted.

few centimetres away from the beam after passing through the field of a bending magnet, and can be detected by taggers placed between the two beam pipes. The position of proton taggers between the beam pipes is shown in Fig. 2.7.

Measuring several points along the proton track would give both the proton position and its angle with respect to the beam. This information allows the direct determination of the proton longitudinal momentum loss x and its transverse momentum p_T.

Several stations of tracking detectors will be installed in the 420-m region of the ATLAS experiment, with each station containing several planes. The detectors will have a resolution of 10 μm or better in order to achieve high precision in the momentum measurements. The detector stations will be movable with respect to the beam so they can adjust to the different LHC optics modes: during injection they have to be kept up to 30 mm away from the beams, while in collision mode the detectors have to get as close as 3 mm to the beam.

Although the detector design has not been finalised yet, the most probable technology choice seems to be 3D edgeless silicon [6]. These are radiation-hard semiconductor pixel devices with active edges, which are sensitive over the whole detector volume starting from a few microns from the physical edge. The edgeless

silicon detectors can be moved very near the beams in order to detect leading protons with small momentum losses. Silicon detectors will be complemented by quartz fast timing detectors with a resolution of 10 ps, making it possible to match leading protons with vertices in the central ATLAS detector to within 3 mm.

The information from the 420-m stations cannot be used for level 1 triggering at ATLAS, because the signals cannot propagate in time for the L1 trigger decision (the L1 latency is about 2.5 μs). This means that at L1, exclusive processes have to be selected based only on their signatures in the central detector. The FP420 tracking and timing information can then be included in high level triggers for further selection.

In addition to the detectors at 420 m, another set of taggers will be placed at a distance of 215 m away from the interaction point. Their primary purpose is to measure the total cross-section [8], but in addition they will be able to detect leading protons from exclusive processes. The positions of the proton taggers at 215 m and 420 m along the LHC beam line are shown in Fig. 2.8. Since at 215 m leading protons are deflected less by bending magnets, the detectors in this region have acceptance for higher momentum losses compared to the taggers at 420 m.

Combining the two sets of detector stations gives the possibility of measuring protons that have lost between 0.2% and 2% of their momentum. This will enable FP420 to complement the central ATLAS detector measurements in searches for new physics [9].

Chapter 3

The ATLAS Semiconductor Tracker (SCT)

The semiconductor tracker (SCT) provides tracking functions for the ATLAS experiment as a part of the inner detector. The SCT is based on silicon microstrip technology. Its modules consist of around 20000 individual microstrip sensors equivalent to an active silicon area of around 60 m^2, much larger than that of any existing detector [10].

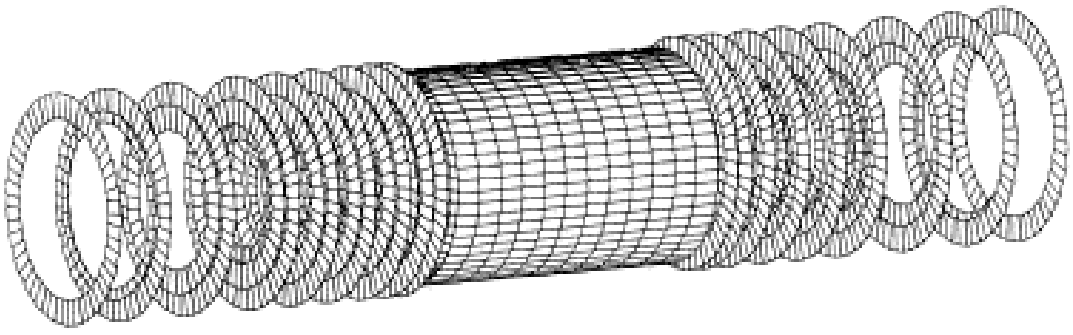

Figure 3.1: A view of the SCT modules, arranged in layers in the barrel and in disks in the forward parts of the detector.

The SCT geometrical configuration is organised into four barrel layers and nine endcap disks on both sides, as shown in Fig. 3.1. The barrel layers are situated within radii of 30 to 52 cm and contain 2112 detector modules. Each barrel module consists of two pairs of identical single-sided silicon detectors: the front pair is aligned along the beam direction, and the back-side pair is rotated by 40 mrad to provide a z-measurement capability. Each of the two sides has 768 strips of 80 μm pitch and active length 123.2 mm, which are read out by binary front-end electronics. Modules are mounted at an angle of 10° to the tangent in order to minimise the signal spread during operation in the solenoidal magnetic field, and are overlapped in a tile arrangement to avoid dead areas [10].

The endcap layout consists of nine disks in each of the forward and backward directions in the radial range $26 < R < 56$ cm, with a total of 1976 modules. The module construction is similar to the barrel part, but the endcap detector modules are wedge-shaped and arranged back-to-back (still with a 40 mrad stereo orientation). The properties of the endcap SCT system will be described in more detail in Section 3.2. Studies of the common mode noise in the readout electronics of the endcap SCT modules are discussed in Chapter 5.

To minimise the radiation damage to silicon detectors, both the barrel and endcap SCT systems will be operated at temperatures lower than -7°C in a dry, nitrogen environment. That is why the detector thermal properties and the cooling system are of special importance for the SCT. Simulations of the thermal performance of the cooling block for endcap modules are described in Chapter 4.

3.1 Silicon Strip Detectors

The choice of silicon detectors for the tracking layers of ATLAS is dictated by their high signal speed, excellent resolution and granularity.

Semiconductor detectors have been used in high energy physics experiments for vertexing and tracking. Silicon has a high intrinsic energy resolution and a small ionisation energy, which lead to suitable and fast signals. The high spatial resolution is a result of integrated circuits which allow the use of large numbers of ultra-thin electrodes on silicon wafers. To achieve good precision in operation, semiconductor detectors rely on low-noise electronics [11].

Silicon detectors can be described as *pn* junction diodes. Reverse bias is applied to the junction, forming a sensitive region depleted of mobile charge carriers, and any charge created in this volume moves across the junction to the electrodes. In silicon microstrip detectors, one side of the junction is segmented into narrow strips, which collect the released charge and pass it to the readout electronics to form a signal.

3.1.1 Principles of Operation

In semiconductors there is an energy gap E_g between the valence band, where the outer shell electrons are, and the conduction band, which is empty. If energy is supplied to the valence electrons, they can be raised to the conduction band, where they are free to move throughout the entire crystal. Releasing an electron from the valence band creates a vacancy in it, called a hole. For silicon, the energy necessary to create an electron-hole pair is 3.6 eV. At temperatures above absolute zero, there is enough thermal energy to liberate some electrons and thus create holes in their position. In an intrinsic material, electron-hole pairs are

constantly being created, while at the same time other pairs recombine, so the densities of electrons and holes are constant. When a charged particle passes through the material, it creates about 3.2×10^4 free charge carriers (for silicon of thickness 300 μm), which are too few to be detected, compared to the number of free carriers which exist in the volume, $\sim 4.5 \times 10^8$ [12].

The equal numbers of charge carriers can be changed by doping the material. Silicon, which is in group IV of the periodic table and has four valence electrons, can be doped by introducing impurities of elements from group III (having 3 valence electrons) or group V (5 valence electrons) to the crystal lattice. In the former case it is doped with acceptor atoms and becomes p-type material, in which the majority charge carriers are holes. If the impurity is pentavalent (donor atoms), there is an extra electron, so the majority carriers are electrons, and the material is called n-type.

By bringing into contact p-type and n-type material, a pn junction is formed between them. Because of the different concentrations of charge carriers on both sides of the junction, electrons diffuse from the n side to the p side, and holes migrate in the opposite direction. Thus the junction forms a space charge, or depletion region, containing immobile acceptor and donor ions and no free carriers. The initial carrier migration sets up a potential barrier of a few hundred millivolts to stop further migration across the junction [13]. An ionising particle passing through this depletion zone creates charge, which can be collected at the junction.

To increase the width of the space charge region, reverse bias voltage is applied, which extends the depletion zone over the full junction. The width of the depletion layer W depends on the applied voltage V_B as [13]

$$W = \sqrt{2\varepsilon\rho\mu V_B}\,, \tag{3.1}$$

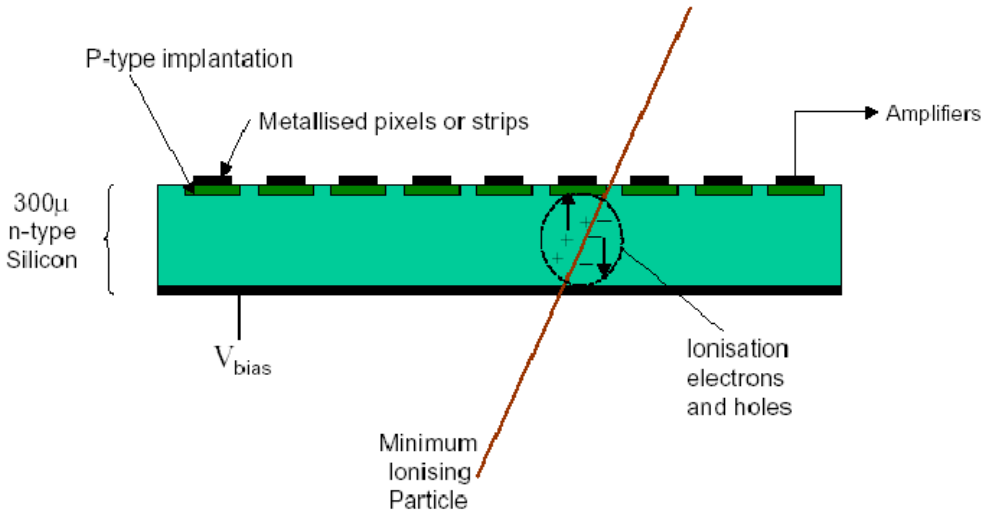

Figure 3.2: The passage of an ionising particle through a silicon detector.

where ε is the dielectric constant of silicon, ρ is its resistivity, and μ is the mobility of the majority charge carriers. Usually for silicon detectors the active volume of the detector is the n-type silicon, while the p-type silicon is shallow and serves only for depletion. Then in Eq. (3.1) the mobility is that of electrons ($\mu = \mu_n$) from the n-type silicon.

The voltage needed to completely deplete a silicon wafer of thickness d is called the depletion voltage V_d, which can be expressed as

$$V_d = \frac{d^2}{2\varepsilon\rho\mu}\,. \tag{3.2}$$

For silicon wafers of typical thickness $d \approx 300$ μm and resistivity $\rho \approx 5$ kΩ cm, the depletion voltage is about 70 V.

The externally applied electric field separates the electron-hole pairs created by the passage of a particle. Electrons drift toward the anode and holes toward the cathode, so all charge is collected at the electrodes on the two sides of the junction. The resulting current pulse has an integral equal to the total charge

produced by the incident particle, i.e. proportional to its energy. The passage of an ionising particle through a semiconductor detector is schematically shown in Fig. 3.2.

3.1.2 Leakage Current

Current is produced on the electrodes not only when a particle passes and ionises the active detector volume. Although the depletion region is free of majority charge carriers, minority charge carriers (holes for the n side and electrons for the p side) can still be thermally generated. In the absence of an electric field the created electron-hole pairs recombine, but when the detector is biased, they get separated and drift to the opposite charge electrodes, creating a leakage current.

Since there is no charge multiplication in silicon detectors, large leakage current can result in high readout noise, as well as unwanted high power consumption. It has two components depending on the region where charge was created: a generation current within the depletion zone, and a diffusion current, which originates in the neutral silicon and diffuses to the depletion zone. When the detector is fully depleted, the diffusion current vanishes, and only the generation component contributes to the leakage current. It is highly temperature dependent due to the thermal dependence of electron-hole creation by lattice defects in the bulk, which is why detector materials have to be very pure. To reduce leakage current, detectors also have to be operated at constant low temperatures; therefore, cooling is very crucial for their signal-to-noise performance.

3.1.3 Radiation Damage

The radiation environment at the LHC will be very harsh, so it will alter directly the properties of silicon detectors [4, 14]. The most serious damage occurs from lattice displacement of silicon atoms (non-ionising energy loss). This creates large numbers of new donor and acceptor defects, thus changing the charge density in the depletion zone and increasing the leakage current. According to the SCT detector specifications [10], the maximum allowed leakage current per strip is 2 nA for unirradiated detectors and 2 μA for irradiated detectors.

Under continuous high fluence irradiation, n-type silicon becomes increasingly p-type until it undergoes type inversion. This also affects the depletion voltage, which decreases and then increases again after the type inversion.

A negative consequence of the increased leakage current after irradiation is the possible thermal runaway. This happens when the power, dissipated in the silicon due to large leakage current, heats it up. If this heat is not extracted, it will further increase the leakage current due to its strong temperature dependence, which in turn will increase the heat. This process can quickly run away uncontrollably and should be avoided by efficient cooling.

Another effect of irradiation is the reverse annealing process [15], which initially repairs the lattice defects, but in the long term causes the damage to increase. In the process electrically inactive defects are created which then interact and become electrically active. Reverse annealing occurs faster at higher temperatures, so the silicon detectors must be kept at low temperatures (-5° to -10°C) to avoid it.

3.1.4 Strip Detector Fabrication

To make a position sensitive silicon detector, the p side is segmented into narrow strips which are isolated from each other. Every p strip is metallised and bonded to the electronics which process the signals from the collected charge. The bias voltage is applied at the back plane, which is made of heavily doped n^+ silicon to define the end of the depletion region and to ensure a good Ohmic contact [13].

Detectors are made from a single silicon wafer, which is processed using planar technology [16]. First, the wafer is sliced and undergoes oxide passivation, the formation of SiO_2 to protect its surface. Then the strips are carved on the surface, and the p and n regions are formed by doping via ion implantation or diffusion (using boron acceptor and arsenic donor ions). Finally, the strips and the back side are metallised to make electrical contact with readout electronics and power supplies.

Signals are read out using AC coupling to avoid noise from leakage current going to the amplifier in direct contact. The charge goes through a capacitor to the metallic strips and is then processed by the readout electronics.

3.1.5 Performance

The strip pitch is chosen to optimise spatial resolution. The charge liberated by an ionising particle spreads during the drift to the electrodes with a Gaussian distribution of full width less than 20 μm [13], so strips of 20 μm pitch are a suitable choice. However, there is a technical limit to the production precision and readout electronics pitch, so usually it is practical to make wider pitch strips. If binary readout is used (via threshold discrimination), the resolution σ depends

on the strip pitch p as

$$\sigma = \frac{p}{\sqrt{12}}\,, \tag{3.3}$$

giving $\sigma = 14.4$ μm for a typical strip pitch of 50 μm.

The intrinsic energy resolution of silicon detectors is very high. It is dictated by the low energy threshold for producing an electron-hole pair—only 3.6 eV. Because of the high density of silicon, the average energy loss of particles is large ($\sim 390\,\mathrm{eV}/\mu\mathrm{m}$). To minimise the effects of multiple Coulomb scattering, which would degrade position resolution, thin detectors are used. There has to be a compromise due to the fact that there is no charge multiplication in silicon and that the amplitude of the signal is proportional to the detector thickness. For the optimum thickness of $\sim 300\mu$m, an ionising particle produces on average 3.2×10^4 electron-hole pairs. Consequently low-noise electronics are required, and the signal-to-noise ratio is a critical issue for silicon detectors.

The charge collection time depends on the processes of drift and diffusion of electron-hole pairs in the silicon. A typical value for the detector time response is 10 ns, which is excellent compared to that of gas detectors.

3.2 The Forward SCT Modules

There are three types of forward (endcap) SCT modules, as is shown in Fig. 3.3. The differences between them are mainly geometrical, to suit the three radial positions (rings) in each endcap disk. Most disks contain 52 outer modules and 40 middle and inner modules.

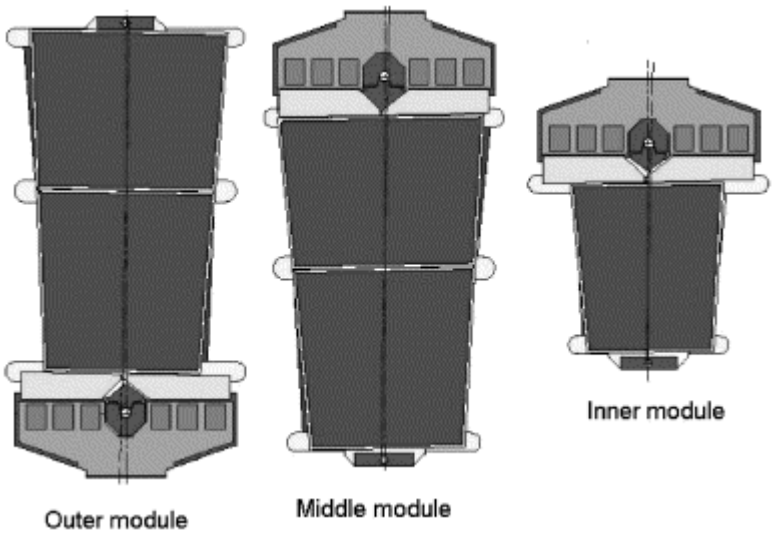

Figure 3.3: The three types of endcap SCT modules. The detector active strip length is 121.1 mm for outer modules, 116.7 mm for inner modules and 72 mm for inner modules.

3.2.1 Detector Specifications

An endcap module is made up of two (in the case of inner modules) or four (in the case of middle and outer modules) wedge-shaped sensors of 285 μm thickness, glued back-to-back at a 40 mrad stereo angle. The strips run almost radially with strip pitch ranging from 55 μm in the inner ends to 95 μm in the outer ends, which are wider [17]. A photo of a forward module is given in Fig. 3.4, and an expanded view of the module parts is shown on Fig. 3.5.

The back-to-back sensors are sandwiched around a central spine which serves as both mechanical support and heat spreader. Spines are made of thermo-pyrolitic graphite (TPG) and aluminium nitride (AlN) to combine good thermal conductivity with mechanical strength. The main spine piece running along the module length is a 500 μm thick and 23 mm wide TPG bar to provide the high thermally conductive path between the silicon sensors and the cooling contact. Since TPG is a good electric conductor, it is also used for giving the biasing

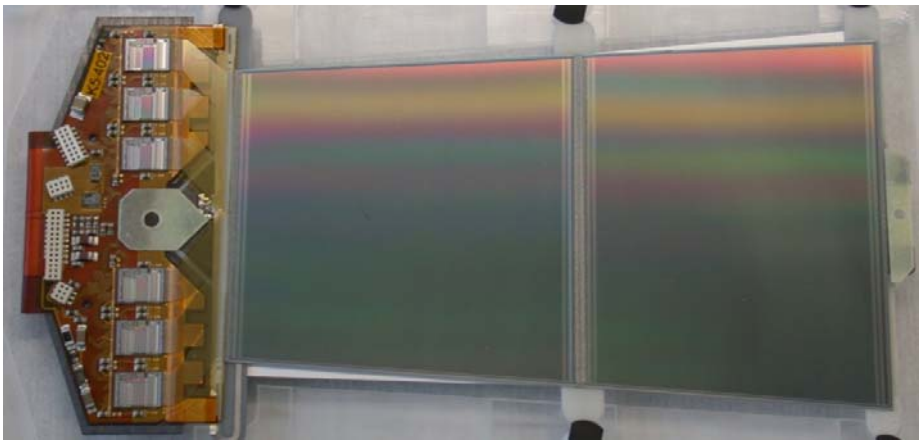

Figure 3.4: Photo of an endcap SCT module (in this case an outer module).

voltage to the sensors. Perpendicular to the TPG bar are the AlN components of the spine, which serve as mechanical support of the module.

The hybrid, which houses the front-end electronics, is positioned at one end of the module. The readout chips on the hybrid are situated on both sides of the module axis around the cooling contact, which also serves as the module mounting point. The electronics and hybrid design are described in the following Sections 3.2.2 and 3.2.3.

3.2.2 Readout Electronics

The SCT modules use binary readout, i.e. signals are discriminated in the front-end electronics, and only the hit/no hit information is passed to the DAQ system. This is done in 12 chips, each of which processes the information from 128 strips. Six of the chips are put on the top side of the hybrid, and the other six are on the bottom side of it.

The front-end integrated circuits (IC) perform the amplification and discrimination of signals, pipeline buffering and data formatting for transmission [10].

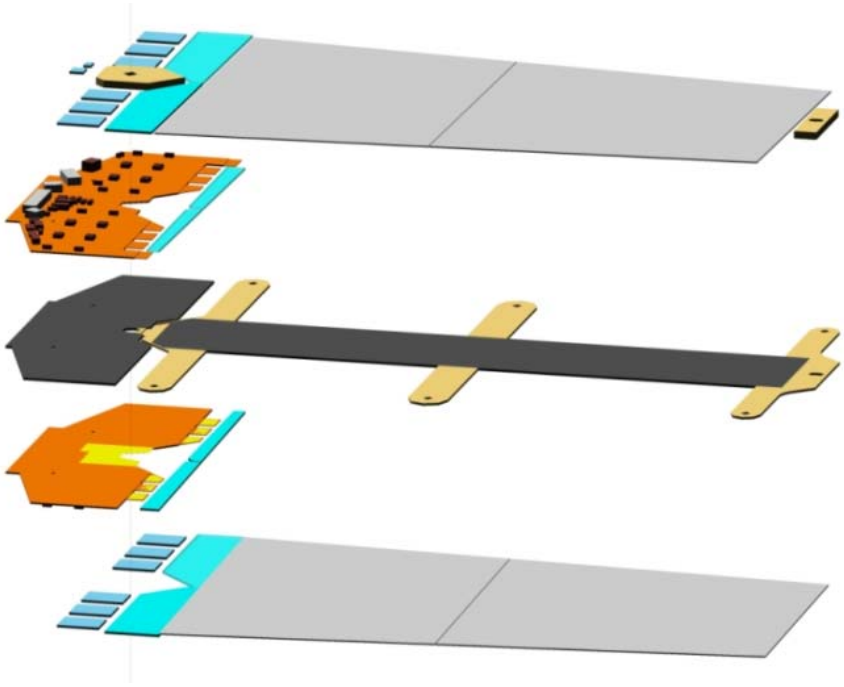

Figure 3.5: An exploded view of an endcap SCT module (in this case a middle module).

These functions are implemented in the ABCD3T-A chips used in the detectors. An ABCD3T-A [18] chip has 128 channels, each of which consists of a charge sensitive preamplifier-shaper circuit, a discriminator, a mask filter and a binary pipeline for storing the hit information.

The preamplifier-shaper processes the positive signals from p-type strips with a nominal gain of 50 mV/fC. Its noise is required not to exceed 1500 electrons RMS (root mean square) for unirradiated modules and 1800 electrons RMS for irradiated modules. At the comparator stage, signals are compared to a threshold voltage generated by an internal DAC (the nominal value is equivalent to 1 fC). A trim DAC exists for threshold correction in order to compensate for channel-to-channel variations.

The hit pattern is stored in a 132-bit deep FIFO binary pipeline. When an L1

trigger arrives, the information is copied to a readout buffer and then compressed and transmitted to the DAQ system. The chip also incorporates command and control functions and distributes the clock and calibration signals.

There are three types of chips with different functions: master, slave and end chips. The master initiates the readout cycle by passing information to the slave next to it, which passes it to the next one etc. until it reaches the end chip. The architecture implements a redundancy mechanism in the case of a chip failure. The ABCD3T-A chip is supplied with low voltages of 3.5 V for the analogue and 4 V for the digital circuits, and has an average power consumption of 3.2 mW per channel.

The chips use advanced technology which will keep them operating in the high-radiation LHC environment during 10 years of data taking. Moreover, their signal-to-noise ratio (S/N) must remain high: it is required not to decrease below the expected value of S/N = 12 at the end of the detector lifetime. The occupancy of the chips due to noise must be kept low (5×10^{-4}). The semiconductor tracker efficiency and noise occupancy depend strongly on the signal-to-noise performance of the front-end circuits.

3.2.3 Hybrids

There are two hybrids per module (on the top and bottom sides), with each hybrid holding six ABCD3T-A chips. The hybrid (Fig. 3.6) is put on a support board with two slots that act as thermal breaks to stop heat from the electronics from entering into the sensors. The thermal functions of the hybrid include conducting away the heat generated in the electronics to the primary cooling contact.

The hybrid plays the important electrical role of distributing the power and

Figure 3.6: Front and back views of the hybrids for an endcap SCT module.

ground to the chips, and some control and redundancy functions. It provides connection of the chips to the optical readout system, and also to the silicon strips via fan-in structures mounted on both sides of it.

Hybrids are made of a multilayer copper-kapton circuit wrapped around a thermally conductive carbon fibre substrate. The high thermal conductivity substrate makes direct contact with the cooling block through a thin layer of thermal grease. In total all the hybrid devices dissipate power of around 6.8 W [17], which is conducted away via the cooling contact.

Chapter 4

Thermal Performance of the SCT Cooling Block

Studies to optimise the SCT cooling block performance were carried out using finite element analysis simulations, and were then compared to previously measured data. The results have been published in ATLAS notes [19] and [20].

4.1 The SCT Cooling System

The SCT cooling system uses an evaporative cooling technique with coolant temperature of around $-20°C$. The C_3F_8 coolant flows through copper-nickel (CuNi) cooling pipes. They are soldered to a cooling block, lying on the module cooling contact area. Heat dissipated in the modules is conducted away, passing from the spine or hybrid, through the thermal grease and the cooling block into the pipes. The heat paths are indicated by arrows in Fig. 4.1 (middle and outer modules have an additional cooling point at the far end).

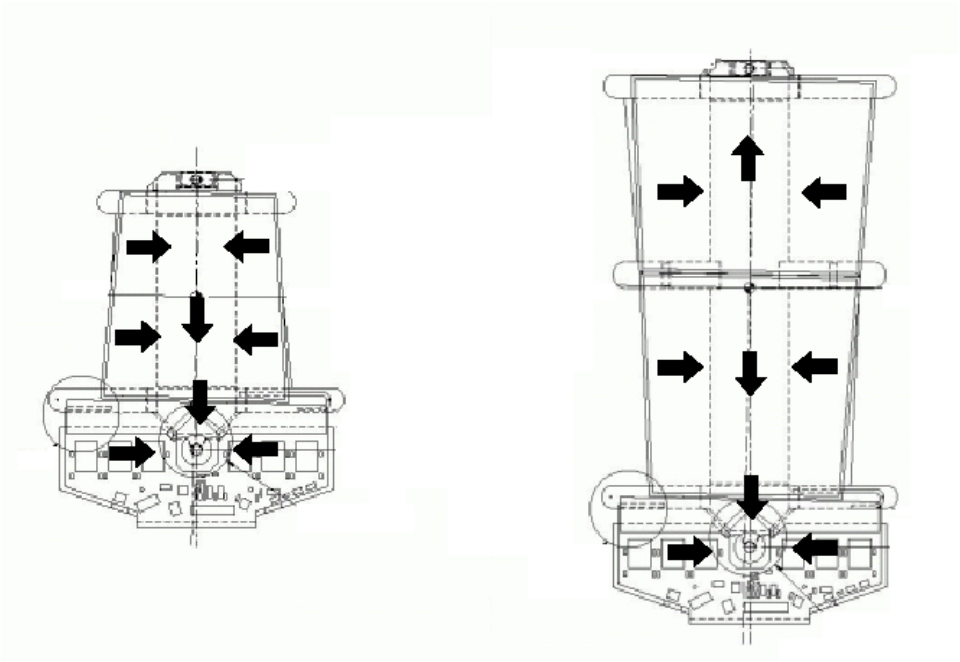

Figure 4.1: The thermal design concept for the inner (left) and outer (right) modules. The arrows indicate the directions in which heat is conducted to the cooling contact area.

The cooling system has two main functions: to conduct away the heat generated in the electronics through the hybrid, and to keep the silicon sensors at low temperature using contact with the spine. Firstly, the chips must be cooled to avoid excess thermal noise which would degrade their performance. The large power dissipated in the hybrid, expected to reach up to 7 W in the worst possible case [21], requires an effective and reliable cooling system.

The second, and more important, role of the module cooling is to maintain the operation of silicon sensors throughout their lifetime. This means keeping them sufficiently cool in order to avoid thermal runaway from the leakage current, which grows with irradiation, and to slow down the damaging process of reverse annealing. Cooling specifications require a good performance to the maximum power density of up to 185 $\mathrm{W\,m^{-2}}$ and bias voltage of up to 460 V, expected

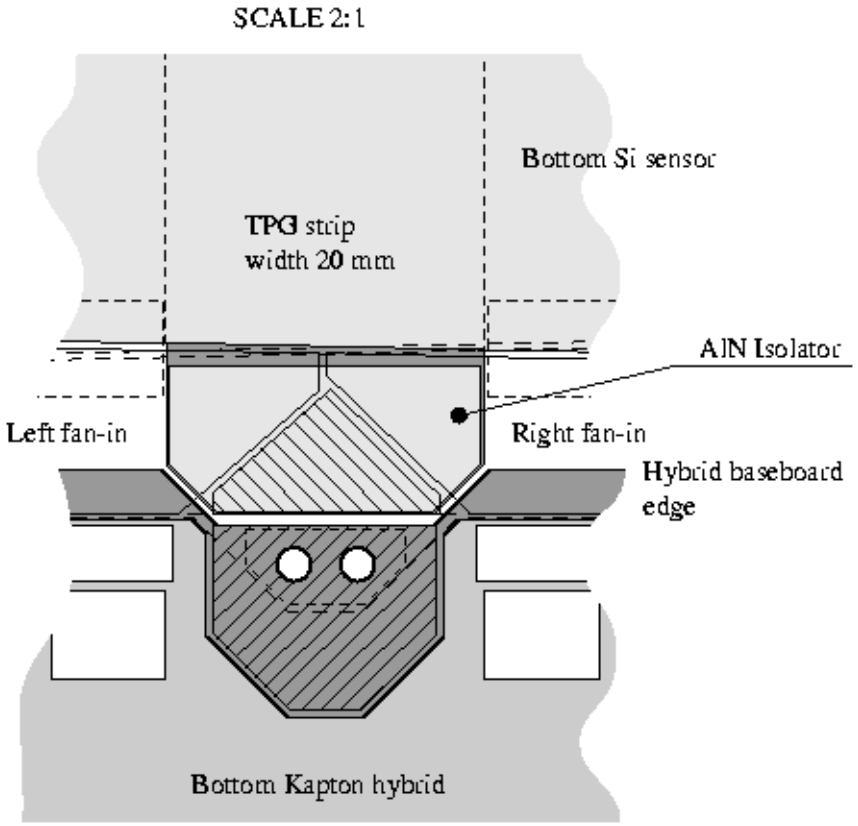

Figure 4.2: The contact area (hashed) between the cooling block and the module spine (grey) and hybrid (dark grey) [22].

after 10 years of operation [21]. To meet these requirements, the cooling system should keep the detectors at an operating temperature of $-7°$C or less.

The sensors receive heat not only from their leakage current, but also from the nearby chips, which are much hotter. That is why it is crucial to thermally decouple the heat paths from the electronics and the sensors. The thermal break is incorporated in the cooling block design, since the block surface makes contact with both hybrid and sensors (Fig. 4.2).

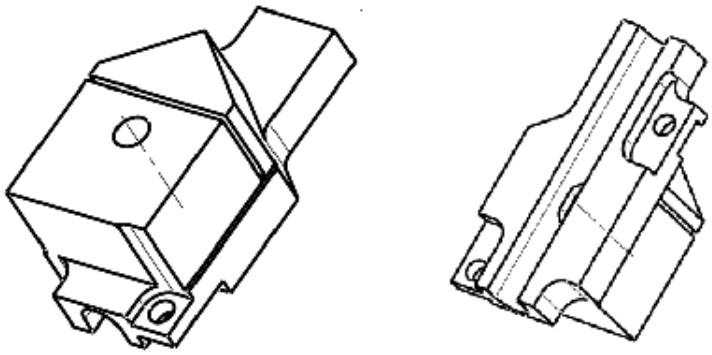

Figure 4.3: Drawings of the carbon-carbon cooling block. It has a length of 30 mm and a width of 14.2 mm.

4.2 Cooling Block Designs

The cooling block is made of carbon-carbon, which is layered so that its thermal conductivity is excellent in one plane but poor in the perpendicular direction. The effects of different orientations of the conducting plane were investigated in order to achieve lowest temperatures on the block-module contact surface.

The block design must ensure the most effective thermal break leading to the sensor part being colder than the hybrid part, in order to maintain the thermal stability of the sensors. This is done by splitting the block in two parts, the hybrid and the sensor regions. However, keeping the two parts separated would create difficulties with their alignment. Thus the block is split and a thin layer of low thermal conductivity material is placed between the two parts to act as an isolator, while keeping the block whole. The isolation material used is polyether ether ketone (PEEK) plastic. Two possible designs were studied, which differ with respect to the properties of the split and choice of material in it: a *baseline* design of a half-split block with air in the split, and a *new* design with a full PEEK split.

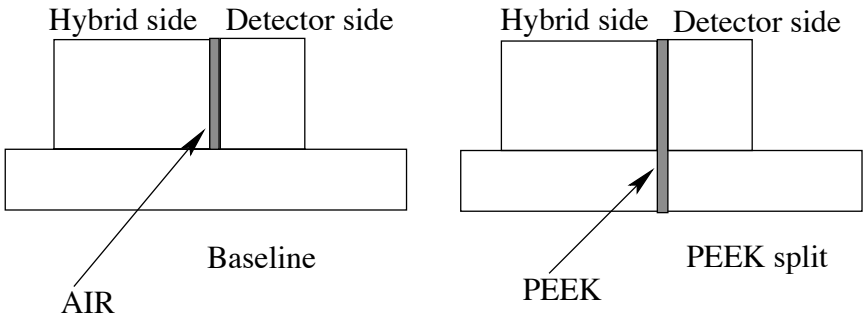

Figure 4.4: Thermal split positions in the baseline (left) and the new design block (right).

Drawings of the whole cooling block are shown in Fig. 4.3. The contact surface with the module is the front wall of the block in the left drawing: the upper part, above the split, cooling the sensors via the spine, and the lower part cooling the electronics on the hybrid. The extended narrow part of the block, shown in the right drawing, surrounds the cooling pipe.

The baseline design of the carbon-carbon block is only partially divided. Its split goes through the block region closer to the module, while the extended part around the cooling pipe is kept whole. The thickness of the air split is 0.5 mm (see the left picture in Fig. 4.4).

Since the baseline design might not provide the most effective thermal break, a new carbon-carbon block design was proposed. Here, the whole block is split, and it has a PEEK layer of 1 mm thickness (the right drawing of Fig. 4.4). Simulations were carried out in order to study which of the two designs had a better thermal performance in cooling the detector module.

A first prototype block of the new design was built, whose PEEK split was measured to be only 0.4 mm. It was also included in the simulations, in order to compare the simulation results with existing data on the prototype block.

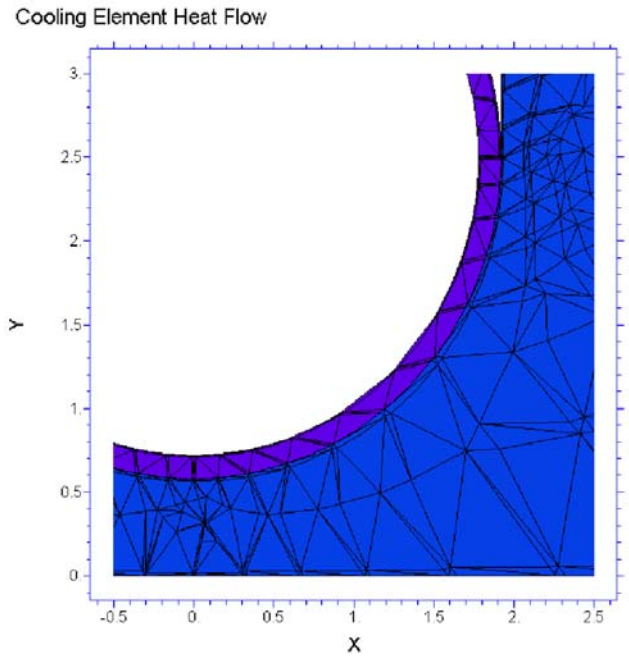

Figure 4.5: The FlexPDE finite element analysis representation of a part of the contact area between the block (blue) and the cooling pipe (purple), as seen from above. The division into small elements is shown by a mesh and the dimensions are given in millimetres.

4.3 Cooling Block Simulations

Finite element analysis simulations of the cooling block thermal performance were performed using the the software tool FlexPDE [23]. The objects under study included the carbon-carbon cooling block, a CuNi cooling pipe which passes through one side of it, a thin layer of Dow Corning DC340 grease, the two-layer (TPG and AlN) spine, and the carbon fibre hybrid.

The geometry of the objects is specified, and FlexPDE calculates their temperature distribution to an accuracy of 0.1°C. The three-dimensional model elements are resolved by a mesh which has a large number of cells due to the small sizes of some elements: the grease layer is only 30 μm thick, the pipe thickness

is 70 μm and the thicknesses of the AlN and TPG parts of the spine are 225 μm each. This creates difficulties for the programme and slows down its calculations considerably. The number of nodes in the model ranges from 73000 to 82000 for the different block designs, and the corresponding number of cells ranges from $\sim$ 48500 to over 54900. A closeup cross-section of the finite element analysis model, showing the division into small cells, is shown in Fig. 4.5.

The calculations are carried out by solving first order partial differential equations and specifying the boundary conditions. The equation solved in this thermal model was the heat flow equation:

$$\partial_x(K_x\partial_x T) + \partial_y(K_y\partial_y T) + \partial_z(K_z\partial_z T) + Q = 0\,, \tag{4.1}$$

where T is the temperature, $\vec{K} = (K_x, K_y, K_z)$ is the anisotropic thermal conductivity (in W mm^{-1}K^{-1}), and Q is the power density of the heat source (in W mm^{-3}). The natural boundary conditions for the heat flux $\vec{F}$ through the internal surface of the cooling pipe, between the pipe and the coolant, were specified as:

$$\vec{F} = -k\nabla T = \mathrm{HTC} \times (T_{\mathrm{coolant}} - T)\vec{n}\,, \tag{4.2}$$

where T_{coolant} is the coolant temperature, k is the (isotropic) thermal conductivity of the CuNi cooling pipe, HTC is the heat transfer coefficient and $\vec{n}$ is a unit vector orthogonal to the cooling pipe surface.

For all other boundary surfaces the heat flux $\vec{F}$ is set to zero. This is a simplification since there is heat transfer to and from the ambient gas, but this effect is believed to be negligible. Moreover, in this geometry, the cooling pipe extends 2 mm beyond the cooling block in both directions to account for the temperature change along the pipes outside the block.

The heat transfer coefficient, which relates the flow of heat between the coolant fluid and the walls of the cooling pipe, is not constant. Its exact variation

with temperature difference and power density is unknown because it depends on the complex mechanisms of heat transfer and the fluid properties. The approximate formulae, derived from measurements of HTC behaviour described in [24], are used in the calculations. Since the data was found to lie between two bounds, these linear parametrisations are used as the two extreme cases of HTC:

$$\mathrm{HTC}_{low} = \frac{1800}{1 - 0.033\Delta T}\,, \qquad \mathrm{HTC}_{high} = \frac{2500}{1 - 0.054\Delta T}\,, \tag{4.3}$$

where $\Delta T = T - T_{\mathrm{coolant}}$.

The HTC uncertainty probably comes from the fact that the coolant temperature in the pipes is not constant [22], so the measured values are rather scattered. The simulations were done separately for the two values of HTC. In Section 4.5 only the more pessimistic results, which give higher temperatures, are shown.

4.4 Geometry

The object simulated in three dimensions is the carbon-carbon block, on one side of which passes the cooling pipe. Its opposite surface makes contact with the two-layer spine and the hybrid via the 30-μm grease layer. Minor simplifications are made in the geometry of the block, making it more symmetric, but they do not affect the overall results.

The cooling pipes, passing through the block, are thin-wall CuNi capillaries with 1.5 mm inner diameter and wall thickness in the range 50–100 μm [22]. The wall thickness value used in the simulations was 70 μm.

The hybrid extends to the sides of the cooling block, and its ends contain heat sources equivalent to the chips. The spine is made of two thin layers: AlN (closer to the block) and TPG (away from the block), and extends in the direction of the

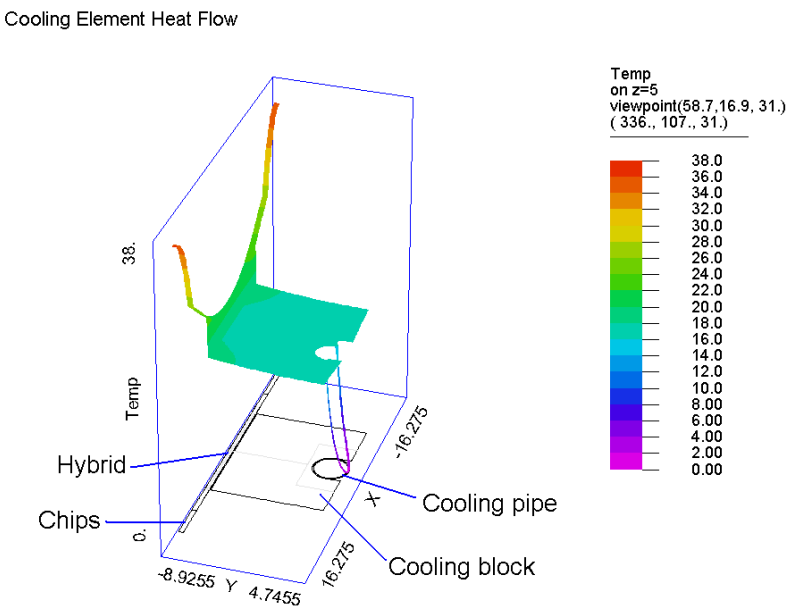

Figure 4.6: The temperature gradient in a cross-section of the hybrid part of the block. Heat flows from the lateral parts of the hybrid where the chips are, through the thin grease layer, the cooling block and into the cooling pipe.

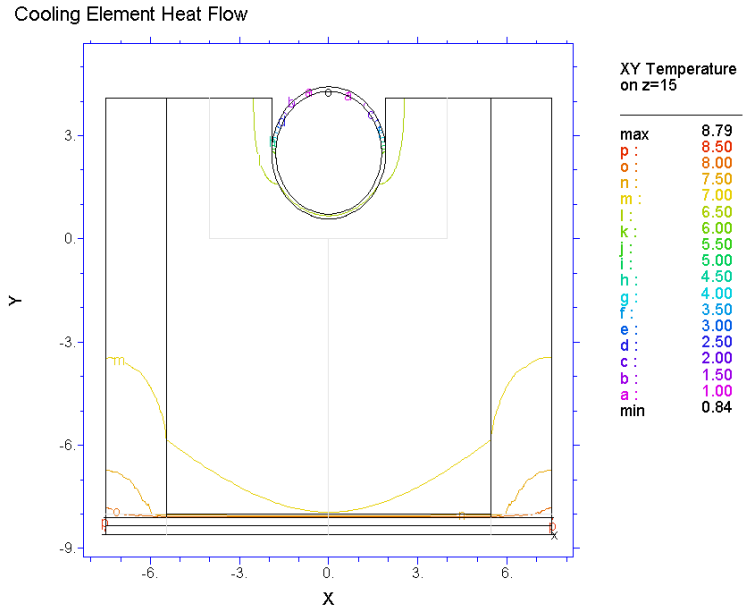

Figure 4.7: The temperature in a cross-section of the detector part of the block. Heat flows from the two-layer spine, through the grease and cooling block and into the cooling pipe.

Material	**Thermal conductivity** [W mm^{-1} K^{-1}]
carbon-carbon	0.20-0.40 in good directions y, z (0.12) 0.05-0.10 in poor direction x (0.07)
carbon fibre (hybrid)	0.7 in x 0.3 in y,z
AlN (spine)	0.18
TPG (spine)	1.7 in x, z 0.08 in y
CuNi (pipe)	0.03
PEEK	0.00025
grease	0.00042
air	0.000026

Table 4.1: Thermal conductivities of the materials.

silicon detectors (vertical in this case). Its upper part is made only of AlN and contains a heat source representing the heat dissipated in the detectors. In this way, heat flows in a realistic way from the sides through the hybrid, and from above through the spine, then enters the block through the grease and finally reaches the cooling pipe. A quasi-three-dimensional temperature distribution through a cross-section of the hybrid part of the block is shown in Fig. 4.6, and the temperature through a cross-section of the detector part of the block is given in Fig. 4.7.

The thermal conductivities of the materials used in the model are listed in Table 4.1. The values of the carbon-carbon thermal conductivity were taken from measurements of cooling blocks. Since the data were very inconsistent, the initial simulations have been separately performed for the low (0.20 $W\,mm^{-1}K^{-1}$ in good and 0.05 $W\,mm^{-1}K^{-1}$ in poor directions) and high (0.40 and 0.10) values. The results showed discrepancies smaller than 1°C for the two cases, thus the final simulations were done using average thermal conductivity values (0.30 and 0.075), with an error of 1°C. Later laboratory measurements obtained lower thermal

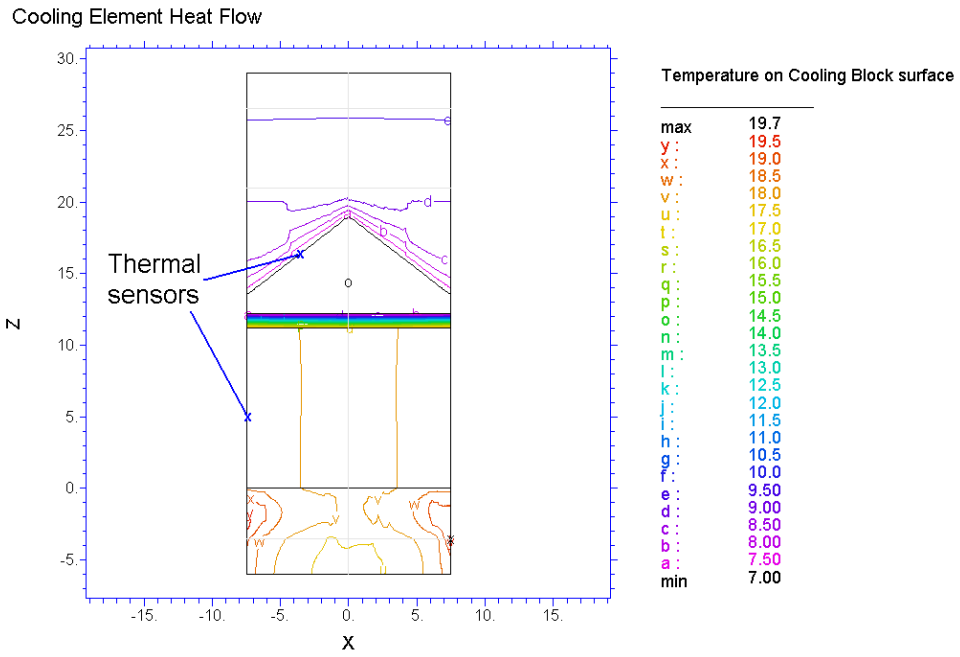

Figure 4.8: The temperature on the cooling block surface which is in contact with the module. The hybrid (lower) part is much hotter than the detector (upper) part, and there is a large temperature gradient in the PEEK split with low thermal conductivity.

conductivity values: 0.12 and 0.07 in the good and poor directions, respectively. All simulations were repeated for these values.

In this approximate model, two main simplifying assumptions are used. The first one is neglecting the heat dissipated on the module as a result of convection from the air. This is thought to be valid because most of the heat is produced in the chips, so it flows to the sensors primarily from the contact region between the hybrid and the sensors.

The second simplification in the simulation is not including the thin layer of solder between the cooling block and the pipes. This leads to an underestimation of the thermal contact areas connecting the hybrid and the sensors. Heat from the electronics could reach the silicon sensors via this path. In reality the thermal

Hybrid Power $[W]$	Det. Power $[W]$	**Baseline**		**Prototype**		**New design**	
		Hybrid Temp.	Detector Temp.	Hybrid Temp.	Detector Temp.	Hybrid Temp.	Detector Temp.
3.5	0	7.4	6.0	9.5	3.5	10.4	2.1
	1	8.6	7.2	9.9	5.2	10.6	4.1
	2	9.2	8.3	10.2	6.8	10.8	6.1
7	0	13.6	10.0	15.8	5.6	16.9	3.2
	1	14.1	11.0	16.0	7.2	17.0	5.2
	2	14.5	11.9	16.2	8.6	17.1	7.0

Table 4.2: Temperature simulation results for the three block designs.

break is not as complete as in the simulations, and this effect is more significant for the PEEK split block.

4.5 Results

The thermal simulations were performed in order to compare the expected temperature distributions across the cooling block with existing data from measurements of the baseline design and prototype blocks. Temperatures were measured with thermal sensors at two points on the surface of the block: in the hybrid part and in the detector part (see Fig. 4.8).

The simulation results, for carbon-carbon thermal conductivity of 70 $\mathrm{W\,m^{-1}K^{-1}}$ in the poor direction and 120 $\mathrm{W\,m^{-1}K^{-1}}$ in the good directions, are given in Table 4.2. The new design of a 1-mm PEEK split block thermally separates the hybrid part from the detector part much more efficiently than the baseline semi-split with air design. It achieves up to $\sim 4^{\circ}$C cooler temperatures on the detector side compared to the baseline design, while the hybrid side remains warmer. The temperature difference between the hybrid side and the detector side of the cooling block ranges from 4.7°C to 13.7°C for the 1-mm PEEK split

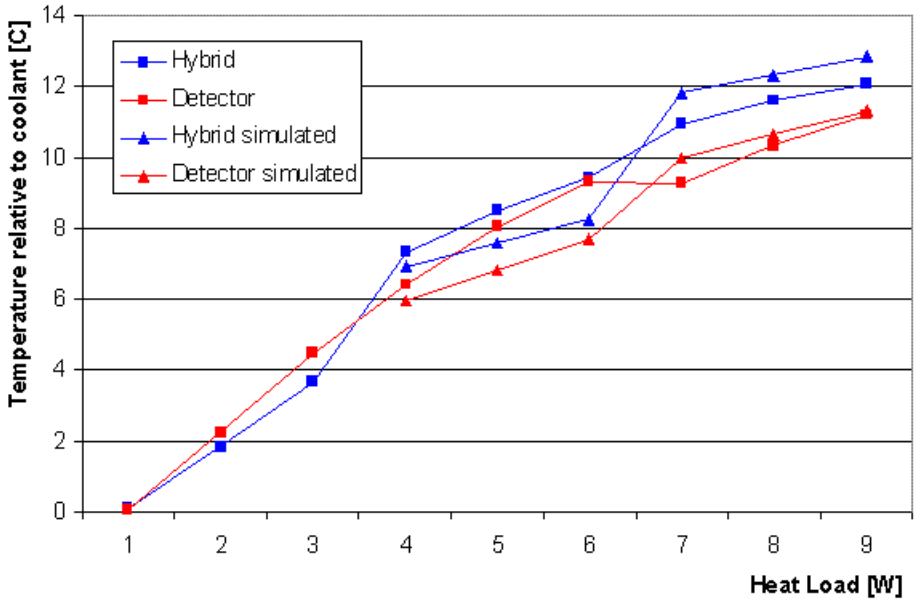

Figure 4.9: The cooling block temperature relative to the coolant for the baseline design block (measurements and simulations).

design.

The results for the cooling block temperature relative to the coolant temperature, as a function of the total power dissipated in the module, are shown in Fig. 4.9 for the baseline design and in Fig. 4.10 the first prototype block. The figures show a comparison of the values obtained by the simulations and the measurements previously made in [19].

Good agreement is seen between the simulations and data for the baseline design. The lesser degree of agreement between the simulations and the measurements for the prototype block is due to the fact that there are additional heat paths between the hybrid and the detector parts of the block, which have not been included in the simulation model. These are the omitted solder layer between the block and cooling pipe, and the heat transfer to the silicon sensors by convection and radiation at high hybrid temperatures. It is also possible that

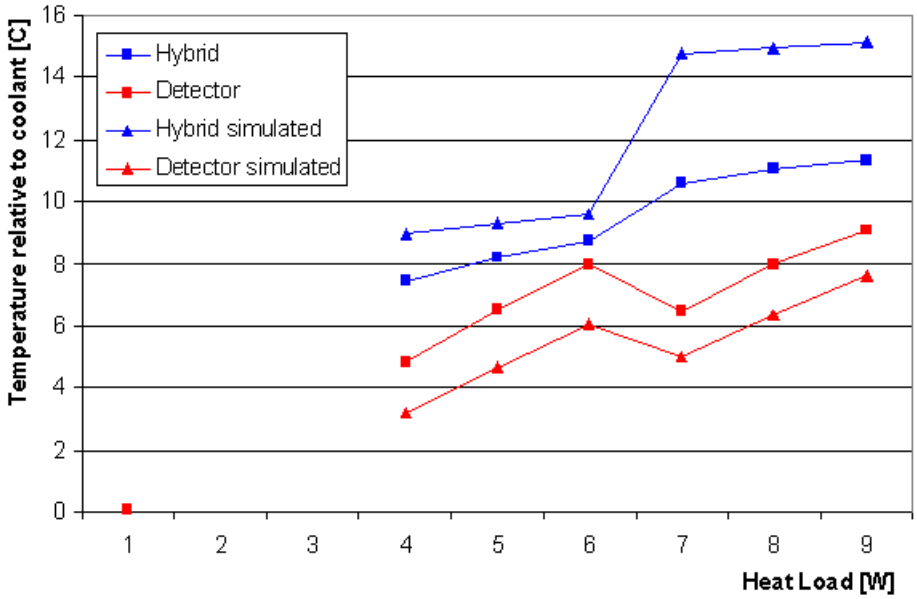

Figure 4.10: The cooling block temperature relative to the coolant for the prototype, 0.4-mm PEEK split block (measurements and simulations).

the actual PEEK thickness in the prototype is less than 0.4 mm, providing a less effective thermal break.

4.6 Discussion

Most important for the performance of the cooling block is the case of highest power dissipated in the hybrid (7 W). The temperatures on the detector side of the block, as a function of the detector heat load, are shown in Fig. 4.11. The figure shows a comparison of simulations and measurements for the three types of cooling blocks. It can be seen that, for the highest powers, the surface of the 1-mm PEEK split block is about 9°C hotter than the coolant. Therefore, allowing for an extra 30 % safety margin [21], the detectors can be safely operated with a 1-mm PEEK split block and the coolant at about −22°C (or with a baseline

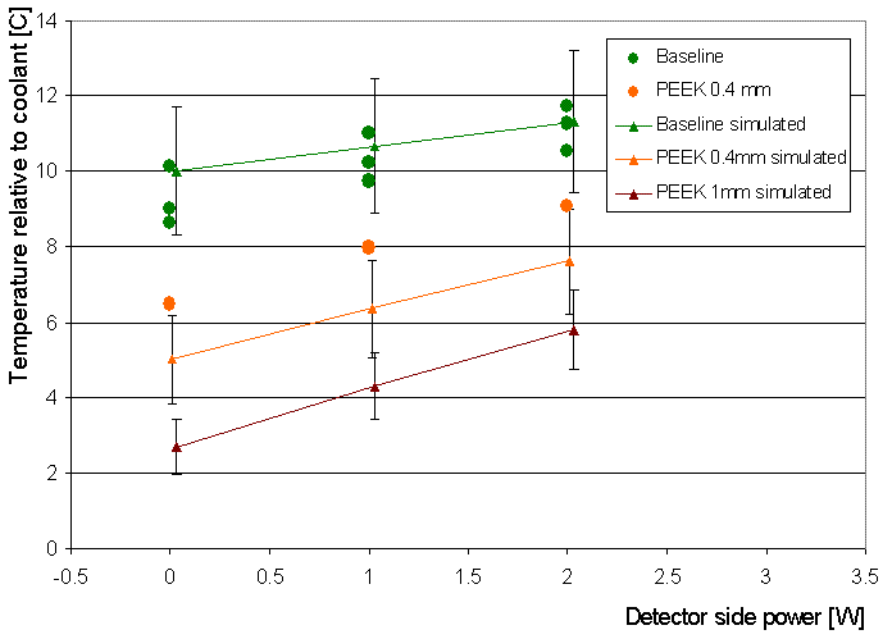

Figure 4.11: The temperature relative to the coolant on the sensor side of the three types of cooling blocks for 7 W dissipated at the hybrid side (measurements and simulations). The error bars reflect the uncertainty in HTC.

block and the coolant at $-24°$C).

The cooling block simulations show the advantages of using a PEEK split block over the baseline, semi-split block. Results agree well with data for the baseline carbon-carbon block. There is some discrepancy between the simulation results and measured temperatures for the prototype PEEK split block, due to underestimation of the cross-talk in the cooling block. Allowing for this discrepancy, the 1-mm PEEK split block is shown to provide sufficiently decoupled thermal paths for detectors and hybrids, achieving an improvement of almost 4°C over the baseline block.

It can be concluded that SCT detectors will operate safely at the specified coolant temperature of $-22°$C. Taking the results of this study into account, the 1-mm PEEK split block design has been implemented in SCT module production.

Chapter 5

SCT Studies of Common Mode Noise

This chapter describes studies of common mode noise for the ATLAS endcap SCT. Common mode noise was measured in four modules by analysing coherent fluctuations in the occupancies of groups of channels.

5.1 SCT Noise Measurements

In silicon detectors with binary readout, only the position and beam crossing identifier of the hits are recorded, but not the signal pulse heights. Thus a lot of useful information that could have been used to subtract the noise background is lost. This creates difficulties in analysing the noise and has led to the development of sophisticated techniques for its evaluation.

The single channel noise can be determined using the laboratory calibration system, by measuring the occupancy as a function of the threshold. This is done in the Three Point Gain test [25], which obtains the noise by performing a threshold

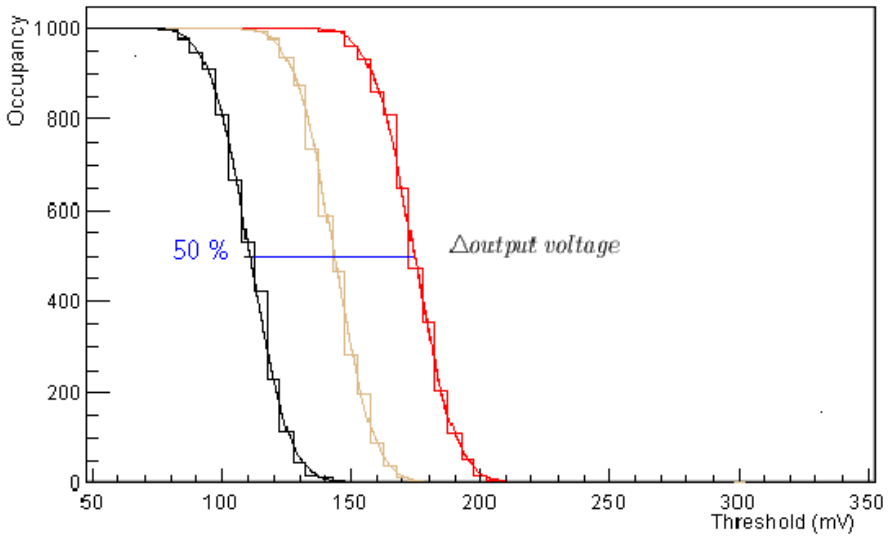

Figure 5.1: S-curves for injected calibration charges of 1.5 fC (black curve), 2 fC (yellow curve) and 2.5 fC (red curve).

scan with a calibration signal injected into the chip amplifiers. The calibration charge passes through the amplifier-shaper circuit, where it is converted to a voltage, and is then compared to the discriminator threshold voltage. A threshold scan records the data taken with a given calibration charge, and for a number of thresholds increasing in small steps. The detector occupancy for a given threshold is the event-averaged fraction of channels that register a hit.

Ideally, the resulting occupancy from a threshold scan, plotted as a function of the threshold, should give a step function: 1 for a threshold voltage smaller or equal to the calibration voltage, and 0 for larger thresholds. In reality the electronics circuit noise smears out this function, producing an S-curve (Fig. 5.1). The spread of this curve is equal to the noise amplitude.

Random noise has a Gaussian distribution $P(x) = \frac{1}{\sigma\sqrt{2\pi}}\exp\{-\frac{(x-\mu)^2}{2\sigma^2}\}$ with width σ and median μ. Therefore the resulting occupancy $O(x)$, equivalent to the probability of surpassing a threshold x, is given by the complementary error

function

$$O(x) = \frac{1}{2}\mathrm{erfc}(x) = 1 - \frac{2}{\sigma'\sqrt{\pi}} \int_x^\infty \mathrm{e}^{-\frac{(x-\mu)^2}{\sigma'^2}} dx \tag{5.1}$$

Fitting the S-curve to a complementary error function gives the noise magnitude σ' and the median μ (which is also the 50% occupancy point in the threshold scan).

Here the width σ' corresponds to the standard deviation of output noise, after it has been amplified in the chip, while σ is the magnitude of the input noise. The two values are related by the chip gain G, defined as:

$$G = \frac{\Delta V_{\mathrm{output}}}{\Delta Q_{\mathrm{input}}}, \tag{5.2}$$

where $\Delta Q_{\mathrm{input}}$ is the difference in input charge, and the voltage difference $\Delta V_{\mathrm{output}}$ is taken at the 50% occupancy points of the curves (see Fig. 5.1).

Knowing the gain and the output noise σ', the input noise σ can be calculated from:

$$\sigma = \frac{\sigma'}{G}. \tag{5.3}$$

The Three Point Gain test obtains the gain and noise using three different calibration charges. There is also another, more precise test, called the Response Curve, which does the same for ten different injected charges. Both tests are implemented in the SCT data acquisition system (described in Section 5.4) and are part of the standard quality assurance procedure for the modules.

5.2 Common Mode Noise

Common mode noise is the noise that affects several channels at the same time. It can be caused by cross-talk between channels, common electromagnetic pick-up, poor shielding, noise on the supply voltages, etc. If common mode noise becomes

large, it can even cause artificial hits in the readout. That is why reducing common mode noise is a critical issue for the SCT.

Since the readout is binary, common mode noise is difficult to distinguish from random noise and to eliminate. No information is available on the signal pulse heights, so real hits cannot be separated from those caused by noise, and common mode noise cannot be measured on an event-by-event basis. Moreover, common mode noise depends on the environment as well as the detector module, so it may differ in laboratory testing conditions from the conditions in the actual experiment. The spectrum of common mode noise is generally unknown, and most difficult to detect is Gaussian noise.

Several methods have been developed to estimate the magnitude of common mode noise in silicon detectors with digital readout [26]. If the single channel random noise is known, any excess can be attributed to common mode noise. Unfortunately, in most cases random noise is unknown because it cannot be separated from common mode noise; only the superposition of the two is measured.

A method of detecting non-Gaussian common mode noise is by plotting the logarithm of the occupancy versus the square of the discriminator threshold. The probability of a hit for threshold τ (normalised to the single channel random noise σ) is given by the complementary error function $p(\tau) = \frac{1}{2}\mathrm{erfc}(\frac{\tau}{\sqrt{2}})$. For large enough thresholds $\tau \gg 1$, this probability can be approximated by [26]

$$p(\tau) \approx \frac{1}{\tau\sqrt{2\pi}} \exp\left(-\frac{\tau^2}{2}\right). \tag{5.4}$$

So taking the logarithm would give

$$\ln(p) \approx -\frac{1}{2}\tau^2 - \ln(\tau\sqrt{2\pi}), \tag{5.5}$$

and the plot of the logarithm of the occupancy versus the threshold squared should give a straight line if only random, Gaussian noise is present. Any deviations

from a straight line are due to non-Gaussian common mode noise. However, this method cannot detect Gaussian common mode noise, which causes only a change of the line slope. It is also not sensitive to coherent effects in the noise.

It was shown in [27] that any common mode noise can be approximated by a Gaussian when it represents a small part of the total noise. The following Section 5.3 describes the coherent occupancy method for measuring Gaussian common mode noise, which was applied to modules at the endcap SCT system test. The analysis and results of system test data are presented in Section 5.5, and the results when noise was artificially injected into the system are given in Section 5.6.

5.3 The Coherent Occupancy Method

Common mode noise can be detected as coherent fluctuations of the channel occupancies from event to event. In the absence of common mode noise, there should be no such fluctuations as random noise does not change with time. Coherent noise causes a lot of channels to register hits in some events, while in others very few hits are recorded. Therefore the distribution of the number of hits per event N_e can be used to indicate the presence of common mode noise in the system [26].

If there is only Gaussian single-channel random noise, the N_e distribution is binomial: $P(N_e) = \mathrm{Bin}(N_e; n, p(\tau))$ for n channels and hit probability $p(\tau)$ at the given threshold τ. Then the mean number of hits per event $\overline{N}_e$ is determined using binomial statistics:

$$\overline{N}_e = \sum_{N_e=0}^{n} \mathrm{Bin}(N_e; n, p(\tau)) = np(\tau)\,, \tag{5.6}$$

and the variance of the distribution can be expressed in terms of $\overline{N}_e$ as

$$\mathrm{Var}(N_e) = np(1-p) = \overline{N}_e \left(1 - \frac{\overline{N}_e}{n}\right) . \tag{5.7}$$

Thus the expected standard deviation of N_e can be directly calculated from the measured average fraction of channels registering a hit, $\overline{N}_e$. Widening of the observed N_e distribution is an indication of common mode noise pick-up.

If common mode noise is Gaussian, its magnitude can be derived from the N_e distribution. The distribution of random noise is given by

$$P(x) = \frac{1}{\sqrt{2\pi}} \exp\left(-\frac{x^2}{2}\right) . \tag{5.8}$$

Without common mode pick-up, the occupancy above a threshold τ is given by the complementary error function, $O(\tau) = \frac{1}{2}\mathrm{erfc}(\tau/\sqrt{2})$. When adding common mode noise with a Gaussian distribution of

$$P(z) = \frac{1}{s\sqrt{2\pi}} \exp\left(-\frac{z^2}{2s^2}\right) , \tag{5.9}$$

the total noise becomes a convolution of the two,

$$P(a) = \frac{1}{\sqrt{2\pi(1+s^2)}} \exp\left(-\frac{a^2}{2(1+s^2)}\right) , \tag{5.10}$$

where $a = x + z$. Here all noise has been normalised to the random noise σ, and s is the width of common mode noise (also in units of σ). The resulting occupancy is then

$$O(\tau) = \frac{1}{2}\mathrm{erfc}\left(\frac{\tau}{\sqrt{2(1+s^2)}}\right) . \tag{5.11}$$

Adding common mode noise to the random noise is equivalent to shifting the discriminator threshold by the same amount in the opposite direction. For Gaussian common mode noise, this can be represented by giving the threshold τ a Gaussian distribution:

$$g(\tau) = \frac{1}{s\sqrt{2\pi}} \exp\left(-\frac{(\tau-\tau_0)^2}{2s^2}\right) , \tag{5.12}$$

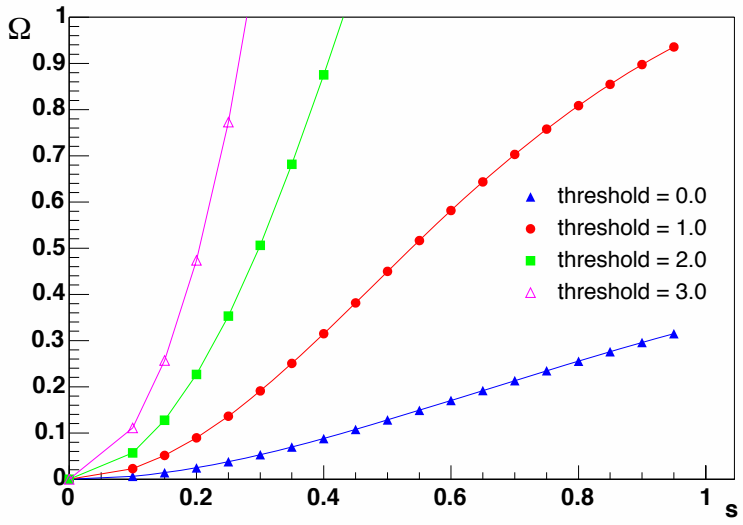

Figure 5.2: The observable Ω as a function of common mode noise.

in which τ_0 is the original threshold.

Therefore the N_e distribution becomes a superposition of binomial distributions for thresholds that vary with a probability distribution $g(\tau)$:

$$P(N_e) = \int_{-\infty}^{\infty} \mathrm{Bin}(N_e; n, p(\tau)) g(\tau) d\tau \,. \tag{5.13}$$

The mean value of N_e is then

$$\overline{N}_e = \sum_{N_e=0}^{n} N_e P(N_e) = \int_{-\infty}^{\infty} \mathrm{Bin}(N_e; n, p(\tau)) g(\tau) d\tau = \int_{-\infty}^{\infty} np(\tau) g(\tau) d\tau \,, \tag{5.14}$$

and the variance $\mathrm{Var}(N_e) = \overline{N_e^2} - \overline{N}_e^2$ can be written in the form

$$\mathrm{Var}(N_e) = \overline{N}_e(1 - \overline{N}_e) + n(n-1) \int_{-\infty}^{\infty} p^2(\tau) g(\tau) d\tau \,. \tag{5.15}$$

An observable Ω, which gives an estimate of common mode noise, was introduced in [27]:

$$\Omega = \frac{n}{n-1} \left(\frac{\mathrm{Var}(N_e)}{\overline{N}_e^2} - \frac{1}{\overline{N}_e} + 1 \right) - 1 \,. \tag{5.16}$$

If the common mode noise contribution is zero, then the observed variance matches the one expected from binomial statistics, and so Ω is always zero (independent of the applied threshold or number of channels). With the addition of common mode noise, Ω increases strongly.

The dependence of the observable Ω on the common mode noise contributions is shown in Fig. 5.2 for different thresholds. It can be seen that the sensitivity of Ω to common mode noise grows with increasing the threshold. This feature makes Ω ideally suited for use at the SCT operating conditions, which require high discriminator thresholds. The size of common mode noise, averaged per chip, is extracted from the Ω observable using an iterative technique.

5.4 Experimental Setup

Specific hardware and software have been developed for the general electrical tests of SCT endcap modules. The readout system consists of the VME modules CLOAK, MuSTARD, SLOG and the high and low voltage supply modules SCTHV and SCTLV [25, 28]. The system is represented schematically in Fig. 5.3.

The CLOAC (CLOck And Control) master card provides the 40.08 MHz clock commands to the modules and generates fast commands for the electrical tests. It is designed to enable module testing in the absence of the ATLAS timing, trigger and control system, that is, at laboratories outside the central experiment. The SLOG (SLOw command Generator) module distributes the clock and fast commands generated by CLOAC, and generates commands for control and configuration of the detector readout chips. The MuSTARD (Multichannel Semiconductor Tracker ABCD Readout Device) receives data from the detector modules, decodes the events, builds histograms of the data, and sends information

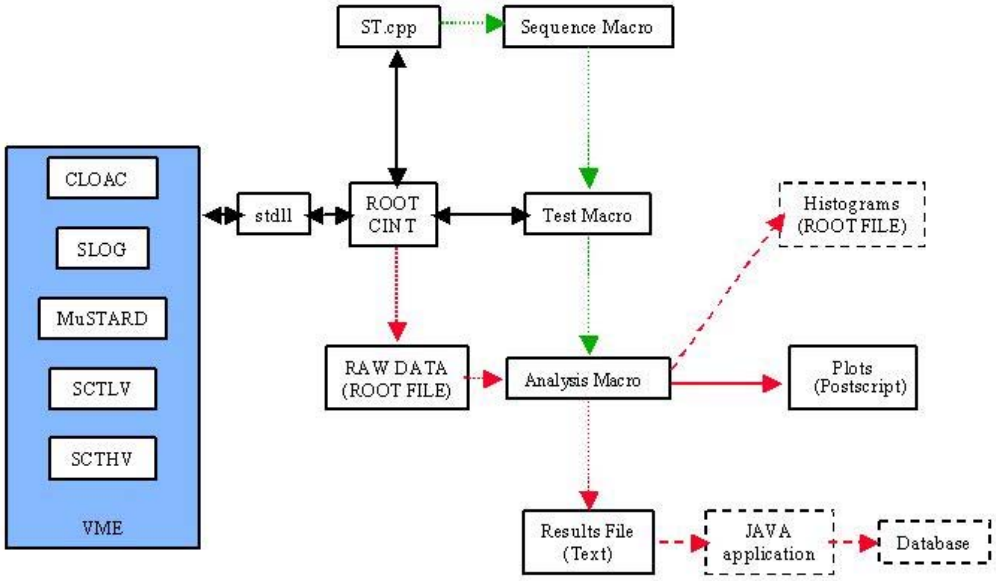

Figure 5.3: The experimental setup for SCT endcap module tests showing the SCTDAQ schematic [25].

to the data acquisition computer.

The module under investigation is connected to the data acquisition system through a forward kapton support card, which allows for either electrical or optical readout. For the case of single module testing in Manchester, the electrical readout was used, while at the SCT system test at CERN data were taken using the optical readout.

Configuring and testing of the detector modules was performed with the data acquisition software package SCTDAQ. The package contains a number of C++ macros for communication with the VME modules and for implementing the electrical tests. SCTDAQ is started from a ROOT [29] interface, allowing commands to be sent by pressing a button from a menu or by typing them directly in the terminal.

The output of each scan is saved as a ROOT file containing the scan configuration conditions and data. Then a separate ROOT macro can access the raw data file for further analysis, the results of which are kept in a text file. A Java application can be called through ROOT to upload the test results to the SCT production database.

5.5 Analysis and Results

The coherent occupancy method, using the observable Ω, was applied to four (two inner and two outer) detector modules mounted on a disk at the endcap SCT system test. Samples of data were taken by recording the full hit information for every event and channel. The noise analysis was then performed using ROOT-based C++ macros within the frame of SCTDAQ.

Although it would be desirable to measure noise at the SCT operating threshold of 1 fC, this is not possible due to the small number of hits. The low occupancy at $Q_{\mathrm{thr}} = 1$ fC does not allow noise to be measured with sufficient accuracy even when taking large data samples. That is why the tests were repeated at smaller thresholds of $Q_{\mathrm{thr}} = 0.4$, 0.6 and 0.8 fC. The coherent occupancy method implies that results should be independent of threshold [27].

Fig. 5.4 shows the common mode noise pick-up per chip at thresholds of 0.6 and 0.8 fC. Modules k5_314 and k5_316 in the plot are inner SCT modules, while k5_400 and k5_402 are outer modules. Noise pick-up is given in units of electron charge at the input, equivalent noise charge (ENC). Within the statistical errors, common mode noise pick-up does not vary with threshold, as expected.

Fig. 5.5 compares the common mode noise, averaged per chip at 0.6 fC, with noise measured at the lower threshold of 0.4 fC. There is an unexpected

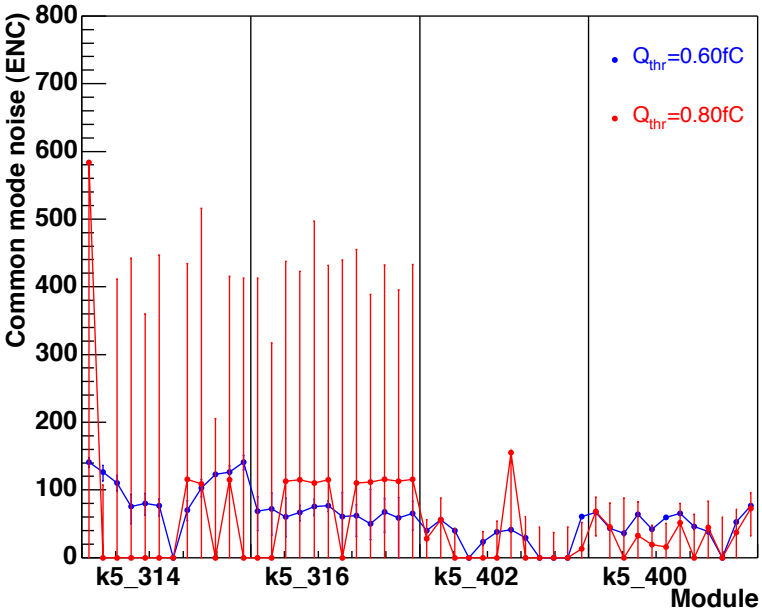

Figure 5.4: Common mode noise, averaged per chip for the four modules, measured from 10 million events at thresholds of 0.6 fC and 0.8 fC. The noise pick-up per chip is quoted in units of equivalent noise charge (ENC).

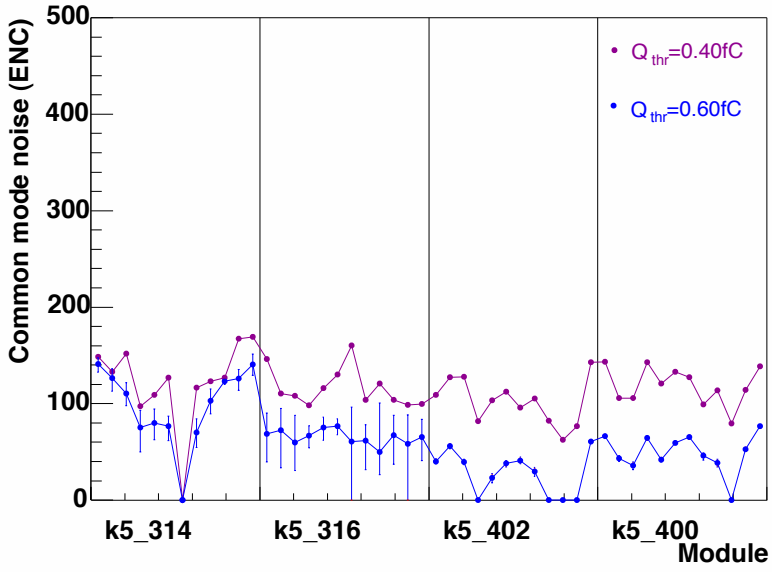

Figure 5.5: Common mode noise, averaged per chip for the four modules, at thresholds of 0.4 fC (1 million events) and 0.6 fC (10 million events).

dependency on the applied threshold: common mode noise is up to a factor of two higher at the low threshold. The variation of results with threshold can be explained by the fact that the gains of channels within a chip differ slightly [27]. The difference arises from the trimming procedure of equalising channel offsets in order to get identical thresholds. Trimming is done at the nominal threshold of 1 fC, therefore the results obtained at much lower thresholds are not reliable.

At system test operating conditions, common mode noise was found to be almost negligible. At 0.4 and 0.6 fC thresholds (where the noise error bars are small enough), all chip-averaged values for coherent noise are smaller than 200 ENC. For comparison, adding common mode noise of 200 ENC in quadrature to random noise of 1500 ENC (a typical value for the SCT), leads to total noise of only 1513 ENC, which is an insignificant increase.

5.6 Measurements with Noise Injection

To simulate the high noise levels of ATLAS and to test the validity of the coherent occupancy method, the measurements were repeated with noise forced into the system. A sinusoidal noise current of known frequency and amplitude was injected into the power supply tapes of the modules. Noise was induced by running the current from a signal generator through a coil around the system test power tapes.

Noise scans were done to determine the increase in noise due to the injected coherent noise. The noise was found by a calibration scan with 2 fC injected charge, and was then converted to input noise (in units of equivalent noise charge ENC) using the known gain. The common mode noise pick-up was evaluated using the Ω coherent occupancy method.

Fig. 5.6 shows the common mode noise for noise injection of a current of

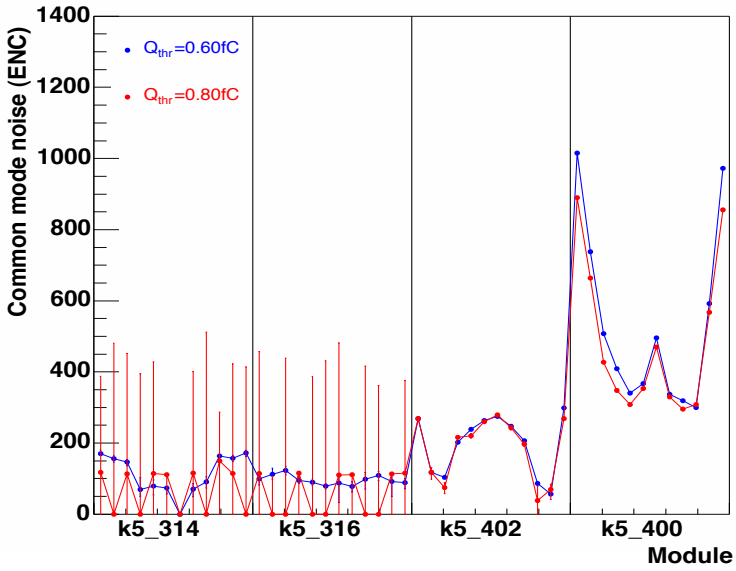

Figure 5.6: Common mode noise pick-up per chip, measured with noise injection of a sinusoidal signal of frequency 6 MHz and amplitude 10 V peak-to-peak. Noise measurements are made for thresholds of 0.6 fC and 0.8 fC, by reading out 10 million events for each threshold.

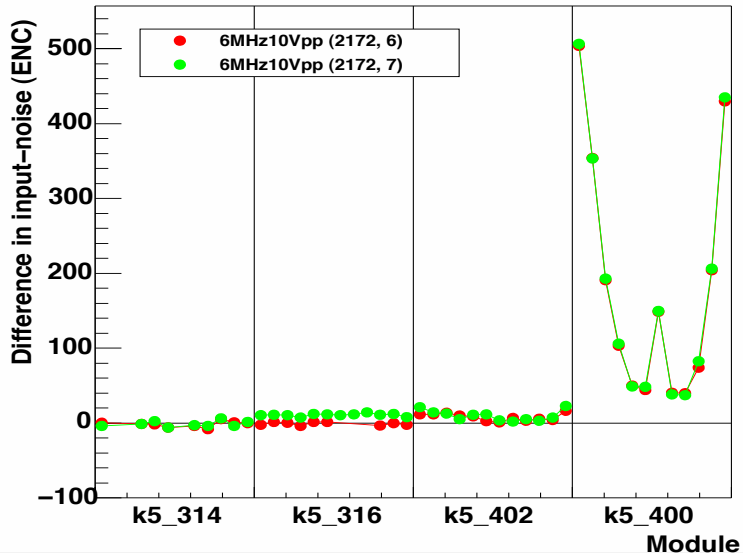

Figure 5.7: Increase in input noise when a signal of frequency 6 MHz and amplitude 10 V peak-to-peak is injected into the shielding of the system test (2 scans). The zero line corresponds to the reference scan without noise injection.

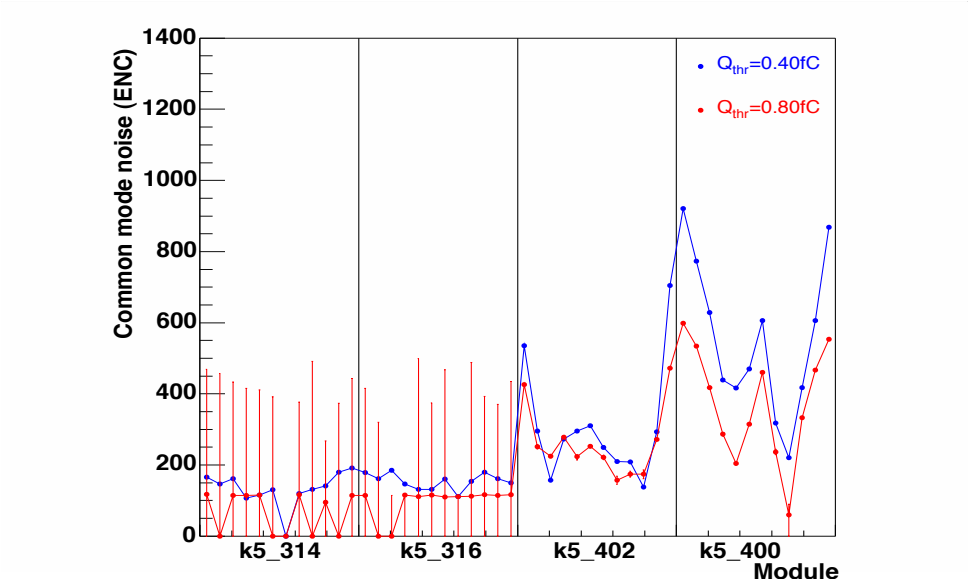

Figure 5.8: Common mode noise pick-up per chip, measured with noise injection of a sinusoidal signal of frequency 10 MHz and amplitude 10 V peak-to-peak. Noise measurements are made for thresholds of 0.4 fC (1 million events) and 0.8 fC (10 million events).

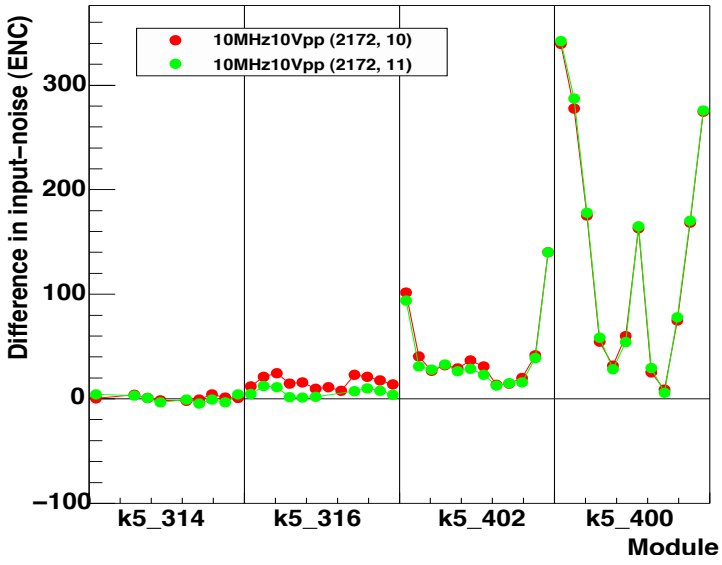

Figure 5.9: Increase in input noise when a signal of frequency 10 MHz and amplitude 10 V peak-to-peak is injected into the shielding of the system test (2 scans). The zero line corresponds to the reference scan without noise injection.

frequency 6 MHz and amplitude 10 V peak-to-peak. The results are for thresholds of 0.6 and 0.8 fC. It can be seen that outer modules (k5_400 and k5_402) pick up more coherent noise from the power tapes than inner modules (k5_314 and k5_316). The amount of common mode noise pick-up is highest in the edge chips on each side of the hybrid (numbers 0, 5, 6 and 11).

Fig. 5.7 shows the difference in input noise measured with and without noise injection of a 6 MHz, 10 V noise current. The value of coherent noise, calculated using the Ω variable in Fig. 5.6, agrees with the excess noise shown in Fig. 5.7. The measurements were repeated for noise injection of frequency 10 MHz and amplitude 10 V peak-to-peak. Figures 5.8 and 5.9 show the common mode noise and increase in noise, respectively. The two independently determined values are found to agree. Adding the common mode noise values in quadrature to random noise (measured without noise injection) gives the detected increase in noise.

5.7 Conclusion

Common mode noise was measured on four SCT modules at the endcap system test. The coherent noise pick-up was found to be within the ATLAS limit of 300 ENC, which is considered manageable. Noise injection did not affect the performance of inner modules, however outer modules showed significant noise pick-up from the power tapes. This is possibly due to less effective electrical shielding of the outer positions on the disk. Reducing common mode pick-up requires further investigation into the system test shielding, which is beyond the scope of this study.

Chapter 6

The Standard Model of Particle Physics

The theory which describes elementary particles and their interactions is called the Standard Model (SM). The particle content of the Standard Model can be divided into two groups: matter particles and force carriers. The elementary building blocks of matter, quarks and leptons, are fermions (with spin 1/2) and their interactions are mediated by the exchange of gauge bosons (with integer spin).

Table 6.1 shows the SM particle spectrum. Leptons participate in the weak interactions, mediated by the massive W and Z bosons. There are three generations of leptons, each containing a charged lepton (electron e, muon μ, tau τ) and a corresponding massless neutrino[1] (ν_e, ν_μ, ν_τ). Charged leptons and quarks also experience the electromagnetic interaction which is mediated by the massless photon. Quarks, too, make up three generations, in which up-type quarks (up u, charm c and top t) have $+2/3$ charge, while down-type quarks (down d, strange

[1] Although neutrinos are massless in the Standard Model, there is recent experimental evidence that they do have (very small) masses.

Type	Particle Name	Spin	Charge Q	Baryon Number B	Lepton Number L
Leptons	electron e^-, muon μ^-, tau τ^-	1/2	-1	0	1
	neutrinos ν_e, ν_μ, ν_τ	1/2	0	0	1
Quarks	up u, charm c, top t	1/2	+2/3	1/3	0
	down d, strange s, bottom b	1/2	-1/3	1/3	0
Gauge bosons	photon γ	1	0	0	0
	weak bosons $W^{\pm}$, Z^0	1	± 1, 0	0	0
	gluons g_i (i = 1,...,8)	1	0	0	0

Table 6.1: Elementary particles and some of their properties. Antiparticles of leptons and quarks (l^+, $\bar{\nu}_l$, and $\bar{q}$) have the opposite sign Q, B and L quantum numbers.

s and bottom b) have $-1/3$ charge. They cannot exist on their own, but instead are bound together by the strong interaction to form stable hadrons which can be baryons containing three quarks (qqq), or mesons containing a quark-antiquark pair ($q\bar{q}$). Quarks have the extra quantum number of colour which can take three possible values, red R, green G or blue B (the corresponding antiquark colours are anti-red $\bar{R}$, anti-green $\bar{G}$, and anti-blue $\bar{B}$). Bound states always contain colourless combinations of quarks and antiquarks. Gluons are the carriers of the colour charge, and they come in eight varieties corresponding to the linearly independent admixtures of colours:

$$\begin{array}{lll} \frac{1}{\sqrt{6}}(R\bar{R}+G\bar{G}-2B\bar{B}) & R\bar{B} & R\bar{G} \\ B\bar{R} & & B\bar{G} \\ G\bar{R} & G\bar{B} & \frac{1}{\sqrt{2}}(R\bar{R}-G\bar{G})\,. \end{array}$$

The Standard Model incorporates three of the four fundamental interactions: electromagnetic, weak and strong interactions (the fourth interaction, gravitation, has not been included in the SM so far). It uses the mathematical formalism of gauge theories—relativistic quantum field theories whose Lagrangians are invariant under local gauge transformations. The SM gauge group is the product

$SU_C(3) \otimes SU_L(2) \otimes U_Y(1)$ of the groups associated with colour, weak and hypercharge symmetries, respectively.

The Standard Model has been remarkably successful as a theory. Its predictions have been observed experimentally and confirmed by precision tests. There is, however, one aspect of it which is yet to be measured experimentally. In the Standard Model particles acquire mass via the Higgs mechanism which breaks electroweak symmetry. As a result, the model predicts the existence of a new massive scalar (spin zero) particle, the Higgs boson, which is yet undiscovered. The discovery of the Higgs boson is central to current experimental searches as without it the Standard Model is incomplete.

Sections 6.1 and 6.2 give a brief overview of quantum electrodynamics and quantum chromodynamics, respectively. QCD interactions at hadron colliders are described in Section 6.3. The electroweak model is introduced in Section 6.4, while the Higgs mechanism of electroweak symmetry breaking is given in Section 6.5. More detailed descriptions of the Standard Model can be found in textbooks such as the ones used in writing this chapter, [30, 31, 32, 33].

6.1 Quantum Electrodynamics

The gauge theory of the electromagnetic interaction which couples charged fermions and photons is quantum electrodynamics (QED). It is consistent with quantum mechanics, electrodynamics and special relativity. Its gauge group of symmetry is the Abelian group of unitary 1×1 matrices $U(1)$, implying that QED is invariant if the fields in it are redefined by a local phase,

$$\psi \rightarrow \psi e^{i\phi(x)} \, . \tag{6.1}$$

In line with special relativity, the theory is invariant under Lorentz transformations. This means that the space-time line element ds^2 is not affected by a change between Lorentz frames. The line element is

$$ds^2 = g_{\mu\nu} dx^\mu dx^\nu \tag{6.2}$$

for coordinates x^μ and metric $g_{\mu\nu}$.

The wavefunction of a free electron ψ is found by solving the Dirac equation for spin-1/2 particles

$$(i \not{\partial} - m)\psi = 0\,, \tag{6.3}$$

where $\not{\partial} \equiv \gamma^\mu \partial_\mu$, γ^μ are Dirac matrices and m is the electron mass. The Dirac matrices γ^μ are four 4×4 anticommuting matrices satisfying the relations:

$$\begin{gathered} \gamma^\mu \gamma^\nu + \gamma^\nu \gamma^\mu = 2g^{\mu\nu}\,, \\ \gamma^{0\dagger} = \gamma^0\,, \quad (\gamma^0)^2 = I\,, \\ \gamma^{k\dagger} = -\gamma^k\,, \quad (\gamma^k)^2 = -I\,, \quad k = 1,2,3\,. \end{gathered} \tag{6.4}$$

Here $g^{\mu\nu} = \mathrm{diag}(+1,-1,-1,-1)$ is the metric, I is the 4×4 unit matrix and the hermitian conjugate matrix is $\gamma^{\mu\dagger} = (\gamma^{\mu *})^{\mathrm{T}}$. The standard representation of Dirac matrices is in terms of the 2×2 traceless Pauli matrices σ_i:

$$\gamma^0 = \begin{pmatrix} I & 0 \\ 0 & -I \end{pmatrix}\,, \quad \vec{\gamma} = \begin{pmatrix} 0 & \vec{\sigma} \\ -\vec{\sigma} & 0 \end{pmatrix}\,, \tag{6.5}$$

$$\sigma_1 = \begin{pmatrix} 0 & 1 \\ 1 & 0 \end{pmatrix}\,, \quad \sigma_2 = \begin{pmatrix} 0 & -i \\ i & 0 \end{pmatrix}\,, \quad \sigma_3 = \begin{pmatrix} 1 & 0 \\ 0 & -1 \end{pmatrix}\,.$$

The Dirac equation (6.3) has two types of solutions: $\psi_1 = u_s(p)e^{-ip\cdot x}$ for a particle and $\psi_2 = v_s(p)e^{ip\cdot x}$ for an antiparticle. The functions u and v are four-component spinors which depend on particle four-momenta p and spins s as

$$u_s(p) \equiv \sqrt{E+m}\begin{pmatrix} \chi_s \\ \frac{\vec{\sigma}\cdot\vec{p}}{E+m}\chi_s \end{pmatrix}\,, \qquad v_s(p) \equiv \sqrt{E+m}\begin{pmatrix} \frac{\vec{\sigma}\cdot\vec{p}}{E+m}\chi_s \\ \chi_s \end{pmatrix}\,, \tag{6.6}$$

where $\chi_{1,2}$ are the basic two-component spinors for spin up and down,

$$\chi_1 = \begin{pmatrix} 1 \\ 0 \end{pmatrix}, \qquad \chi_2 = \begin{pmatrix} 0 \\ 1 \end{pmatrix}. \tag{6.7}$$

The antiparticle spinor v corresponds to negative energy solutions, therefore it is defined by taking $E \to -E$ and $\vec{p} \to -\vec{p}$. The spinors are orthogonal and normalised so that

$$u_r^\dagger(p)u_s(p) = v_r^\dagger(p)v_s(p) = 2E\delta^{rs}\,. \tag{6.8}$$

They satisfy the completeness relations

$$\begin{aligned} \sum_{s=1,2} u_s(p)\bar{u}_s(p) &= (\not{p} + m)\,, \\ \sum_{s=1,2} v_s(p)\bar{v}_s(p) &= (\not{p} - m)\,, \end{aligned} \tag{6.9}$$

where $\bar{u} \equiv u^\dagger\gamma^0$.

In order for the Lagrangian density of a free fermion

$$\mathcal{L} = \bar{\psi}(i\gamma^\mu\partial_\mu - m)\psi \tag{6.10}$$

to be invariant under $U(1)$ gauge transformations (6.1), a covariant derivative D_μ is introduced:

$$\partial_\mu \to D_\mu \equiv \partial_\mu + ieA_\mu\,, \tag{6.11}$$

where A_μ is the gauge field and e is a free constant, the fermion electric charge. The vector field A_μ is the photon wave-function which can be written in terms of the photon four-momentum q^μ as

$$A_\mu = \varepsilon_\mu(q)e^{-iq\cdot x}\,, \tag{6.12}$$

where ε_μ is the polarisation vector of the photon.

Imposing the covariant derivative in the Lagrangian (6.10) leads to an interaction term between fermions and photons,

$$-e\bar{\psi}\gamma^\mu A_\mu\psi\,. \tag{6.13}$$

The Lagrangian of quantum electrodynamics also contains a kinetic term for the photon field,

$$-\frac{1}{4}F_{\mu\nu}F^{\mu\nu}\,, \tag{6.14}$$

which is written in terms of the field strength

$$F_{\mu\nu} = -\frac{i}{e}[D_\mu, D_\nu] \equiv \partial_\mu A_\nu - \partial_\nu A_\mu\,. \tag{6.15}$$

The photon field kinetic term (6.14) ensures gauge and Lorentz invariance and leads to the correct formulation of Maxwell's equations of electrodynamics. Since gauge invariance does not allow for a mass term of the kind $\frac{1}{2}m^2 A_\mu A^\mu$ to be added, the photon is massless.

Thus the complete Lagrangian density of QED is

$$\mathcal{L}_{QED} = \bar{\psi}(i\gamma^\mu\partial_\mu - m)\psi + e\bar{\psi}\gamma^\mu A_\mu\psi - \frac{1}{4}F_{\mu\nu}F^{\mu\nu}\,. \tag{6.16}$$

6.2 Quantum Chromodynamics

Quantum chromodynamics (QCD) is the gauge theory of the strong interaction between quarks and gluons. The formalism of QCD is similar to that of QED with the extra colour charge. Unlike photons in QED, gluons themselves carry colour charge; therefore, as we will see, they can interact with each other.

The gauge group of QCD is the $SU(3)$ group of colour, consisting of unitary 3×3 matrices U with determinant equal to 1. A quark colour field q transforms under $SU(3)$ as

$$q(x) \to Uq(x) \equiv e^{i\alpha_a(x)T_a}q(x)\,, \tag{6.17}$$

where α_a are the group parameters, and T_a are its generators. The generators are a set of eight traceless hermitian linearly independent 3×3 matrices. They

do not commute:

$$[T_a, T_b] = i f_{abc} T_c \,, \tag{6.18}$$

where f_{abc} are the totally antisymmetric structure constants of the group. The group $SU(3)$ is therefore non-Abelian.

In analogy to QED, the theory starts from a free Lagrangian of the quark fields

$$\mathcal{L} = \bar{q}_j (i\gamma^\mu \partial_\mu - m) q_j \,, \tag{6.19}$$

where $j = 1, 2, 3$ are the colour indices. Imposing $SU(3)$ gauge invariance leads to a redefinition of the covariant derivative,

$$\partial_\mu \to D_\mu \equiv \partial_\mu + i g_s T_a G^a_\mu \,. \tag{6.20}$$

Here g_s is the strong coupling, and G^a_μ are the eight gluon gauge fields, giving rise to a quark-gluon interaction term. With the addition of a gluon kinetic term, the Lagrangian of quantum chromodynamics becomes

$$\mathcal{L}_{QCD} = \bar{q}(i\gamma^\mu \partial_\mu - m) q - g_s (\bar{q} \gamma^\mu T_a q) G^a_\mu - \frac{1}{4} G^a_{\mu\nu} G^{\mu\nu}_a \,. \tag{6.21}$$

Due to the non-Abelian properties of the theory, the field strength

$$G^a_{\mu\nu} = -\frac{i}{g_s} [D_\mu, D_\nu] \equiv \partial_\mu G^a_\nu - \partial_\nu G^a_\mu - g_s f_{abc} G^b_\mu G^c_\nu \tag{6.22}$$

has an extra term corresponding to gluon self-interactions, which causes three-gluon and four-gluon vertices to exist in QCD.

Another consequence of the non-Abelian nature of QCD is the running of the coupling constant and asymptotic freedom. When probing hadrons at very high energy, or small distance, the coupling constant $\alpha_s = g_s^2/4\pi$ is small, and the constituent quarks and gluons behave like free particles. As the energy scale of the interaction decreases, the coupling α_s increases, resulting in quark confinement within hadrons.

The running of α_s with the energy scale Q is given by

$$\alpha_s(Q^2) = \frac{12\pi}{(33 - 2n_f)\ln(Q^2/\Lambda^2_{QCD})}\,, \tag{6.23}$$

where n_f is the number of quark flavours, and Λ_{QCD} is a scale of the order of a hadronic mass (a few hundred MeV) at which α_s diverges. For high energies $Q \gg \Lambda_{QCD}$, the strong coupling α_s is small and QCD calculations are done using perturbation theory.

6.3 Hadronic Interactions

Perturbative QCD cannot be applied to describe the low energy structure of quarks and gluons inside a hadron, due to the divergence of α_s at these scales. The distributions of partons (quarks and gluons) within the proton are determined experimentally by studying deep inelastic scattering in proton-electron collisions at HERA [34, 35]. The measured parton distribution functions (PDF) $f_i(x_i, Q^2)$ express the probability of finding a parton i with a fractional momentum x_i when probing the proton at a scale Q. Once PDFs are measured at a given scale, they can be determined at other energies with evolution equations, similar to those describing the running of α_s.

In proton-proton collisions a high energy interaction occurs between two partons, called the hard scatter [32]. The cross-section σ of the scattering process then factorises into the hard scatter cross-section $\hat{\sigma}$, and the parton PDFs:

$$\sigma(pp \to X) = \sum_{i,j} \int dx_1 dx_2 f_i(x_1, \mu) f_j(x_2, \mu) \times \hat{\sigma}(ij \to X)\,. \tag{6.24}$$

Here μ is the chosen scale at which factorisation occurs: above that scale the hard process is calculated using perturbative QCD, and below μ the parton content of protons is given by PDFs. Physical observables do not depend on the factorisation

scale, as any μ dependence cancels if the calculations are performed to all orders of perturbation theory.

Once the hard scatter partons have been removed from the protons, the remaining proton constituents are no longer colour-neutral. In order to form colourless states, they regroup whilst generating further quarks, antiquarks and gluons, and combining into jets of hadrons. This process is known as hadronisation. Although it cannot be calculated using perturbative techniques, hadronisation is successfully described by models [32].

6.4 The Electroweak Model

The electroweak gauge theory unifies the weak interactions, mediated by massive $W^{\pm}$ and Z bosons, with the electromagnetic interactions. It is symmetric under weak isospin $SU_L(2)$ and hypercharge $U_Y(1)$ transformations. Fermions in the $SU(2)\times U(1)$ theory form weak isospin left-handed doublets χ_L and right-handed singlets χ_R:

$$\begin{aligned} \chi_L &= \begin{pmatrix} \nu_e \\ e^- \end{pmatrix}_L \text{ or } \begin{pmatrix} u \\ d \end{pmatrix}_L , \\ \chi_R &= e_R^- , \quad u_R \text{ or } d_R . \end{aligned} \tag{6.25}$$

Left-handed and right-handed states $\psi_{L,R}$ are defined using the projection operators $P_{L,R}$:

$$\psi_{L,R} = P_{L,R}\,\psi\,, \qquad P_L = \frac{1}{2}(1-\gamma^5)\,, \qquad P_R = \frac{1}{2}(1+\gamma^5)\,, \tag{6.26}$$

where $\gamma^5 = i\gamma^0\gamma^1\gamma^2\gamma^3$. For neutrinos, which are massless in the Standard Model, this means that $P_{L,R}$ are helicity operators; therefore, neutrinos only have left-handed states.

Weak isospin $\vec{T}$ and hypercharge Y are the generators of the $SU_L(2)$ and

$U_Y(1)$ groups, respectively, with couplings g and g'. The electromagnetic interaction is contained in the $SU(2) \times U(1)$ theory, with the electric charge being $Q = T^3 + Y/2$. The standard choice for $SU_L(2)$ generators are the Pauli matrices σ_i (6.5).

The two gauge symmetries lead to the introduction of weak gauge bosons W_μ^i $(i = 1, 2, 3)$ from $SU_L(2)$ and B_μ from $U_Y(1)$. The physical neutral gauge bosons A_μ and Z_μ are orthogonal combinations of B_μ and W_μ^3:

$$\begin{aligned} Z_\mu &\equiv \cos\theta_W W_\mu^3 - \sin\theta_W B_\mu \,, \\ A_\mu &\equiv \sin\theta_W W_\mu^3 + \cos\theta_W B_\mu \,, \end{aligned} \tag{6.27}$$

where θ_W is the weak mixing angle which relates the weak and electromagnetic couplings

$$g \sin\theta_W = g' \cos\theta_W = e \,. \tag{6.28}$$

The physical charged weak bosons are

$$W_\mu^\pm \equiv \frac{1}{\sqrt{2}}(W_\mu^1 \pm i W_\mu^2) \,. \tag{6.29}$$

The electroweak $SU(2) \times U(1)$ gauge invariant Lagrangian for leptons is

$$\mathcal{L}_{EW} = i\bar{\chi}_L \gamma^\mu (\partial_\mu - \frac{g}{2}\sigma_a W_\mu^a - \frac{g'}{2} B_\mu)\chi_L + \bar{e}_R \gamma^\mu (i\partial_\mu + g' B_\mu) e_R - \frac{1}{4} W_{\mu\nu}^a W_a^{\mu\nu} - \frac{1}{4} B_{\mu\nu}^a B_a^{\mu\nu} \,, \tag{6.30}$$

where the field strength tensors in the gauge boson kinetic terms are defined similarly to QED and QCD:

$$\begin{aligned} W_{\mu\nu}^a = & \quad -\tfrac{1}{g}[D_\mu, D_\nu] \quad \equiv \partial_\mu W_\nu^a - \partial_\nu W_\mu^a - g\varepsilon_{abc} W_\mu^b W_\nu^c \,, \\ B_{\mu\nu}^a = & \quad -\tfrac{1}{g'}[D_\mu, D_\nu] \quad \equiv \partial_\mu B_\nu^a - \partial_\nu B_\mu^a \,. \end{aligned} \tag{6.31}$$

The interaction terms of the Lagrangian can be rewritten to describe lepton interactions with the physical gauge bosons A_μ, $W_\mu^\pm$ and Z_μ:

$$g \sin\theta_W \bar{e} \gamma^\mu e A_\mu \,,$$

$$
\begin{aligned}
&-\tfrac{g}{2\sqrt{2}}\bar{\nu}\gamma^{\mu}(1-\gamma^{5})eW_{\mu}^{-}+\text{h.c.}\,,\\
&-\tfrac{g}{4\cos\theta_{W}}\bar{\nu}\gamma^{\mu}(1-\gamma^{5})\nu Z_{\mu}\,,\\
&\tfrac{g}{4\cos\theta_{W}}\bar{e}(\gamma^{\mu}(1-\gamma^{5})-4\sin^{2}\theta_{W}\gamma^{\mu})eZ_{\mu}\,,
\end{aligned}
\tag{6.32}
$$

where the hermitian conjugate, h.c., relates to the interaction with a W_{μ}^{+} boson.

The Lagrangian in Eq. (6.30) describes massless fermions and bosons. It is not possible to add to it a fermion mass term $-m\bar{\chi}\chi$, since left-handed fermions χ_L are isospin doublets and right-handed χ_R are singlets; thus, a term with $\chi_L\chi_R$ breaks gauge invariance. Adding mass terms for gauge bosons would break gauge invariance, too, and would make the theory non-renormalisable. That is why in the Standard Model fermions, W and Z bosons acquire masses by a spontaneous breaking of the $SU_L(2)\times U_Y(1)$ gauge symmetry.

6.5 The Higgs Mechanism for Electroweak Symmetry Breaking

The mechanism of spontaneous symmetry breaking introduces a ground state which breaks the symmetry of a system, while the Lagrangian retains its invariance under the symmetry group. The symmetry is then said to be hidden, as the vacuum state is not invariant under it.

In order to spontaneously break local $SU_L(2)\times U_Y(1)$ gauge symmetry, a complex scalar $SU(2)$ doublet field ϕ is introduced,

$$
\phi=\frac{1}{\sqrt{2}}\begin{pmatrix}\phi_1+i\phi_2\\ \phi_3+i\phi_4\end{pmatrix}. \tag{6.33}
$$

The $SU_L(2)\times U_Y(1)$ invariant Lagrangian density of ϕ is given as

$$
\mathcal{L}=(iD_{\mu}\phi)^{\dagger}(iD^{\mu}\phi)-\mu^{2}\phi^{\dagger}\phi-\lambda(\phi^{\dagger}\phi)^{2}-\frac{1}{4}W_{\mu\nu}^{a}W_{a}^{\mu\nu}-\frac{1}{4}B_{\mu\nu}^{a}B_{a}^{\mu\nu}\,, \tag{6.34}
$$

where $D_\mu \equiv \partial_\mu + ig\frac{\sigma_a}{2}W_\mu^a + ig'\frac{1}{2}B_\mu$ is the covariant derivative from (6.30).

The second and third terms in the Lagrangian represent the potential $V(\phi)$ which must be bounded from below; therefore, λ is always positive. For a positive μ^2 (mass term for ϕ), the solution for the vacuum state of the potential is $\phi_0 = 0$. However, taking μ^2 negative allows for a non-zero ground state to exist where

$$\phi_0^\dagger \phi_0 = \frac{1}{2}(\phi_1^2 + \phi_2^2 + \phi_3^2 + \phi_4^2) = -\frac{\mu^2}{2\lambda}\,. \tag{6.35}$$

In this case the potential has the "Mexican hat" shape shown in Fig. 6.1 and the minimum no longer lies at zero, but there is a set of minima (shown by the lower dotted line ring in the picture). In order to expand $\phi(x)$ around the minimum in perturbation theory, a particular value is chosen from the set of minima, thus breaking the gauge symmetry:

$$\phi_0 = \frac{1}{\sqrt{2}}\begin{pmatrix}0\\ v\end{pmatrix}, \qquad v \equiv \sqrt{-\frac{\mu^2}{2\lambda}}\,. \tag{6.36}$$

The expansion of the field around the vacuum then becomes

$$\phi(x) = \frac{1}{\sqrt{2}}\begin{pmatrix}0\\ v + h(x)\end{pmatrix}, \tag{6.37}$$

where the perturbation is the scalar field $h(x)$, called the Higgs field.

Substituting the vacuum expectation value (vev) ϕ_0 of the scalar field in the Lagrangian (6.34) leads to mass terms for the gauge bosons:

$$\left|\left(-ig\frac{\sigma_a}{2}W_\mu^a - i\frac{g'}{2}B_\mu\right)\phi\right|^2 = \left(\frac{1}{2}vg\right)^2 W_\mu^+ W^{-\mu} + \left(\frac{1}{2}v\sqrt{g^2+g'^2}\right)^2 Z_\mu Z^\mu + 0\, A_\mu A^\mu\,. \tag{6.38}$$

The masses of the $W_\mu^\pm$ and Z_μ bosons are proportional to the Higgs vacuum expectation value v,

$$M_W = \frac{1}{2}vg\,, \qquad M_Z = \frac{1}{2}v\sqrt{g^2+g'^2} \equiv \frac{M_W}{\cos\theta_W}\,, \tag{6.39}$$

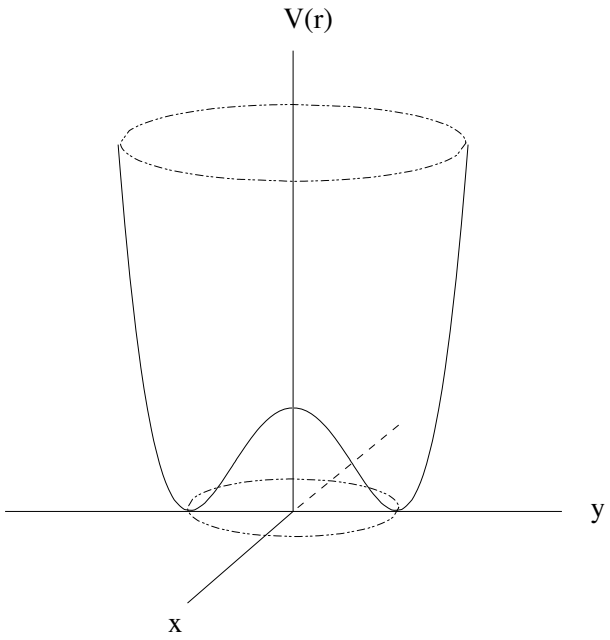

Figure 6.1: The spontaneous symmetry breaking Higgs potential [33].

while the photon A_μ remains massless, due to the neutral choice of a vacuum state ϕ_0, which is invariant under the QED gauge group $U_{em}(1)$. From the experimentally measured gauge boson masses and weak couplings, the value of the vev is $v = 246$ GeV. The local $SU_L(2) \times U_Y(1)$ gauge symmetry is spontaneously broken to $U_{em}(1)$ by the non-zero vev of the Higgs field.

The same scalar Higgs doublet generates masses for quarks and leptons, too. For example, for leptons the following gauge invariant Yukawa interaction term is added to the Lagrangian:

$$\mathcal{L}_{\text{Yukawa}} = -G_e \bar{\chi}_L \phi e_R + \text{h.c.}\,, \tag{6.40}$$

which, when substituting the choice of Higgs field (6.37), turns out to give mass terms for electrons,

$$\mathcal{L}_{\text{Yukawa}} = -\frac{G_e}{\sqrt{2}} v(\bar{e}_L e_R + \bar{e}_R e_L) - \frac{G_e}{\sqrt{2}}(\bar{e}_L e_R + \bar{e}_R e_L)h\,. \tag{6.41}$$

Neutrinos are left massless in the Standard Model. In this Lagrangian, the

Yukawa coupling G_e is a free parameter which can be chosen so that it gives the correct electron mass $m_e = G_e v/\sqrt{2}$. The second term of (6.41) contains the Higgs-fermion interaction with coupling proportional to the fermion mass.

For quarks the situation is slightly different, as both up and down type quarks have masses. The quark Yukawa interaction terms lead to mass mixing, which means that quark mass eigenstates differ from their weak eigenstates. Denoting the down quark weak eigenstates as (d', s', b'), the mixing is parametrised by a 3×3 unitary matrix as

$$\begin{pmatrix} d' \\ s' \\ b' \end{pmatrix} = V_{CKM} \begin{pmatrix} d \\ s \\ b \end{pmatrix} . \tag{6.42}$$

The matrix V_{CKM} is the Cabibbo-Kobayashi-Maskawa (CKM) matrix with four independent parameters. Then for up type quarks q_i (of flavour $i = u, c, t$) and down type quarks q_j ($j = d, s, b$), the coupling to W bosons is modified with the corresponding CKM mixing matrix element V_{ij},

$$-\frac{g}{2\sqrt{2}} V_{ij} \bar{q_i} \gamma^\mu (1 - \gamma^5) q_j W_\mu^- + \text{h.c.} \tag{6.43}$$

The Higgs scalar particle acquires mass from electroweak symmetry breaking, too. The Higgs potential

$$V(\phi) = \mu^2 \phi^\dagger \phi + \lambda (\phi^\dagger \phi)^2 \tag{6.44}$$

leads to a mass term for the Higgs boson with $m_H = \sqrt{2\lambda} v$. Although v is known, λ is arbitrary and therefore the Higgs mass is not predicted by the model. The theoretical upper limit on the Higgs mass from the validity range of perturbation theory and loop corrections to scattering processes is $m_H < 1$ TeV. Direct Higgs searches at particle experiments [37] have given a lower mass bound of $m_H > 114.4$ GeV at 95% confidence level.

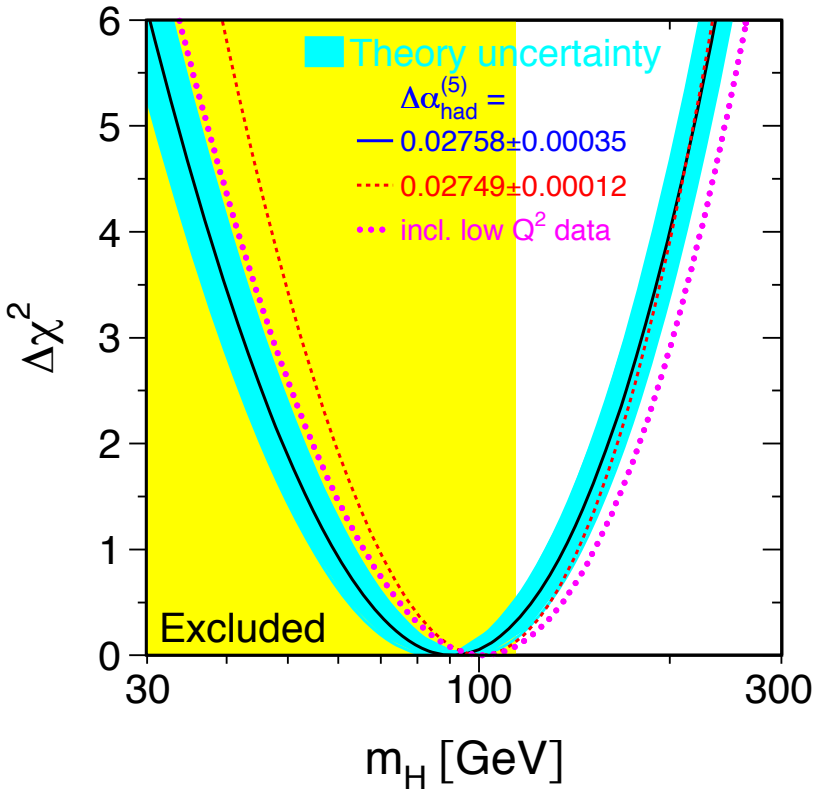

Figure 6.2: Delta chi squared curve of the Standard Model fit to the Higgs mass, derived from various electroweak measurements [36]. The vertical band shows the 95% confidence level exclusion limit from direct Higgs searches.

The Higgs boson has not been observed yet; however, some constraints were made on its mass from measuring Standard Model observables. The Higgs mass appears in radiative corrections to the vector boson and top quark masses. Precision measurements of electroweak observables such as $\sin\theta_W$, m_{top}, M_Z, α_s and α give an overconstrained system and limits on m_H can be extracted. The Standard Model favours a relatively light Higgs, with a limit from the latest fit to all electroweak data of $m_H < 219$ GeV at 95% confidence level (when including the direct search lower mass limit in the fit) [36].

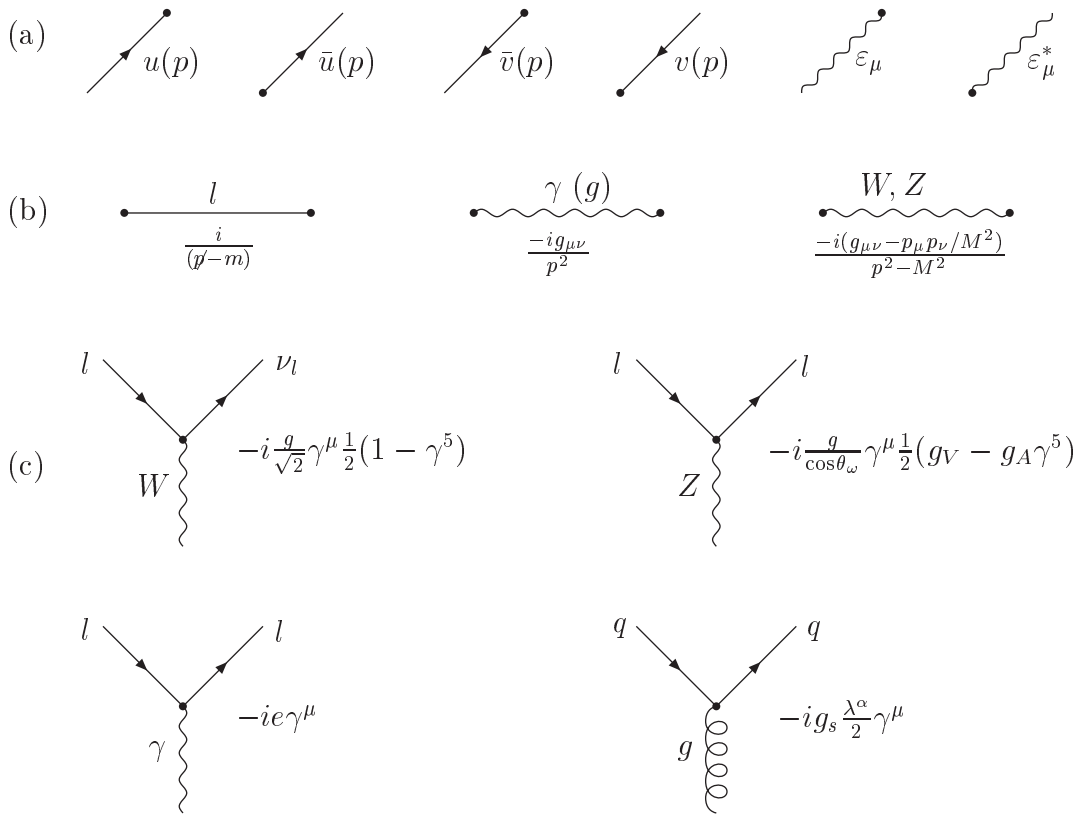

Figure 6.3: Some of the basic Feynman diagrams and their corresponding rules for (a) incoming and outgoing particles, (b) particle propagators and (c) interaction vertices.

6.6 Feynman Diagrams and Rules

Processes involving particle interactions can be represented as Feynman diagrams. This allows the calculation of process cross-sections using Feynman rules derived from the Lagrangian density of the theory. Each internal particle line corresponds to a particle propagator factor, and each vertex carries a vertex factor formed from the interaction term of the Lagrangian. In addition, incoming and outgoing particle lines correspond to energy-momentum conservation constraints.

A particle scattering process usually has contributions from several Feynman diagrams. For each diagram the propagator and vertex factors are multiplied in a

certain order to give the amplitude. Then the amplitude factors from all possible diagrams contributing to the same process are added to get the total amplitude of the process. Taking the square of the amplitude, or matrix element, and integrating over the appropriate phase-space results in the cross-section of the process.

Fig. 6.3 shows some basic Feynman diagrams and their corresponding Feynman rules in momentum space. Time flows from left to right, and the arrows correspond to the direction of the fermion line, pointing right for a particle and left for an antiparticle. Incoming and outgoing fermions and anti-fermions are represented by spinors (u, $\bar{u}$, v, and $\bar{v}$). The rules for incoming and outgoing vector bosons require their polarisation vectors ε_μ and ε^*_μ, respectively. The internal particle line propagators are written in terms of particle momenta and masses (μ and ν are Lorentz indices for vector bosons). Interactions are represented by vertices, the rules for which follow from the strong (6.21) and electroweak (6.32) Lagrangian interaction terms.

The Standard Model Feynman diagrams introduced here are used in Chapters 7 and 8 to represent the scattering processes under study.

Chapter 7

Central Exclusive Higgs Production

The process of central exclusive Higgs production at the LHC is characterised by non-disintegrating inelastically scattered protons. The Higgs boson is produced via gluon-gluon fusion, and the initial protons exchange an additional gluon that balances the colour flow, leaving them intact. A diagram of exclusive Higgs production is shown in Fig. 7.1.

Several models exist for calculating the exclusive process cross-section [38, 39]. In this analysis the perturbative "Durham model" of Khoze, Martin and Ryskin [40, 41, 42] was used. A short introduction to diffractive scattering and rapidity gaps is given in Section 7.1. After defining in Section 7.2 the kinematic variables used throughout the calculations, the Durham model cross-section for exclusive Higgs production is given in Section 7.3. The advantages of the exclusive channel are outlined in Section 7.4, and the Higgs to WW decay mode is characterised in Section 7.5.

7.1 Central Exclusive Diffractive Production

The process in Fig. 7.1 is a t-channel colour singlet exchange, which does not destroy the protons. The protons stay intact and scatter through small angles, having lost small fractions of their momenta. The momentum losses are spent in producing a central system, which is kinematically well separated from the forward protons. The process is referred to as diffractive, because the mass of the produced system is much smaller than the collision energy [38]. This is known as the Regge limit, $s \gg M^2$.

In diffractive processes, there is a lack of hadronic activity in the detector forward regions, close to the outgoing protons. This signature is called a rapidity gap. The rapidity y of a particle with non-zero transverse momentum is defined in terms of its longitudinal momentum p_L (in this case the longitudinal momentum is along the beam direction, $p_L \equiv p_z$) and energy E as [43]

$$y = \frac{1}{2} \ln \frac{E + p_L}{E - p_L}. \tag{7.1}$$

In the massless particle limit, rapidity and pseudorapidity are the same.

Although rapidity gaps offer a clean signature for exclusive signals, it will be spoiled by overlap interactions (known as pile-up) at high LHC luminosities. At the low luminosity of $10^{33}\,\mathrm{cm}^{-2}\mathrm{s}^{-1}$, there will be on average ~ 2.3 interactions per bunch crossing. This number increases to 22 pile-up interactions per crossing at high luminosity ($10^{34}\,\mathrm{cm}^{-2}\mathrm{s}^{-1}$). A rapidity gap trigger seems unfeasible due to the pile-up effect.

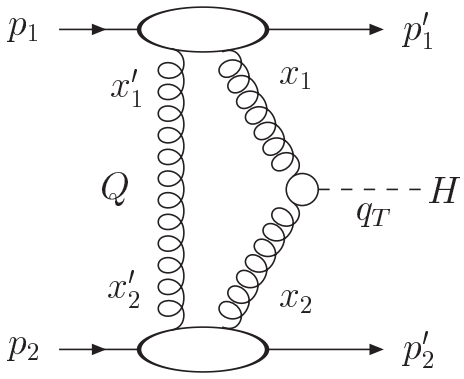

Figure 7.1: The process of central exclusive Higgs production.

7.2 Kinematic Variables

The gluons that fuse to produce the Higgs boson carry small fractions of the proton momentum. In Fig. 7.1 these are the fractional longitudinal momentum losses x_1 and x_2, defined as

$$x_1 = 1 - \frac{p_1'^z}{p_1^z}\,, \qquad x_2 = 1 - \frac{p_2'^z}{p_2^z}\,, \tag{7.2}$$

where $p_{1,2}^z$ and $p_{1,2}'^z$ are the longitudinal components along the beam direction of proton momenta before and after the collision. The longitudinal momentum fractions with respect to each proton of the "screening" gluon, which is exchanged to balance the colour flow between the protons, are x_1' and x_2'. The gluon momentum fractions satisfy the relations [44]

$$\left(x' \sim \frac{Q_t}{\sqrt{s}}\right) \ll \left(x \sim \frac{M_H}{\sqrt{s}}\right) \ll 1\,, \tag{7.3}$$

where $\sqrt{s}$ is the collision energy (14 TeV in the case of LHC), and Q_t is the transverse momentum of the screening gluon. Although the values of Q_t are small, they are still in the perturbative QCD regime [44]:

$$\Lambda_{QCD}^2 \ll Q_t^2 \ll M_H^2\,. \tag{7.4}$$

The rapidity of the Higgs can be expressed in terms of x_1 and x_2:

$$y = \frac{1}{2} \ln \frac{x_1}{x_2} \,. \tag{7.5}$$

The protons momentum transfer variables $t_{1,2}$ are given by

$$t_1 = (p_1' - p_1)^2 \,, \qquad t_2 = (p_2' - p_2)^2 \,, \tag{7.6}$$

and they also equal the transverse momenta squared of the outgoing protons.

The centre-of-mass energy squared of the fusing gluons is denoted as $\hat{s}$,

$$\hat{s} = (p_1 + p_2 - p_1' - p_2')^2 \,. \tag{7.7}$$

The diffractive regime occurs when $-t \ll \hat{s} \ll s$. Thus in the diffractive limit the transverse momenta of the outgoing protons can be neglected, $p_{T1,2}' \to 0$. The incoming and outgoing protons can also be considered massless ($m_p \ll E, E'$), so the fractional momentum losses $x_{1,2}$ reduce to fractional energy losses:

$$x_{1,2} \approx 1 - \frac{E_{1,2}'}{E} \,. \tag{7.8}$$

In order to produce a central system of mass 100–200 GeV, the protons lose around 2% or less of their momenta. This is within the experimental acceptance of FP420, which can therefore detect outgoing protons from the exclusive production of a relatively light Higgs ($M_H \leq 200$ GeV).

7.3 The Durham Model of Exclusive Higgs Production

The Durham model of Khoze, Martin and Ryskin [40, 41, 42, 44] uses perturbative QCD to calculate the cross-section for exclusive Higgs production in proton collisions, $pp \to p + H + p$ (where the + signs denote rapidity gaps). The Higgs

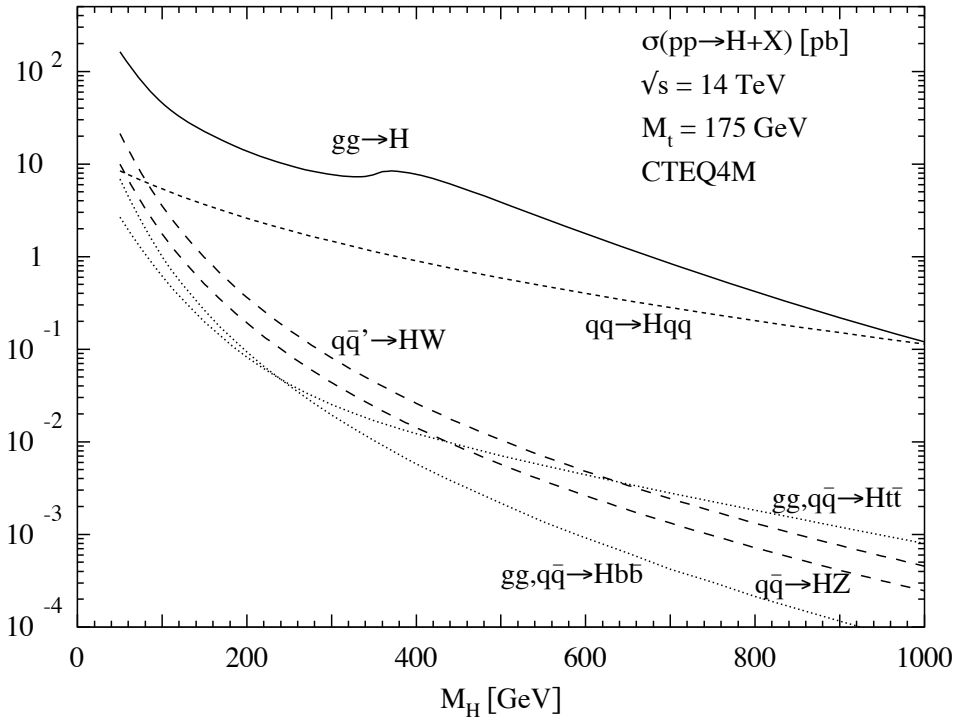

Figure 7.2: Cross-sections for Standard Model Higgs production as a function of Higgs mass at the LHC for the various production mechanisms [45].

boson is produced by gluon-gluon fusion through a virtual top quark loop. This is the dominant Higgs production mechanism at the LHC, as can be seen in Fig. 7.2.

The amplitude of the process in Fig 7.1 is [41, 42]

$$\mathcal{M} = A\pi^3 \int \frac{dQ_t^2}{Q_t^4} \, f_g\left(x_1, x_1', Q_t^2, \frac{M_H^2}{4}\right) f_g\left(x_2, x_2', Q_t^2, \frac{M_H^2}{4}\right) . \tag{7.9}$$

Here A gives the contribution of the $gg \to H$ vertex:

$$A^2 = K\frac{\sqrt{2}G_F}{9\pi^2}\alpha_s^2(M_H^2)\,, \tag{7.10}$$

in which $K \approx 1.5$ is a factor to account for next-to-leading order corrections (NLO K factor), G_F is the Fermi weak coupling constant

$$G_F = \frac{\sqrt{2}g^2}{8M_W^2}\,, \tag{7.11}$$

and the strong coupling constant α_s is evaluated at the scale of the process, the Higgs mass M_H.

The integral in the amplitude (7.9) runs over the screening gluon transverse momentum, Q_t. The functions f_g are the unintegrated skewed (off-diagonal) gluon densities. They depend on the gluon momentum fractions $x_{1,2}$, $x'_{1,2}$, the transverse momentum Q_t and the hard scale $\mu = M_H/2$. The f_g are taken off-diagonal because the screening gluon carries a much smaller momentum fraction than the fusing gluon, see Eq. (7.3). For $x' \ll x$ the unintegrated skewed gluon density can be approximated by an expression involving the integrated gluon density $g(x, Q_t^2)$ [41]:

$$f_g\left(x, x', Q_t^2, \mu^2\right) = R_g \frac{\partial}{\partial \ln Q_t^2}\left[\sqrt{T(Q_t,\mu)}\, x g(x, Q_t^2)\right] , \tag{7.12}$$

where the multiplicative factor R_g contains the skewed effect. At the LHC energy it was found [42] that $R_g = 1.2$.

The factor $T(Q_t, \mu)$, known as the Sudakov factor, accounts for the probability of the hard gluon not to emit QCD radiation in the evolution up to the hard scale $\mu = M_H/2$. The Sudakov factor is calculated using perturbative QCD evolution equations. The unintegrated skewed gluon density (7.12) contains a square root of T, because it is assumed that only the hard gluon can radiate. The screening gluon has very little momentum, $x' \approx 0$, and thus no ability to emit radiation.

The integral (7.9) is infrared-divergent due to the factor $1/Q_t^4$. However, this divergency is regulated by the Sudakov factor, which falls exponentially as $Q_t \to 0$ [38]:

$$T \sim \exp\left(-\frac{C_A \alpha_s}{\pi} \int_{Q_t^2}^{M_H^2/4} \frac{dp_T^2}{p_T^2} \int_{p_T}^{M_H/2} \frac{dE}{E}\right) . \tag{7.13}$$

The exponent falls faster than the fourth power of Q_t, thus keeping the integral finite. Another way to explain this effect is in terms of colour screening: the screening gluon forbids emission with $p_T < Q_t$ off the fusing gluons as it screens the colour charge, which cannot be resolved by long-wavelength radiation

($\lambda \approx 1/p_T$). In the infrared limit, $Q_t \to 0$, the screening gluon can no longer screen colour charge, and fails to suppress real emissions. Then the non-emission probability vanishes.

In addition to Sudakov rapidity gap survival, the exclusive process cross-section must also account for suppressing soft parton rescattering effects. The probability that the gaps and the protons survive the soft rescattering of partons from the underlying event is denoted by S^2. Although it cannot be calculated using perturbative techniques, S^2 has been modelled and evaluated in [46, 47]. The gap survival probability model is based on an analysis of all available data from experimental measurements of soft diffraction processes. There it was shown that S^2 depends on the parton momentum fractions, as well as the hard subprocess of the reaction, and it is not a universal factor. For LHC energies, the gap survival factor for the $pp \to p + H + p$ process was found to be $S^2 = 0.02$ with an accuracy of $\pm 50\%$ [44].

Currently S^2 brings a large uncertainty factor to the exclusive cross-section. The other contributions to the cross-section uncertainty come from the uncertainties of the gluon densities ($\pm 5\%$), NLO contributions to the Sudakov T factor ($\pm 20\%$), and NNLO corrections to the Higgs-gluon vertex ($\pm 20\%$). The NNLO correction uncertainty is not unique to exclusive production as it applies to all processes involving a Higgs-gluon vertex.

The Durham model prediction for the total exclusive cross-section at the LHC is $\sigma = 3$ fb for a Higgs of mass $M_H = 120$ GeV, with a factor of 2 uncertainty [44]. It was suggested [44, 48] that the uncertainty could be improved by measuring exclusive processes with higher rates, for example the exclusive production of high-E_T dijets or diphotons. This is possible due to the fact that all cross-section terms, apart from the vertex factor, are common for exclusive dijet,

diphoton and Higgs production.

For exclusive diffractive production of a central system, the cross-section σ factorises into [42]

$$\sigma = \mathcal{L}(M^2, y) \times \hat{\sigma}(M^2)\,, \tag{7.14}$$

where $\mathcal{L}$ is the effective gluon-gluon luminosity for a central system of mass M and rapidity y, and $\hat{\sigma}$ is the hard subprocess cross-section. The luminosity is the same for all colourless t-channel exchange states. It can be written as a product of the gap survival factor S^2 and a perturbative part L:

$$M^2 \frac{\partial \mathcal{L}}{\partial y \partial M^2} = S^2 L\,, \tag{7.15}$$

where L is given by

$$L = \left(\frac{\pi}{8b} \int \frac{d^2 Q_t}{Q_t^4}\, f_g(x_1, x_1', Q_t^2, \mu^2) f_g(x_2, x_2', Q_t^2, \mu^2) \right)^2 . \tag{7.16}$$

This expression is integrated over the transverse momenta of the outgoing protons. The factor b is the slope of the momentum transfer distribution of the protons,

$$\frac{d^2\sigma}{dt_1 dt_2} \propto e^{b(t_1+t_2)}\,, \tag{7.17}$$

and in the cross-section calculation it takes the value $b = 4$ GeV^{-2} [9].

The factorisation of the cross-section (7.14) allows the calculation of different exclusive production processes, once the effective luminosities are known.

7.3.1 The ExHuME Event Generator

The Durham perturbative model of exclusive diffraction is implemented in the ExHuME [49] event generator. ExHuME uses the factorisation of the exclusive cross-section in Eq. (7.14) to calculate the differential effective luminosity and the hard subprocess cross-section. The hard subprocess amplitude is evaluated

by taking the colour-singlet, zero spin projection of the general gluon fusion amplitude. For the gluon-gluon effective luminosity, ExHuME uses a fixed gap survival factor of $S^2 = 0.03$ at LHC energy.

ExHuME generates exclusive Higgs production and is linked to the Higgs decay programme HDECAY [50], and to Pythia [51] for hadronisation of the decay products. It takes the integrated gluon densities from the parton distribution function library LHAPDF [52].

7.4 Advantages of the Exclusive Higgs Production Mode

Searching for the Standard Model Higgs boson in the exclusive process not only complements conventional LHC inclusive searches, but also offers some unique advantages [53]. If the two protons are detected by forward proton taggers and their momenta measured, the mass of the centrally produced system can be calculated as the missing mass MM [54],

$$MM^2 = (p_1 + p_2 - p_1' - p_2')^2 \approx x_1 x_2 s\,. \tag{7.18}$$

The exclusive production of a Higgs boson of mass M_H will give a mass peak in the missing mass spectrum at M_H. The Higgs mass found by the central ATLAS detector can be matched with the high-resolution missing mass measurement. The expected mass resolution of the proton taggers, which is independent of the decay mode of the central system, is shown in Fig, 7.3.

Observing the exclusive production process would reveal the quantum numbers of the produced Higgs particle [42, 53, 55]. In the massless proton limit ($m_p \ll E, E'$), the protons cannot change helicity in the exclusive process. Since

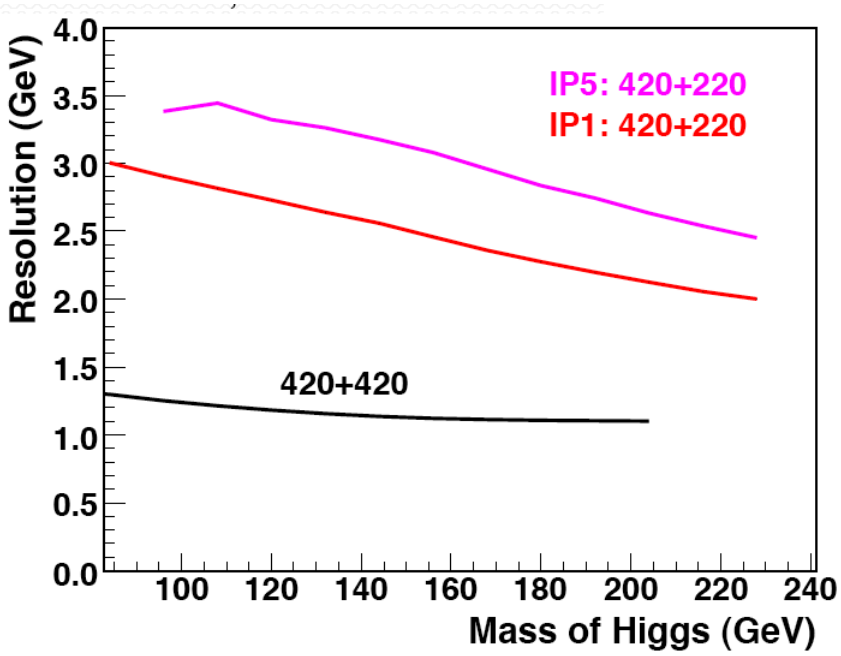

Figure 7.3: Higgs mass resolution of the proton taggers, in the cases when both protons are detected at 420 m (420+420), and when one proton is detected at 420 m with the other one at 215 m (420+220) [6]. The curve marked IP1 corresponds to the ATLAS interaction point 1, and IP5 gives the resolution at the CMS interaction point 5.

the transverse momenta of the recoil protons are very small, there is no angular momentum transferred to the central system. Hence in exclusive diffraction the produced system has predominantly the quantum numbers of the vacuum: no colour or charge, and zero projection of angular momentum in the beam direction, $J_z = 0$. Detecting the Higgs in the exclusive process would establish that it is a scalar, CP-even particle. This is important, since various extensions of the Standard Model predict the existence of several Higgs bosons with different quantum numbers (see, for example, [56]).

Another obvious advantage of exclusive production is the clean signature of the process—there are no soft particles from the underlying event. The only final states in the central detector are the Higgs decay products. The colour-singlet,

$J_z = 0$ selection rule greatly reduces backgrounds, making it possible to observe the Standard Model Higgs with signal-to-background ratios greater than one.

7.5 The Higgs to WW$^{(*)}$ Decay Channel

For a light Higgs the dominant decay mode is a pair of $b\bar{b}$ quarks, and it has been the subject of previous analyses [44, 57]. The Higgs can be detected in the $b\bar{b}$ decay channel, provided that the leading protons are tagged. An accurate missing mass measurement by the taggers would enable the missing mass peak (MM) to be matched with the $b\bar{b}$ mass measured by ATLAS ($M_{b\bar{b}}$). The main background, exclusive $b\bar{b}$ production, is suppressed at leading order by the $J_z = 0$ selection rule. However, the level of background depends crucially on the mass resolution of the taggers, because a wider Higgs mass peak will contain more background events from the $b\bar{b}$ continuum.

Under the optimistic assumption of a 1 GeV mass resolution of the taggers, it was found that the signal to background ratio is S/B ≈ 1 [44]. An additional challenge is to trigger on this channel: the two b jets usually have transverse momenta below the trigger jet thresholds, and signals from the taggers at 420 m cannot be included in the level 1 trigger.

Therefore the WW$^{(*)}$ decay mode becomes experimentally more attractive. The Higgs can decay to a pair of W bosons, one of which can be virtual, W*, if the Higgs mass is below the $2M_W$ threshold. Measurement of the W$^{(*)}$ boson decay to leptons would benefit from the relatively low p_T thresholds of ATLAS leptonic triggers, leading to high acceptances. Also, background elimination does not depend on the taggers' mass resolution.

The exclusive Higgs production cross-sections times branching ratios for the

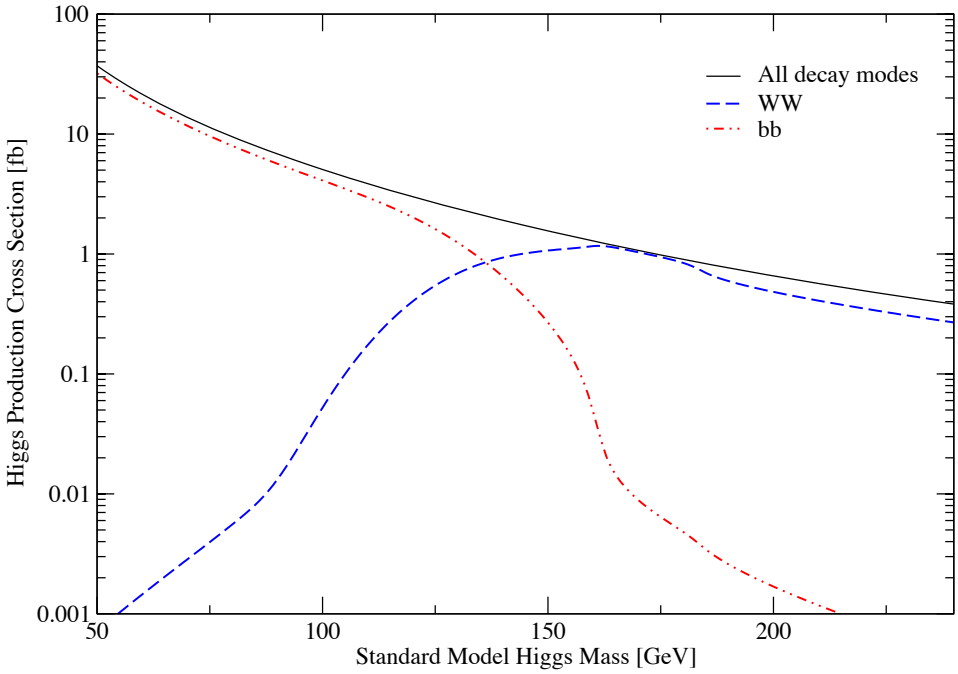

Figure 7.4: The exclusive cross-section times branching ratio for Standard Model Higgs production as a function of Higgs mass, for the $b\bar{b}$ (dashed-dotted line) and WW (dashed line) decay modes. The total cross-section is shown by the solid line.

$b\bar{b}$ and WW decay modes, obtained using ExHuME, are shown in Fig. 7.4. Although the total cross-section falls with increasing Higgs mass, this is balanced by the growing branching ratio of the WW decay mode. The analysis of exclusive Higgs production and decay to $WW^{(*)}$ in the semileptonic and fully-leptonic channels is presented in Chapter 8.

Chapter 8

Analysis of Exclusive Diffractive Higgs Production and Decay to $WW^{(*)}$

This chapter describes the simulation study of central exclusive Higgs production and decay to $WW^{(*)}$. The analysis of the Higgs signal was performed at particle level, with event selection based on the ATLAS triggers and the acceptances of the proton taggers. Initial estimates of the background rates are given.

The signal and backgrounds are characterised in Sections 8.1 and 8.2, respectively. Section 8.3 describes the event selection for semileptonic and fully leptonic WW decays. The results of this study, which have recently been published in [58], are given in Section 8.4.

8.1 Signal

The signal of the Standard Model Higgs boson decaying to WW can be classified into three types of events, depending on the decay modes of the W bosons: fully leptonic, semileptonic, and fully hadronic WW decays.

Fully leptonic decays, in which both W bosons decay by the $W^{\pm} \rightarrow l^{\pm}\nu_l$ process ($l = e, \mu$), offer the cleanest experimental signature: only two isolated leptons (e or μ) in the central detector, and missing transverse energy from the two neutrinos. Although fully leptonic WW decays with an electron or a muon are the most experimentally attractive, their branching ratio is low; they make up only 4.5% of all WW decays.

In semileptonic decays, one W decays to leptons while the other one decays to a quark-antiquark pair, which in turn hadronises to form two jets. A Feynman diagram of the Higgs production process with subsequent semileptonic WW decay is shown in Fig. 8.1. Semileptonic decays with a muon or an electron have a branching ratio of around 29%. Events with fully leptonic and semileptonic W decays were selected using the standard ATLAS leptonic triggers, which require a high-p_T isolated lepton (electron or muon) to be reconstructed in the central detector.

The case in which a W boson decays leptonically to a tau is more complicated because taus are not stable particles. A tau can decay to an electron and two neutrinos, a muon and two neutrinos, or a jet of hadrons and a neutrino. Event selection was based only on leptonic τ decays by demanding that the decay electron or muon passes ATLAS level 1 trigger thresholds. The process of one or both W bosons decaying to taus, with the taus decaying leptonically ($WW \rightarrow \tau\nu_\tau\tau\nu_\tau \rightarrow l\nu_l\nu_\tau l\nu_l\nu_\tau$ or $WW \rightarrow \tau\nu_\tau l\nu_l \rightarrow l\nu_l\nu_\tau l\nu_l$), has a small branching ratio of less than 2%. Such events have a clean fully leptonic signature, but

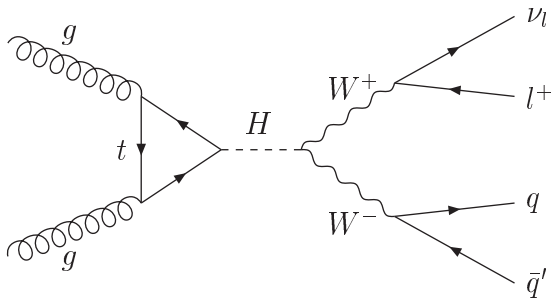

Figure 8.1: The hard subprocess of $gg \to H \to WW \to l\nu q\bar{q}$. The Higgs boson is produced via gluon-gluon fusion, and it decays to $WW^{(*)}$ with the W bosons decaying semileptonically.

their lepton p_T spectrum is softer due to the larger number of neutrinos, thus making trigger selection more difficult.

WW decays with semileptonic final states from tau decays (from the processes WW $\to \tau\nu_\tau qq \to l\nu_l\nu_\tau jj$, WW $\to l\nu_l\tau\nu_\tau \to l\nu_l j\nu_\tau$ or WW $\to \tau\nu_\tau\tau\nu_\tau \to l\nu_l\nu_\tau j\nu_\tau$) were also considered since they could pass ATLAS leptonic triggers. The contribution of these to the total signal is small, due to the branching ratio of 9%, combined with the low p_T of the leptons.

The final category of events is the fully hadronic WW decays, coming mostly from the WW $\to qqqq$ process, but also including hadronic decays of taus from the W bosons. These constitute more than half (56%) of all WW decays. Unfortunately the resulting four jets would not pass the ATLAS level 1 trigger selection: the trigger threshold for each of the four jets is $E_T > 55$ GeV [5], while the jets from WW decays share the available energy of the process, resulting in a maximum jet transverse energy of $E_T \approx M_H/4$. Therefore hadronic WW decays were not used in this analysis.

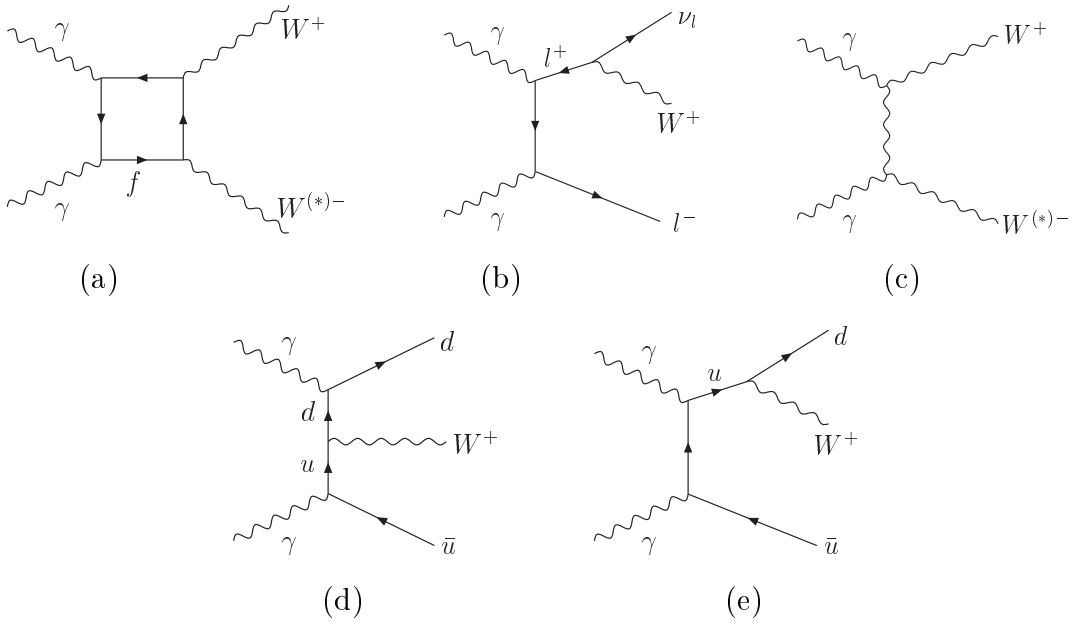

Figure 8.2: The hard subprocesses of photon-induced backgrounds.

8.2 Backgrounds

There are two categories of background processes to the Higgs to WW signal: photon-photon and gluon-gluon fusion backgrounds.

The photon-induced, or QED, backgrounds are shown in the Feynman diagrams of Fig. 8.2. The protons radiate photons which fuse to produce a $WW^{(*)}$ pair, a W with a lepton and a neutrino, or a W with a $q\bar{q}$ pair. The QED $Wq\bar{q}$ production process, shown in diagrams (d) and (e), can fake the semileptonic WW signal decay. The $\gamma\gamma \to WW^{(*)}$ process (in diagrams (a) and (c)) and the $\gamma\gamma \to Wl\nu_l$ process (in diagram (b)) form the background to both semileptonic and fully leptonic signal decays.

The two-photon backgrounds were evaluated in [58] by requiring the final states to be within $|\eta| < 2.5$, and integrating over a mass window $\Delta M \approx 3\sigma \sim 0.05 M_H$, corresponding to a Gaussian mass resolution of the proton taggers with

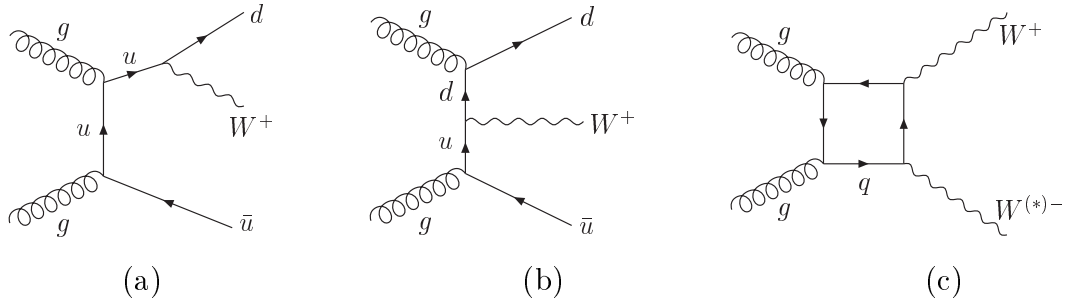

Figure 8.3: The hard subprocesses of gluon-induced backgrounds.

a width $\sigma = 2$ GeV. The calculated cross-sections are $\sigma^{\mathrm{QED}} = 0.015$ (0.033, 0.37, 2.0) fb for Higgs masses $M_H = 120$ (140, 160, 180) GeV. After imposing the single leptonic trigger cuts, described in Section 8.3.2, the QED cross-sections fall to $\sigma^{\mathrm{QED}} = 0.01$ (0.02, 0.27, 1.53) fb for $M_H = 120$ (140, 160, 180) GeV.

Although the QED backgrounds are small compared to the signal for $M_H < 150$ GeV, they grow with increasing Higgs mass. In this case they can be controlled by constraining the transverse momenta of the leading protons, since proton p_T distributions are much softer in photon fusion compared to gluon fusion processes. Demanding that the protons have $p_T > 100$ (200) MeV reduces the QED backgrounds by a factor of 15 (75) [58].

The second type of backgrounds come from the gluon-gluon processes in Fig. 8.3. The quark box diagram (c) was found from the results of [59] to have a negligible contribution of less than 1% of the signal [58]. The QCD W-strahlung processes of Fig. 8.3 (a) and (b) form the dominant background to semileptonic signal decays. They were evaluated in [60] by using the spinor techniques of [61], again over a mass interval $\Delta M \approx 3\sigma \sim 0.05 M_H$, and by requiring the quarks to fall within $|\eta| < 2.5$. The cross-sections for the exclusive W + 2 jets production background were found to exceed the signal, leading to $\sigma^{\mathrm{QCD}} = 1.7$ fb for $M_H = 140$ GeV.

The QCD background can be suppressed by placing a mass window constraint on the hadronic W, as the quark jets not originating from a W form a continuum under the signal peak. The mass window cut is effective for Higgs masses above the $2M_W$ threshold, when both W bosons are real. However, at $M_H < 160$ GeV this cut would eliminate also the signal: if the hadronically decaying W from the signal is virtual, its mass would fall outside the mass window.

The QED and QCD backgrounds are controllable, and for fully leptonic decays and semileptonic decays with a real hadronic W the expected signal-to-background ratios are greater than one.

8.3 Event Selection

The Higgs signal events were generated using ExHuME [49] interfaced to the Higgs decay tool HDECAY [50] and to the parton distribution function library LHAPDF [52]. Hadronisation was done using Pythia 6.25 [51].

Event selection was implemented at particle level (without detector simulation) by applying ATLAS triggers, acceptances of proton taggers and jet finding. The following sections describe the event selection in detail.

8.3.1 Acceptance of Proton Taggers

The event selection requires both outgoing protons to be detected by the proton taggers at 420 m or 215 m in order to identify the process as exclusive diffractive production. The acceptance of the proton taggers as a function of the mass of the central system was taken from [63] to be 61% (67%, 71%, 74%, 77%) for $M_H = 120$ (140, 160, 180, 200) GeV. The acceptance of the taggers grows with

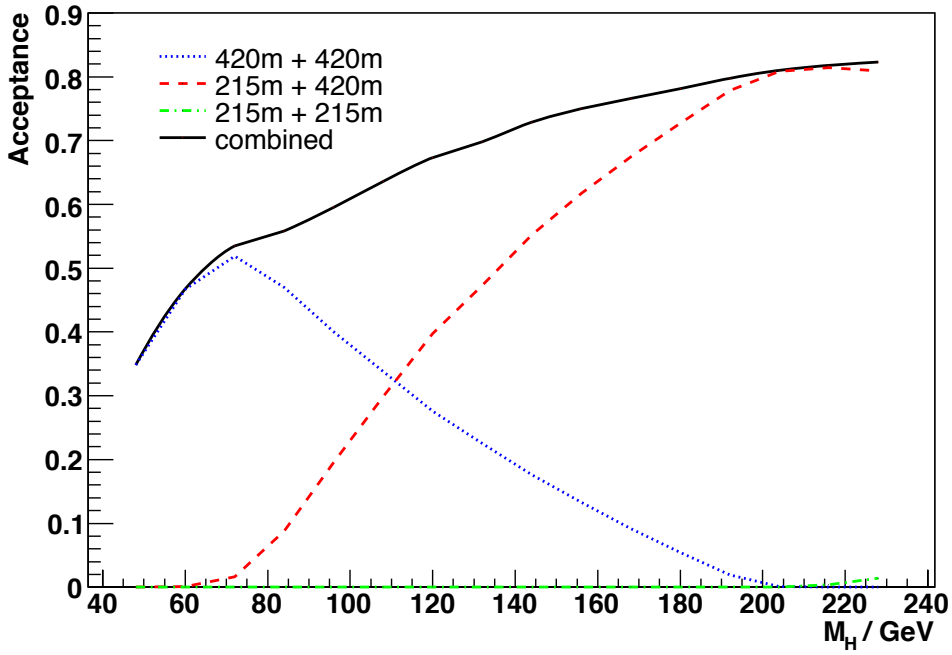

Figure 8.4: Acceptance of the proton taggers at different positions around the ATLAS interaction point as a function of Higgs mass [62]. The dotted curve corresponds to both protons being detected at 420 m, the dashed curve corresponds to one proton being detected at 215 m and the other one at 420 m, and the dash-dotted curve corresponds to both protons being detected at 215 m. The solid curve represents the combined acceptance of all tagger stations. The distance of approach of the taggers to the beam is 3 mm at 420 m, and 2 mm at 215 m.

increasing Higgs mass, making event selection more difficult for low masses. The numbers were obtained by performing a fast detector simulation for CMS, and tracking leading protons down the accelerator beam line. The software package MAD [64] with version 6.2 of LHC optics was used for simulating the taggers' response to the outgoing protons.

There has been more recent progress in the simulations of leading protons. The software package FPTRACK [62] was developed especially for simulating protons in FP420. There are some small discrepancies between the acceptances used in this analysis (from [63]) and the more recent results from FPTRACK,

shown in Fig. 8.4. At the time of writing these discrepancies are being investigated. The numbers used in this analysis correspond to the more pessimistic acceptances of the proton taggers.

8.3.2 Triggering

The main factor affecting the signal reconstruction efficiency is triggering. Events were selected using the standard ATLAS level 1 trigger criteria for leptons [5]. The level 1 single leptonic trigger requires either an electron with transverse momentum $p_T > 25$ GeV or a muon with $p_T > 20$ GeV to be reconstructed in the central detector with pseudorapidity in the range $|\eta| < 2.5$. This condition can select both fully leptonic and semileptonic WW decays.

Fully leptonic decays can in addition pass the level 1 dilepton triggers, which require two leptons to be measured within $|\eta| < 2.5$. There are three possible dilepton trigger menus used in the event selection:

- two electrons each with $p_T > 15$ GeV.
- two muons each with $p_T > 10$ GeV.
- an electron with $p_T > 15$ GeV and a muon with $p_T > 10$ GeV.

Fully leptonic decays benefit from the lower dilepton trigger thresholds, thus achieving better selection efficiencies.

The signal lepton η and p_T distributions are shown in Fig. 8.5 for $M_H = 120, 140, 160$ GeV and in Fig. 8.6 for $M_H = 180, 200$ GeV. For fully leptonic decays only the transverse momentum and pseudorapidity of the highest-p_T lepton are given. It can be seen that most leptons fall within the ATLAS pseudorapidity acceptance of $|\eta| < 2.5$, as is expected of the decay products of a centrally

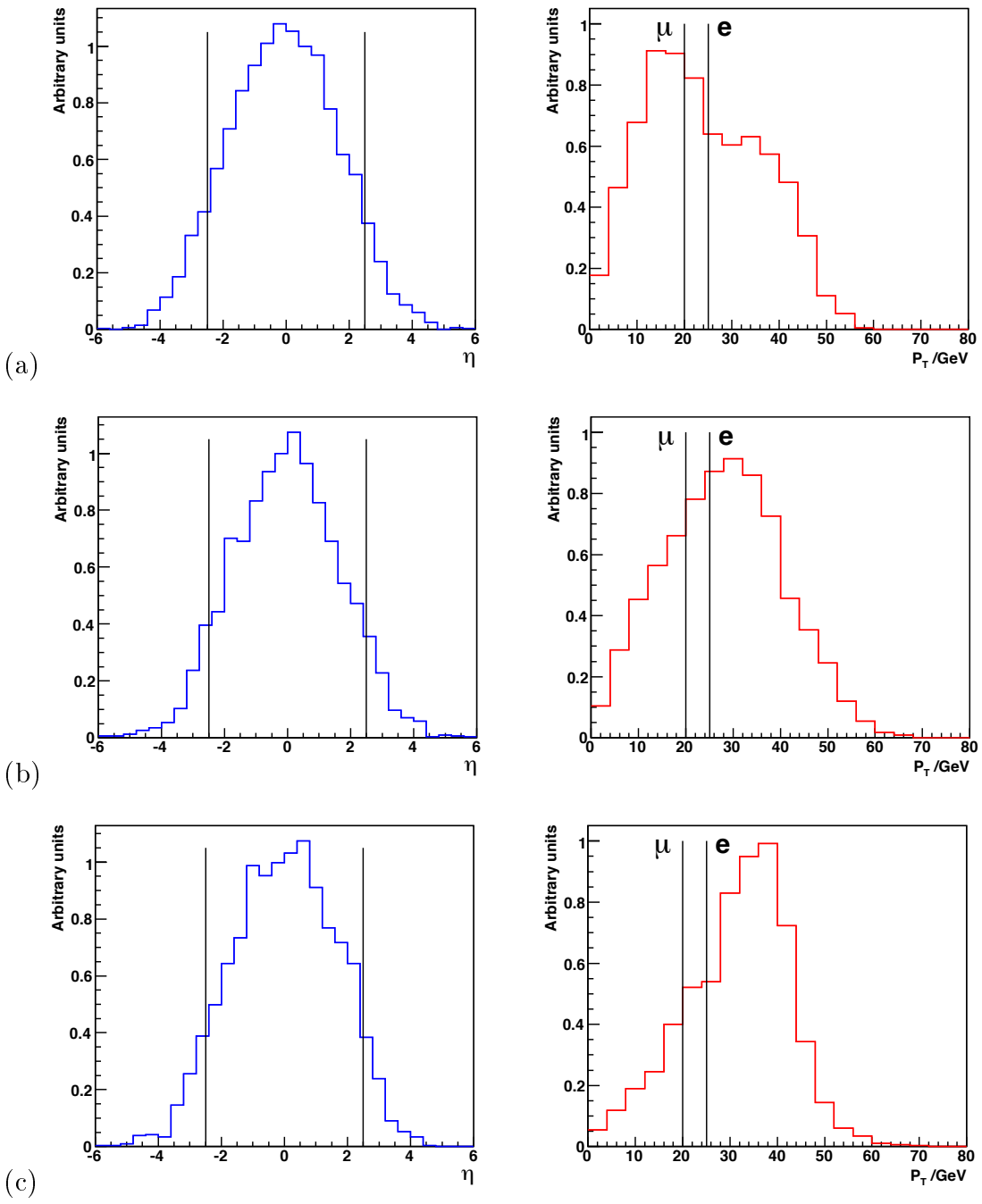

Figure 8.5: The pseudorapidity (left) and transverse momentum (right) distributions of the signal highest-p_T lepton for (a) $M_H = 120$ GeV, (b) $M_H = 140$ GeV, and (c) $M_H = 160$ GeV. The vertical lines on the left plots indicate the trigger pseudorapidity acceptance, and the vertical lines on the right plots show the single leptonic trigger thresholds for electrons and muons.

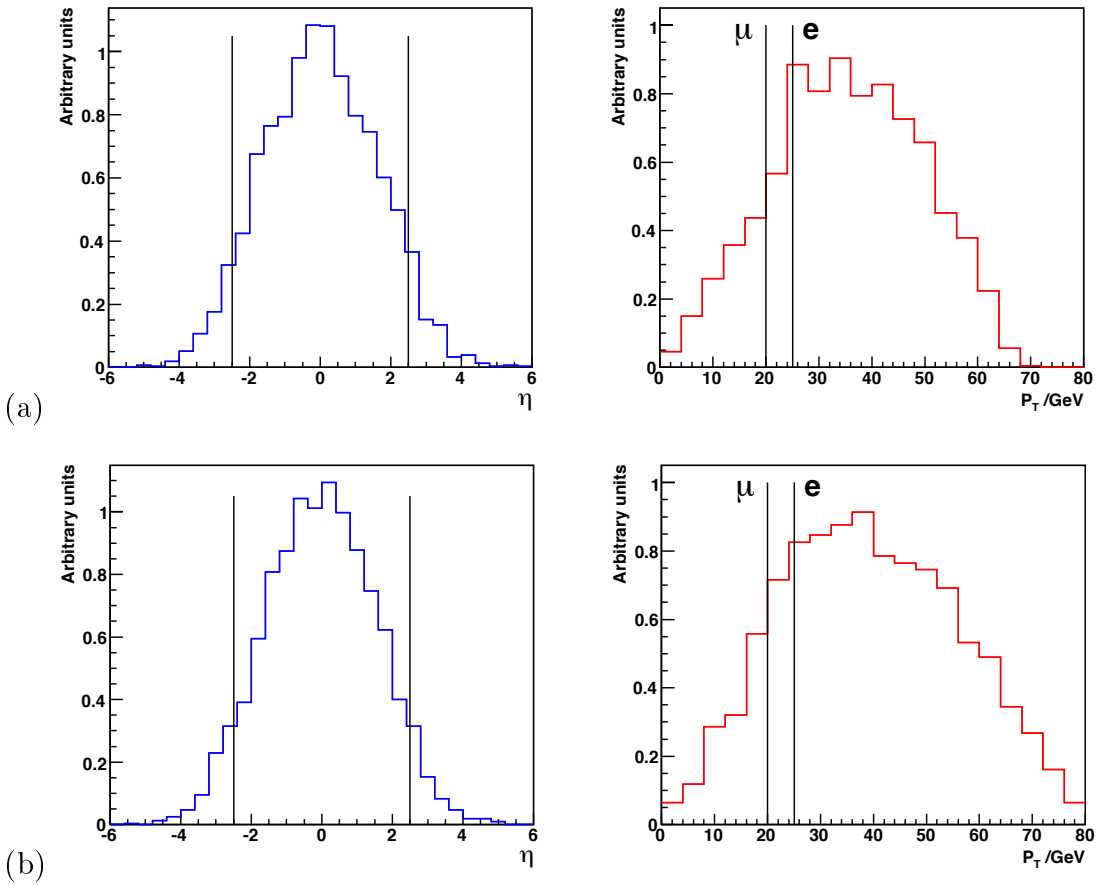

Figure 8.6: The pseudorapidity (left) and transverse momentum (right) distributions of the signal highest-p_T lepton for (a) $M_H = 180$ GeV, and (b) $M_H = 200$ GeV. The vertical lines on the left plots indicate the trigger pseudorapidity acceptance, and the vertical lines on the right plots show the single leptonic trigger thresholds for electrons and muons.

produced Higgs. The trigger selection is more efficient at higher Higgs masses because leptons carry larger transverse momenta.

8.3.3 Hadronic W Reconstruction

In semileptonic signal decays, the hadronic W was reconstructed from the remaining final-state particles other than the highest-p_T lepton. Jet finding was done using the $K_\perp$ clustering algorithm [65] in exclusive mode by forcing the decay products of the hadronic W into two jets. The E recombination scheme was used in which the jets' momenta are formed by adding the four-vectors of the particle momenta that make up the jets.

The $K_\perp$ algorithm in exclusive mode allows the use of merging scale variables for further jet study. These are y_{21}, which defines the scale at which two jets merge into one, and y_{32}, at which three jets merge into two. Jets coming from a W are expected to have a harder splitting scale than quark jets, so the merging scales can be used to suppress backgrounds, as was shown in previous studies [66]. However, since the backgrounds are currently not simulated, no further optimisation of the jet finding was implemented at this stage of the analysis; this can be done in a future study.

The pseudorapidity and transverse momentum distributions of the two jets are shown in Fig. 8.7 and Fig. 8.8 for different Higgs masses after leptonic triggers were applied. The event selection requires both jets to lie within the ATLAS experimental acceptance of $|\eta| < 2.5$. It can be seen in the plots that the jets are central, so most events would pass the η requirement.

The reconstructed dijet invariant masses M_{jj} of the hadronic W, after the leptonic triggers and the jet pseudorapidity cuts, are given in Fig. 8.9. The mass

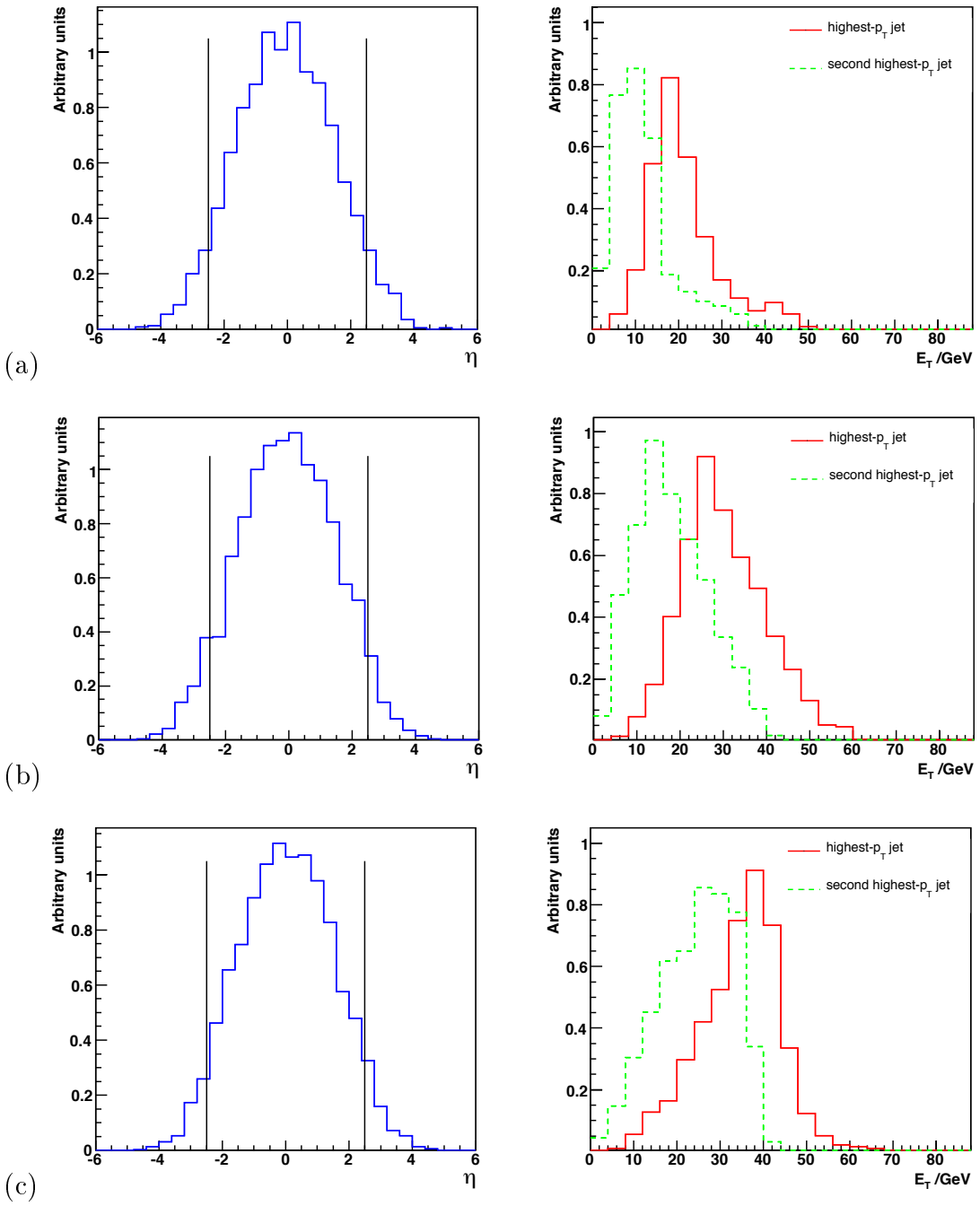

Figure 8.7: The pseudorapidity (left, with two entries per event) and transverse momentum (right) distributions of the two highest-p_T jets in the semileptonic channel for (a) $M_H = 120$ GeV, (b) $M_H = 140$ GeV, and (c) $M_H = 160$ GeV. The vertical lines on the left plots indicate the pseudorapidity acceptance for jets.

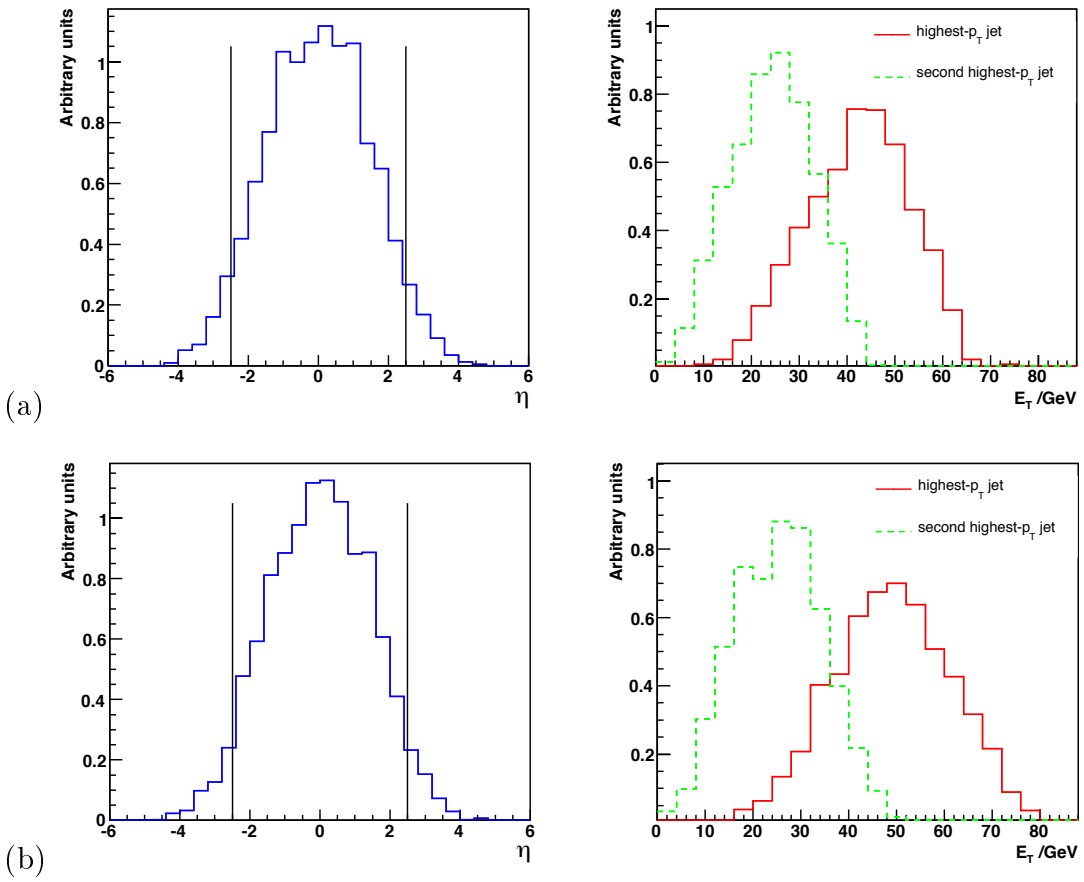

Figure 8.8: The pseudorapidity (left, with two entries per event) and transverse momentum (right) distributions of the two highest-p_T jets in the semileptonic channel for (a) $M_H = 180$ GeV, and (b) $M_H = 200$ GeV. The vertical lines on the left plots indicate the pseudorapidity acceptance for jets.

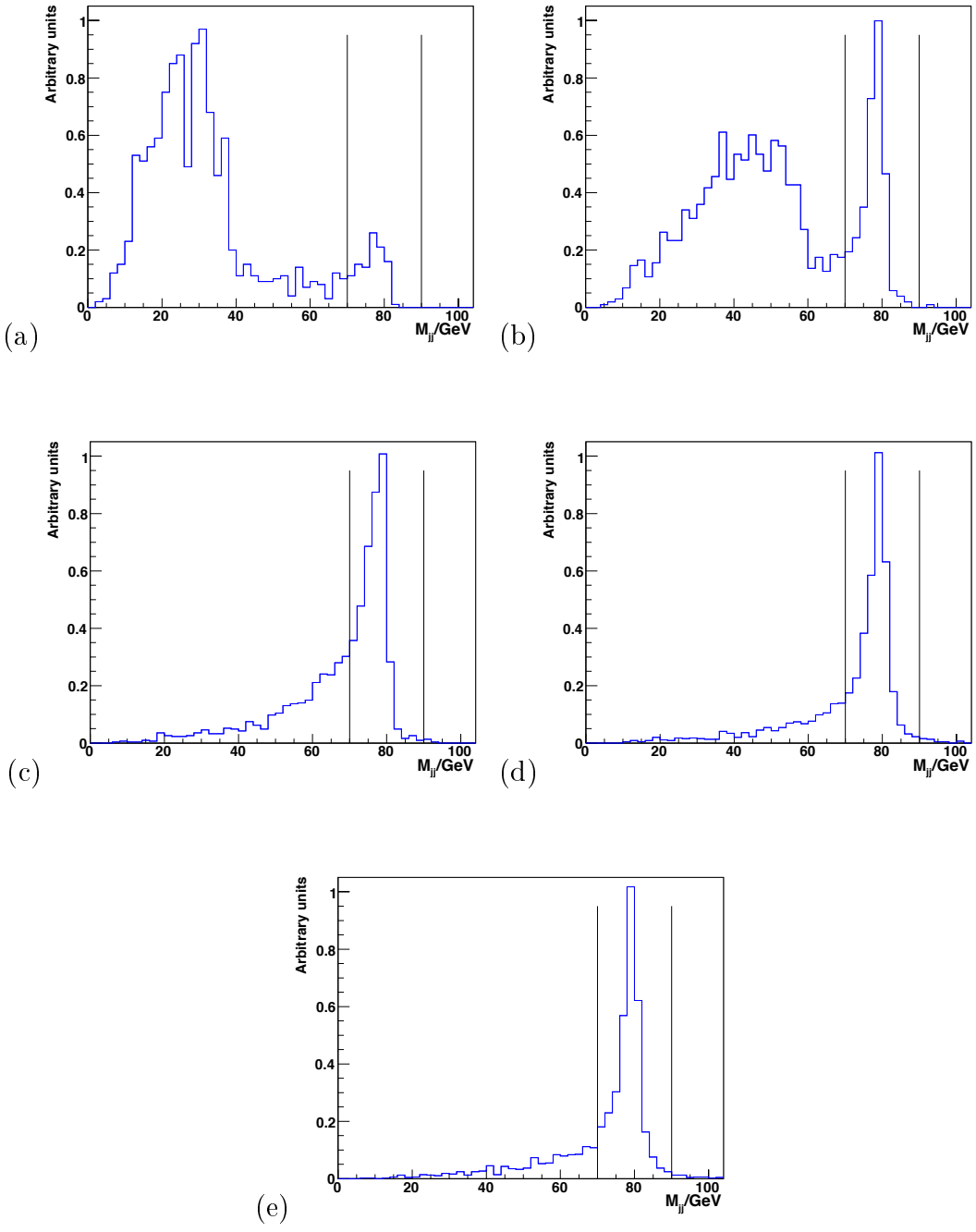

Figure 8.9: The dijet invariant mass M_{jj} distributions in the semileptonic channel for (a) $M_H = 120$ GeV, (b) $M_H = 140$ GeV, (c) $M_H = 160$ GeV, (d) $M_H = 180$ GeV, and (e) $M_H = 200$ GeV. The vertical lines indicate the dijet mass window cut.

distributions peak at the W boson mass, $M_W = 80.4$ GeV. For Higgs masses below the threshold of $2M_W$, one of the W bosons is virtual (W*), giving a second peak in M_{jj} at low mass. The virtual W* mass peak is especially pronounced at the lowest $M_H = 120$ GeV because lepton triggers have already picked out the real W to be leptonic.

In order to reduce the dominant background of exclusive W + 2 jets production, a mass cut was applied to the hadronic W. The chosen mass window was 70 GeV$< M_{jj} <$ 90 GeV. These values can be further optimised once the background process is simulated. Applying a mass window cut does not affect the signal greatly at high Higgs masses. However, in the low-mass case when one W is virtual, the dijet mass cut significantly reduces the signal.

8.3.4 Proton p_T Cut

A cut on the transverse momenta of leading protons was introduced to suppress the QED backgrounds of Fig. 8.2. The cut was only applied for Higgs masses $M_H \geq 160$ GeV, at which the photon-induced backgrounds become large. The events were initially selected to have proton $p_T > 100$ MeV, and the cut was also increased to $p_T > 200$ MeV for further background elimination.

The transverse momentum distributions of the leading protons are shown in Fig. 8.10, where it can be seen that only a small part of the signal would be lost to the proton p_T cut.

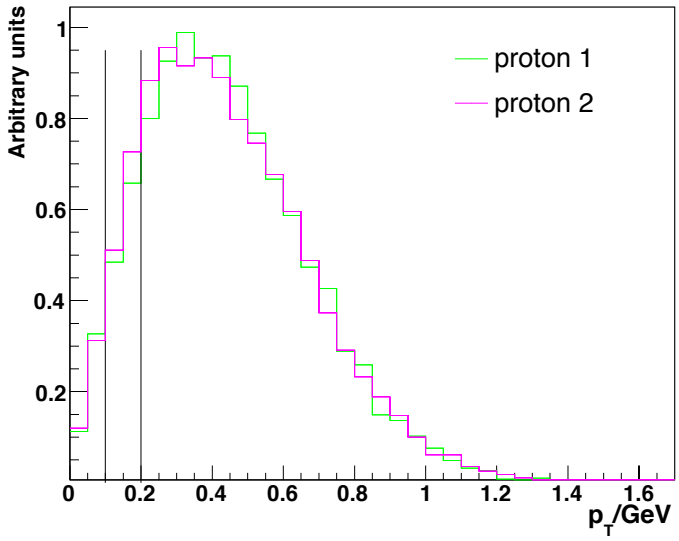

Figure 8.10: The transverse momentum distributions of the leading protons. The vertical lines show the cuts $p_T > 100$ MeV and $p_T > 200$ MeV.

8.4 Results

The event selection efficiencies and the resulting signal cross-sections are summarised in Table 8.1 for semileptonic WW decays, and in Table 8.2 for fully leptonic decays. The results are given for Higgs masses of 120, 140, 160, 180 and 200 GeV.

The cross-sections of the initially generated events (given in the rows of the tables labelled "Generated") include the Higgs to WW branching ratio (as shown in Fig. 7.4), but not the branching ratios of subsequent WW semileptonic or fully leptonic decays. Therefore the trigger efficiencies for fully leptonic decays are lower than those for semileptonic decays, reflecting the large difference in branching ratios.

The last column of Tables 8.1 and 8.2 contains the number of signal events for 30 fb^{-1} integrated luminosity, corresponding to 3 years of LHC running at

Selection cuts	Higgs Mass (GeV)	Efficiency	Signal σ (fb)	Events / 30 fb^{-1}
Generated $H \to$ WW	120	100%	0.403	12.1
	140	100%	0.933	28.0
	160	100%	1.164	34.9
	180	100%	0.843	25.3
	200	100%	0.483	14.5
Acceptance of proton taggers (420m + 215m)	120	61 %	0.246	7.4
	140	67 %	0.625	18.8
	160	71 %	0.826	24.8
	180	74 %	0.624	18.7
	200	77 %	0.372	11.2
ATLAS single lepton triggers	120	9 %	0.035	1.1
	140	13 %	0.119	3.6
	160	17 %	0.194	5.8
	180	18 %	0.154	4.6
	200	20 %	0.096	2.9
2 or more jets within $\lvert\eta\rvert < 2.5$	120	7 %	0.028	0.8
	140	10 %	0.096	2.9
	160	14 %	0.158	4.7
	180	15 %	0.127	3.8
	200	17 %	0.080	2.4
Mass window around the hadronic W 70 GeV $< M_W <$ 90 GeV	120	0.5 %	0.002	0.1
	140	2 %	0.019	0.6
	160	7 %	0.084	2.5
	180	10 %	0.080	2.4
	200	11 %	0.052	1.6
p_T(protons) > 100 MeV	120	N/A	N/A	N/A
	140	N/A	N/A	N/A
	160	7 %	0.077	2.3
	180	9 %	0.073	2.2
	200	10 %	0.047	1.4
p_T(protons) > 200 MeV	120	N/A	N/A	N/A
	140	N/A	N/A	N/A
	160	5 %	0.061	1.8
	180	7 %	0.057	1.7
	200	8 %	0.037	1.1

Table 8.1: The effect of cuts on signal samples for selecting semileptonic WW decays ($WW \to l\nu jj$, $l = e, \mu, \tau$) for different Higgs masses.

Selection cuts	Higgs Mass (GeV)	Efficiency	Signal σ (fb)	Events / 30 fb^{-1}
Generated $H \to$ WW	120	100%	0.403	12.1
	140	100%	0.933	28.0
	160	100%	1.164	34.9
	180	100%	0.843	25.3
	200	100%	0.483	14.5
Acceptance of proton taggers (420m + 215m)	120	61 %	0.246	7.4
	140	67 %	0.625	18.8
	160	71 %	0.826	24.8
	180	74 %	0.624	18.7
	200	77 %	0.372	11.2
ATLAS single lepton or dilepton triggers	120	3 %	0.009	0.3
	140	3 %	0.029	0.9
	160	3 %	0.038	1.2
	180	4 %	0.030	0.9
	200	4 %	0.017	0.5
p_T(protons) > 100 MeV	120	N/A	N/A	N/A
	140	N/A	N/A	N/A
	160	3 %	0.036	1.1
	180	3 %	0.027	0.8
	200	3 %	0.016	0.5
p_T(protons) > 200 MeV	120	N/A	N/A	N/A
	140	N/A	N/A	N/A
	160	2 %	0.0028	0.8
	180	3 %	0.021	0.6
	200	3 %	0.011	0.3

Table 8.2: The effect of cuts on signal samples for selecting fully leptonic WW decays ($WW \to l\nu l\nu$, $l = e, \mu, \tau$) for different Higgs masses.

initial luminosity. After trigger and jet selection, 3 to 6 events will be detected for Higgs masses between 140 and 200 GeV. Applying a dijet mass cut reduces this number to 2 to 3 events. One of these is in the "gold-plated" fully leptonic channel for which there is no significant background. For a Higgs mass of $M_H = 120$ GeV, less than one event is expected.

8.5 Discussion

As a whole, the event yield estimates in this study are conservative from both analysis and theoretical perspectives.

The trigger selection efficiency can increase if tau triggers are included. In addition, single leptonic trigger thresholds could be lowered by requiring two jets in conjunction with a lepton. For example, lowering the single lepton trigger thresholds to 15 GeV can more than double the number of signal events.

The signal cross-sections implemented in ExHuME are pessimistic due to the use of MRST2002 [67] parton distribution functions. Changing the PDF sets in ExHuME to CTEQ6M [68] gives an increase in the signal cross-sections ranging from 37% at $M_H = 120$ GeV to 46% at $M_H = 200$ GeV. The fact that signal rates are likely to be higher than those considered here is confirmed by the recent observations of exclusive diffractive diphoton production by the CDF experiment [69, 70]: the measured number of exclusive diphoton events agrees with the upper bound of the uncertainty on the Durham model prediction.

Even with the current conservative choice of cross-sections and event selection, the Higgs can be observed in the exclusive $WW^{(*)}$ channel with tagged protons for masses $140 < M_H < 200$ GeV. The number of events presented in Section 8.4 can be considered the worst case scenario.

Chapter 9

Conclusion

This thesis has presented two different aspects of the work carried out towards the preparation of the ATLAS experiment. The first aspect covered development and testing of the semiconductor tracker modules. The second aspect consisted of simulations of physics processes to investigate the ability of ATLAS to detect the Higgs boson through the process of exclusive production and decay to $WW^{(*)}$.

The thermal performance of the SCT cooling block was studied in finite element analysis simulations which found the optimal choice of block design. It was shown that a 1-mm PEEK split block presents the best solution for thermally separating the hybrid and the detector parts of a module, and this design was implemented in the module production. Simulations and measurements indicated that the SCT can be operated safely with a coolant at a temperature of -22°C.

The performance of SCT modules with binary readout was investigated with respect to common mode noise. Four SCT modules were tested at the endcap system test by using the coherent occupancy method, and the results showed insignificant common mode pickup. The validity of the method was verified by repeating the tests with injection of a known amount of common mode noise into

the system. The measurements confirmed that the SCT modules meet the low noise requirements of ATLAS.

The potential of ATLAS to detect a light Standard Model Higgs boson, produced in exclusive diffraction and decaying to a pair of W bosons, was evaluated in simulations. The analysis was performed at particle level by selecting fully leptonic and semileptonic WW decays using the ATLAS level 1 leptonic trigger criteria. The results show that if suitable forward proton tagging detectors are installed in the 420-m region around ATLAS, the Higgs can be observed for masses in the range $140 < M_H < 200$ GeV. A lower estimate finds 3 to 6 events in 30 fb^{-1}, the equivalent of the first three years of ATLAS taking data at initial LHC luminosity. More events could be selected if the leptonic trigger thresholds were lowered by requiring additional signatures such as two jets, or if tau triggers were applied.

In order to eliminate the dominant background of exclusive W + 2 jets production, a mass window was applied to the decay products of the hadronic W. The dijet mass window cut halves the number of signal events, and is expected to suppress the background greatly. Future work would involve simulating the exclusive W + 2 jets background. More elaborate cuts on the final states could then be developed, based on the signal and background distributions of kinematic variables. Further jet analysis is expected to make an important contribution to background suppression.

Although conservative, the current results of the exclusive Higgs to $\text{WW}^{(*)}$ study represent an idealised case without any detector effects such as smearing or particle misidentification. The next step to complete the analysis would be to perform a detailed detector simulation of the signal and background.

Bibliography

[1] O. Bruning (ed.) et al. LHC design report. Volume 1: The LHC main ring. CERN-2004-003.

[2] [ATLAS Collaboration]. ATLAS: Technical proposal for a general-purpose p p experiment at the Large Hadron Collider at CERN. 1994. CERN-LHCC-94-43.

[3] [ATLAS Collaboration]. ATLAS: Detector and physics performance technical design report. Volume 1 and Volume 2. CERN-LHCC-99-14, CERN-LHCC-99-15.

[4] [ATLAS Collaboration]. ATLAS Inner Detector: Technical design report. Volume 1. 1997. CERN-LHCC-97-16.

[5] [ATLAS Collaboration]. ATLAS First-level Trigger: Technical design report. CERN-LHCC-99-14, CERN-LHCC-99-15.

[6] M. G. Albrow et al. FP420: An R&D proposal to investigate the feasibility of installing proton tagging detectors in the 420-m region at LHC. CERN-LHCC-2005-025.

[7] B. E. Cox. The FP420 R&D project: Forward proton tagging at the LHC as a means to discover new physics. *AIP Conf. Proc.*, **792**:540–543, 2005.

[8] P. Jenni and M. Nessi (tech. coordinator). ATLAS Forward Detectors for Luminosity Measurement and Monitoring. Letter of Intent. CERN-LHCC-2004-010.

[9] V. A. Khoze, A. D. Martin, and M. G. Ryskin. Physics with tagged forward protons at the LHC. *Eur. Phys. J.*, **C24**:581–587, 2002. hep-ph/0203122.

[10] [ATLAS Collaboration]. ATLAS Inner Detector: Technical design report. Volume 2. 1997. CERN-LHCC-97-17.

[11] S. Eidelman et al. Review of Particle Physics. *Physics Letters B*, **592**:1+, 2004.

[12] C. Joram. Particle Detectors. CERN Summer Student Lect. Prog., 2001.

[13] A. Peisert. Silicon microstrip detectors. *Adv. Ser. Direct. High Energy Phys.*, **9**:1–79, 1992.

[14] T. Nakayama et al. Radiation damage studies of silicon microstrip sensors. *IEEE Trans. Nucl. Sci.*, **47**:1885–1891, 2000.

[15] E. Fretwurst et al. [RD2 Collaboration]. Reverse annealing of the effective impurity concentration and long term operational scenario for silicon detectors in future collider experiments. *Nucl. Instrum. Meth.*, **A342**:119–125, 1994.

[16] D. Ferrère. Silicon vertex detectors in HEP and in the semiconductor tracker of ATLAS. ATL-CONF-99-007, 1999.

[17] G. F. Moorhead. Detector modules for the endcaps of the ATLAS semiconductor tracker. *Nucl. Instrum. Meth.*, **A485**:43–53, 2002.

[18] W. Dabrowski. ABCD3TA ASIC Requirements and Specification. ATL-IS-ES-0039, 2001.

[19] S. Snow, I. Nasteva, and I. Wilmut. Tests of forward SCT cooling blocks with C_3F_8 evaporative cooling. ATL-IS-EN-0023, 2003.

[20] A. Clark, M. Donega, I. Nasteva, S. Snow, R. Wallny, and I. Wilmut. Thermal performance of the ATLAS SCT forward modules. ATL-INDET-2003-010, 2003.

[21] S. Snow. Thermal and Mechanical Specifications and Expected Performance of the Forward SCT Module. ATL-IS-EN-0007, 2002.

[22] H. Becker et al. An improved thermal design of the ATLAS SCT end-caps. ATL-INDET-2000-019, 2000.

[23] FlexPDE, finite element modelling software, PDE Solutions Inc. www.pdesolutions.com.

[24] S. Snow and I. Wilmut. The C_3F_8 Evaporative Heat Transfer Coefficient. http://www.hep.man.ac.uk/atlas/TM/RALhtc.doc, 2002.

[25] L. Eklund, D. Ferrère, B. Gallop, and P.W. Phillips. Electrical Tests of SCT Hybrids and Modules. ATL-COM-INDET-2003-004, 2003.

[26] L. Feld, S. Roe, A. Ahmad, and S. Snow. Measurement of common mode noise in binary read-out systems. *Nucl. Instrum. Meth.*, **A487**:557–564, 2002.

[27] P. J. Bell and J. Grosse-Knetter. Techniques for the measurement of common mode noise in binary read-out systems. *Nucl. Instrum. Meth.*, **A516**:153–159, 2004. ATL-INDET-2002-023.

[28] Z. Dolezal and S. Roe. The Quality Assurance of the ATLAS SCT End-Cap Detector Modules. ATL-IS-QA-0004, 2002.

[29] R. Brun and F. Rademakers. ROOT: An object oriented data analysis framework. *Nucl. Instrum. Meth.*, **A389**:81–86, 1997.

[30] F. Halzen and A. D. Martin. *Quarks and Leptons: An Introductory Course In Modern Particle Physics.* New York, Usa: Wiley, 396p, 1984.

[31] F. Mandl and G. Shaw. *Quantum Field Theory.* Chichester, Uk: Wiley, 354p, 1984.

[32] R. K. Ellis, W. J. Stirling, and B. R. Webber. *QCD and Collider Physics.* Cambridge University Press, 435p, 1996.

[33] A. Signer. The Standard Model. In *Proceedings of the School for Young High Energy Physicists held 31 August to 12 September 2003*, 2004. RAL-TR-2004-008.

[34] C. Adloff et al. [H1 Collaboration]. Measurement and QCD analysis of neutral and charged current cross sections at HERA. *Eur. Phys. J.*, **C30**:1–32, 2003. hep-ex/0304003.

[35] S. Chekanov et al. [ZEUS Collaboration]. Measurement of the neutral current cross section and F2 structure function for deep inelastic e+ p scattering at HERA. *Eur. Phys. J.*, **C21**:443–471, 2001. hep-ex/0105090.

[36] The LEP Electroweak Working Group [OPAL Collaboration]. A combination of preliminary electroweak measurements and constraints on the standard model. 2005. hep-ex/0511027.

[37] R. Barate et al. [LEP Working Group for Higgs Boson Searches Collaboration]. Search for the standard model Higgs boson at LEP. *Phys. Lett.*, **B565**:61–75, 2003. hep-ex/0306033.

[38] J. R. Forshaw. Diffractive Higgs production: Theory. 2005. hep-ph/0508274.

[39] V. A. Khoze, A. D. Martin, and M. G. Ryskin. Diffractive Higgs production: Myths and reality. *Eur. Phys. J.*, **C26**:229–236, 2002. hep-ph/0207313.

[40] V. A. Khoze, A. D. Martin, and M. G. Ryskin. The rapidity gap Higgs signal at LHC. *Phys. Lett.*, **B401**:330–336, 1997. hep-ph/9701419.

[41] V. A. Khoze, A. D. Martin, and M. G. Ryskin. Can the Higgs be seen in rapidity gap events at the Tevatron or the LHC? *Eur. Phys. J.*, **C14**:525–534, 2000. hep-ph/0002072.

[42] V. A. Khoze, A. D. Martin, and M. G. Ryskin. Prospects for new physics observations in diffractive processes at the LHC and Tevatron. *Eur. Phys. J.*, **C23**:311–327, 2002. hep-ph/0111078.

[43] John C. Collins. Light-cone variables, rapidity and all that. 1997. hep-ph/9705393.

[44] A. De Roeck, V. A. Khoze, A. D. Martin, R. Orava, and M. G. Ryskin. Ways to detect a light Higgs boson at the LHC. *Eur. Phys. J.*, **C25**:391–403, 2002. hep-ph/0207042.

[45] M. Spira. QCD effects in Higgs physics. *Fortsch. Phys.*, **46**:203–284, 1998. hep-ph/9705337.

[46] V. A. Khoze, A. D. Martin, and M. G. Ryskin. Soft diffraction and the elastic slope at Tevatron and LHC energies: A multi-pomeron approach. *Eur. Phys. J.*, **C18**:167–179, 2000. hep-ph/0007359.

[47] A. B. Kaidalov, V. A. Khoze, A. D. Martin, and M. G. Ryskin. Probabilities of rapidity gaps in high energy interactions. *Eur. Phys. J.*, **C21**:521–529, 2001. hep-ph/0105145.

[48] Valery A. Khoze, Alan D. Martin, and M. G. Ryskin. Higgs or dijet production in double rapidity gap events. 2000. hep-ph/0006005.

[49] J. Monk and A. Pilkington. ExHuME: A Monte Carlo event generator for exclusive diffraction. 2005. hep-ph/0502077.

[50] A. Djouadi, J. Kalinowski, and M. Spira. HDECAY: A program for Higgs boson decays in the standard model and its supersymmetric extension. *Comput. Phys. Commun.*, **108**:56–74, 1998. hep-ph/9704448.

[51] T. Sjostrand, L. Lonnblad, and S. Mrenna. PYTHIA 6.2: Physics and manual. 2001. hep-ph/0108264.

[52] M. R. Whalley, D. Bourilkov, and R. C. Group. The Les Houches accord PDFs (LHAPDF) and LHAGLUE. 2005. hep-ph/0508110, http://hepforge.cedar.ac.uk/lhapdf/.

[53] A. B. Kaidalov, V. A. Khoze, A. D. Martin, and M. G. Ryskin. Extending the study of the Higgs sector at the LHC by proton tagging. *Eur. Phys. J.*, **C33**:261–271, 2004. hep-ph/0311023.

[54] M. G. Albrow and A. Rostovtsev. Searching for the Higgs at hadron colliders using the missing mass method. 2000. hep-ph/0009336.

[55] A. B. Kaidalov, V. A. Khoze, A. D. Martin, and M. G. Ryskin. Central exclusive diffractive production as a spin-parity analyser: From hadrons to Higgs. *Eur. Phys. J.*, **C31**:387–396, 2003. hep-ph/0307064.

[56] S. P. Martin. A Supersymmetry Primer. 1997. hep-ph/9709356.

[57] A. D. Martin, V. A. Khoze, and M. G. Ryskin. Forward proton tagging as a way to identify a light Higgs boson at the LHC. *Acta Phys. Polon.*, **B33**:3473–3478, 2002. hep-ph/0207062.

[58] B. E. Cox, A. De Roeck, V. A. Khoze, T. Pierzchala, M. G. Ryskin, I. Nasteva, W. J. Stirling, and M. Tasevsky. Detecting the standard model Higgs boson in the WW decay channel using forward proton tagging at the LHC. *Eur. Phys. J.*, **C45**:401–407, 2006. hep-ph/0505240.

[59] M. Duhrssen, K. Jakobs, J. J. van der Bij, and P. Marquard. The process $gg \to$ WW as a background to the Higgs signal at the LHC. *JHEP*, **05**:064, 2005. hep-ph/0504006.

[60] V. A. Khoze, M. G. Ryskin, and W. J. Stirling. Diffractive W + 2 jet production: A background to exclusive $H \to WW$ production at hadron colliders. *Eur. Phys. J.*, **C44**:227–232, 2005. hep-ph/0504131.

[61] R. Kleiss and W. J. Stirling. Spinor Techniques For Calculating $p\bar{p} \to W^{\pm}/Z^0$ + Jets. *Nucl. Phys.*, **B262**:235–262, 1985.

[62] P. Bussey. private communication, 2006.

[63] J. Kalliopuska et al. Resolution studies of the leading proton measurement in exclusive central diffraction at LHC. 2003. HIP-2003-11/EXP.

[64] F. C. Iselin, J. M. Jowett, J. Pancin, and A. Adelmann. MAD version 9. 2000. CERN-SL-2000-026-AP.

[65] J. M. Butterworth, J. P. Couchman, B. E. Cox, and B. M. Waugh. KtJet: A C++ implementation of the K(T) clustering algorithm. *Comput. Phys. Commun.*, **153**:85–96, 2003. hep-ph/0210022.

[66] J. M. Butterworth, B. E. Cox, and J. R. Forshaw. WW scattering at the LHC. *Phys. Rev.*, **D65**:096014, 2002. hep-ph/0201098.

[67] A. D. Martin, R. G. Roberts, W. J. Stirling, and R. S. Thorne. Uncertainties

of predictions from parton distributions. I: Experimental errors. *Eur. Phys. J.*, **C28**:455–473, 2003. hep-ph/0211080.

[68] J. Pumplin et al. New generation of parton distributions with uncertainties from global QCD analysis. *JHEP*, **07**:012, 2002. hep-ph/0201195.

[69] K. Terashi [CDF Collaboration]. New diffraction results from the Tevatron. 2006. hep-ex/0605084.

[70] M. Gallinaro [CDF Collaboration]. Diffractive and exclusive measurements at CDF. 2006. hep-ex/0606024.